



저작자표시-비영리-변경금지 2.0 대한민국

이용자는 아래의 조건을 따르는 경우에 한하여 자유롭게

- 이 저작물을 복제, 배포, 전송, 전시, 공연 및 방송할 수 있습니다.

다음과 같은 조건을 따라야 합니다:



저작자표시. 귀하는 원저작자를 표시하여야 합니다.



비영리. 귀하는 이 저작물을 영리 목적으로 이용할 수 없습니다.



변경금지. 귀하는 이 저작물을 개작, 변형 또는 가공할 수 없습니다.

- 귀하는, 이 저작물의 재이용이나 배포의 경우, 이 저작물에 적용된 이용허락조건을 명확하게 나타내어야 합니다.
- 저작권자로부터 별도의 허가를 받으면 이러한 조건들은 적용되지 않습니다.

저작권법에 따른 이용자의 권리는 위의 내용에 의하여 영향을 받지 않습니다.

이것은 [이용허락규약\(Legal Code\)](#)을 이해하기 쉽게 요약한 것입니다.

[Disclaimer](#)

Ph.D. DISSERTATION

Electrochemical biosensor platform
based on electron tunneling

전자 터널링 기반의 전기화학 바이오센서 플랫폼

By

Jun Yeon Yun

August 2018

DEPARTMENT OF ELECTRICAL AND COMPUTER ENGINEERING
COLLEGE OF ENGINEERING
SEOUL NATIONAL UNIVERSITY

Electrochemical biosensor platform based on electron tunneling

전자 터널링 기반의 전기화학 바이오센서 플랫폼

指導教授 朴炳國

이 論文을 工學博士 學位論文으로 提出함

2018 年 8 月

서울대학교 大學院

工科大學 電氣·컴퓨터 工學部

尹俊淵

尹俊淵의 工學博士 學位論文을 認准함

2018 年 8 月

委員長 이종호 (印)
Chairman Jong-Ho Lee

副委員長 박병국 (印)
Vice-chairman Byung-Gook Park

委員 박영준 (印)
Committee Young June Park

委員 정준호 (印)
Committee Junho Chung

委員 신동식 (印)
Committee Dong-Sik Shin

Electrochemical biosensor platform based on electron tunneling

by

Jun Yeon Yun

Submitted to

the Department of Electrical and Computer Engineering

in partial fulfillment of the requirements

for the degree of Doctor of Philosophy

in Electrical Engineering

at

SEOUL NATIONAL UNIVERSITY

August 2018

© Seoul National University 2018

Committee in Charge:

Jong-Ho Lee, Chairman

Byung-Gook Park, Vice-Chairman

Young June Park

Junho Chung

Dong-Sik Shin

Dedicated to my beloved family

Abstract

Electrochemical biosensor platform based on electron tunneling

Jun Yeon Yun

Department of Electrical and Computer Engineering
College of Engineering
The Graduate School
Seoul National University

We propose an electrochemical protease biosensor platform, called T-chip based on electron tunneling (electrochemistry) and the voltage pulse method to extract the pure transient tunneling current characteristics of the sensor device. By analyzing the I-V and C-V characteristics of the T-chip device with its unique structure having the 2-terminal asymmetric electrodes, the new perspective on the T-chip device describing as the metal-insulator-electrolyte (MIE) capacitor has been suggested.

The biosensor application for the detection of the Trypsin as the target molecule has been demonstrated in the imitated human serum condition with the high concentration of the nonspecific BSA protein of 500 μM . It has been found that the voltage pulse method can enhance the sensitivity and the nonspecific-to-specific ratio performances of the biosensor device than the cyclic-voltammetry

measurement.

In addition, the effect of the back-filling materials on the surface of the electrodes has been studied, and the optimized structure of the T-chip device has been established. The biomolecular transport in the bulk electrolyte solution and the biochemical reaction has been simulated by solving the reaction-diffusion equation and Menten-Michaelis kinetics. The equivalent circuit of the T-chip device is also proposed, and simulated by using the MNA technique. To overcome the limitation of the voltage pulse method, the generalized voltage pulse method based on the integration of the tunneling current is suggested. Finally, the pH sensor application of the T-chip device has been demonstrated by utilizing the MCH-SAM on the electrode of the device.

In this research, we have focused on creating new perspectives even there are somewhat rough and radical assumptions. Even if our approach is not that much perfect and the experimental data are not that much precise, we believe that it is of great value to find new possibilities for the future device not only in the biosensor industry but also in the other scientific field developing the solid-state devices.

Keywords: Electrochemical biosensor, protease biosensor, electron tunneling, self-assembled monolayer (SAM), redox state, Methylene blue (MB), peptide, Trypsin, Metal-insulator-electrolyte (MIE) structure. cyclic-voltammetry (Cyc-V), quasi-static capacitance-voltage (QSCV) measurement, voltage pulse

method, reaction-diffusion system, Menten-Michaelis kinetics, modified nodal analysis (MNA), generalized voltage pulse method, pH sensor.

Student Number: 2013-20837

Contents

Abstract	i
Contents	iii
List of Tables	vii
List of Figures	vii
Chapter 1. Introduction	1
1.1. POCT in general: trend of market and society	1
1.2. Competing technologies for POCT application.....	15
1.3. Review of electrochemical biosensor (T-chip) based on electron tunneling.....	19
Chapter 2. T-chip	24
2.1. Device fabrication and structure of T-chip.....	24
2.2. Immobilization of probe peptide.....	32
2.3. Reference electrode-free electrochemical device	36
2.4. Strategy for detection of biomarkers	38
2.5. Target biomarker: Trypsin.....	40
Chapter 3. Electrochemical characteristics of T-chip	42
3.1. I-V characteristics of T-chip.....	42
3.2. C-V characteristics of T-chip.....	50
Chapter 4. Metal-insulator-electrolyte capacitor	57
4.1. Similarity between metal-insulator-electrolyte (MIE) and metal-oxide-semiconductor (MOS) capacitors	57
4.2. Concept of flat-band voltage	61

4.3. Flat-band voltage shifts and energy band diagram	67
4.4. Equivalent circuit model of T-chip	75
4.5. Capacitive components of T-chip	81
Chapter 5. Voltage pulse method.....	89
5.1. Motivation	89
5.2. Preparation of sensor device and electrical measurement.....	96
5.3. Extraction of transient tunneling current.....	99
5.4. Verification of voltage pulse method	107
5.4.1. Practical problem: voltage and time windows	107
5.4.2. Validation of eliminating capacitive current and extracting tunneling current for voltage pulse method	113
5.4.3. Correlation between the C-V characteristics and results of voltage pulse method.....	119
Chapter 6. Application to protease biosensor	125
6.1. Trypsin detection.....	125
6.2. Experimental result of sensing Trypsin.....	127
6.3. Effect of nonspecific adsorption	135
Chapter 7. Conclusion.....	139
Appendix 1. Appendix 1. Effect of back-filling material.....	143
A1.1. MB-modified peptide and back-filling materials of MCXs.....	143
A1.2. Trypsin as a target molecule	145
A1.3. Measurement configuration	145
A1.4. Experiment for optimization of device condition	147
A1.5. Effect of the back-filling materials of MCXs	149
Appendix 2. Appendix 2. Numerical simulation.....	155
A2.1. Diffusion and reaction of biomolecules in electrolyte	155
A2.2. Modified Nodal Analysis.....	165

Appendix 3. Appendix 3. Generalized voltage pulse method.....	173
A3.1. Integration of tunneling current	173
Appendix 4. Appendix 4. pH sensor application	179
A4.1. MIE capacitor for pH sensor application.....	179
Bibliography	185
초 록.....	193

List of Tables

Table 1-1. Summary of the sensing performance with various protease biosensor platforms for MMP9 detection.	17
Table 2-1. Fabrication process of the T-chip device.	27

List of Figures

Figure 1-1. POCT diagnostics market segmentation & scope [1]. The segments are categorized by products, applications, and regions.	4
Figure 1-2. Summary of the POCT market [1]. Most of the POCT market share is occupied by the products for diabetes including glucose and HbA1c testing and by the applications for specialized institutions including clinics, hospitals, and healthcare facilities.	5
Figure 1-3. Major market participants in the POCT market [1].	6
Figure 1-4. Segmental positions of the POCT product in 2015 [1].	7
Figure 1-5. Roche distribution presence [1].	8
Figure 1-6. Werfen Group distribution presence [1].	9
Figure 1-7. Abbott Laboratories distribution network coverage [1].	10
Figure 1-8. Siemens Healthcare distribution presence [1].	11

Figure 1-9. Danaher distribution presence [1].	12
Figure 1-10. Categorization of market participants of the POCT industry [1].	13
Figure 1-11. Smartphone-based POCT sensor devices (a) Wireless blood pressure monitor (BP) developed by iHealth Lab Inc., (b) iHealth BP dock, (c) wireless BP wrist monitor, (d) wireless digital scale, (2)wireless body analysis scale, (f) wireless activity and sleep tracker, (g) wireless pulse oximeter, (h) wireless Smart Gluco-monitoring system, and (i) iHealth Smartphone Algner [4].....	14
Figure 1-12. (a) I-V characteristics of Cyclic voltammetry results after injecting 1 nM MMP9 solution, (b) Ratio of current decreases (calibration curve) in different concentrations of MMP9 and BSA after 1 hour.....	21
Figure 1-13. (a) I-V characteristics of Cyclic voltammetry results after injecting human serum solution, (b) Ratio of current decreases (calibration curve) in different concentrations of MMP2 in human serum after the reaction for 1 hour.	23
Figure 2-1. Illustration of the total fabrication process of the T-chip device. (a) Cleaning process, (b) TEOS wet oxidation, (c) photolithography, (d) E-gun metal evaporation, (e) lift-off process and chip-dicing.....	28
Figure 2-2. (a) Lay out of the T chip having the size of 5 mm x 5 mm. (b) the fabricated 4-inch wafer after dicing process.....	29
Figure 2-3. (a) Layout of the T-chip device. (b) T-chip mounted on the PCB board. (c) Schematic of T-chip integrated with the PMDS well.....	30
Figure 2-4. (a) Sequence of probe peptide. Methylene blue (MB) is modified at the end of the peptide. Thiol of Cys was used to immobilize the peptide on the gold electrode by forming the Au-thiol covalent bond. (b)	

Schematic of the electrode surface.....	34
Figure 2-5. (a) Reference electrode-free device (T-chip) and its concentric electrode structure. (b) Due to the area asymmetry of the electrodes, the electrical potential of the bulk electrolyte is stabilized by capacitive coupling, called “ <i>self-gating effect</i> .” (c) MB-modified peptide SAM is immobilized on the gold electrode. (d) Potential profile from the working electrode to the counter electrode. Most of the potential drop occurs through the SAM and SCR.....	37
Figure 2-6. Illustration of the target-probe cleaving event. The target biomarker (protease or enzyme) cleaves the probe peptide. After the target-probe reaction, the number of the fixed MB states on the electrode surface reduces once the fragment of the peptide diffused from the electrode surface. The reduction of the tunneling current indicates the concentration of the target biomolecules.....	39
Figure 2-7. Crystal structure of bovine Trypsin (EC 3.4.21.4) [23]. Trypsin is one of the serine protease and it found in the digestive system of vertebrates.....	41
Figure 3-1. Schematic illustration of (a) the T-chip device, (b) Stair-case input voltage, (c) its transient current characteristic, and (d) I-V characteristics of the T-chip device.....	45
Figure 3-2. Schematic illustration of the I-V characteristics of the bare, peptide (pep-SAM), and peptide-MB-SAM (pep-MB-SAM) devices and their structures.....	46
Figure 3-3. Measured I-V characteristics of the bare (black), pep-SAM (red), and pep-MB-SAM (blue) devices. In the case of the bare electrode, the combination of the remaining capacitive current of the EDL and the leakage current due to weak electrolysis is plotted in the black line. Both	

current value decreased after immobilizing the pep-SAM layer on the electrode surface as plotted in the red line. Without MB modification (red) only capacitive and leakage background current is observed. With MB modification (blue) the tunneling event occurs. The electrical potential applied to the working electrode was varied from -0.4 V (hold time 5 s) to 0.2 V with 0.02 V steps (delay time 20 ms and scan rate 1 V/s) while the counter electrode was grounded. 47

Figure 3-4. Schematic illustration of (a) peptide-MB immobilized on the gold electrode and (b and c) its energy band diagram..... 48

Figure 3-5 Schematic illustration of (a) the T-chip device, (b) Stair-case input voltage, (c) its transient current characteristic, and (d) C-V characteristics of the T-chip device..... 52

Figure 3-6. C-V characteristics of the various devices with different surface conditions. The potential of the working electrode was swept from 0 V to -0.5 V and +0.5 V..... 53

Figure 3-7. C-V characteristics of the various devices with different surface conditions. The potential of the working electrode was swept from 0 V to -0.5 V and +0.5 V and the counter electrode was grounded. The bare electrode shows either nonlinear and asymmetric profile. (the black) After introducing peptide SAM on the metal electrode, the capacitance become quite symmetric (the red). By facilitating this symmetrized capacitance, the capacitive current can be eliminated and the tunneling current can be extracted in the pulse method. The existence of the MB states is observed in the negative bias region indicating that the standard redox energy level of the MB is higher than the Fermi level of the gold electrode. The MB state can be considered as the trap state (donor-like) which is similar to the interface or oxide trap of the solid state devices. It

can be described as the capacitance, C_q	54
Figure 4-1. (a) Schematic illustration of the T-chip device and (b) electrical potential profile across the T-chip device.....	59
Figure 4-2. (a) Electrical potential profile across the T-chip device, (b) cross-sectional view of the T-chip device nearby the working electrode, which can be considered the MIE capacitor, and (c) that of the MOS capacitor structure.	60
Figure 4-3. Schematic illustration of the (a) MOS and (b) MIE capacitors and their C-V characteristics. The concept of the flat-band voltage shift can be introduced.....	63
Figure 4-4. Energy band diagram and pseudo-energy band diagram of the MOSOS and MIEIM structure with negative fixed charge states.....	64
Figure 4-5. Energy band diagram and pseudo-energy band diagram of the MOSOS and MIEIM structure with negative fixed charge states under the flat-band voltage bias condition.	65
Figure 4-6. Schematics of the peptide only device, peptide with MCP, peptide with MCH, and peptide with MCN.	70
Figure 4-7. I-V characteristics of the devices for different SAM thickness. .	71
Figure 4-8. Energy band diagram of the devices with different thickness of the SAM under the flat-band voltage condition.	72
Figure 4-9. Energy diagram of the T-chip with the MB redox state. The MB redox state acts as the trap capacitance to capture and release the electron.	73
Figure 4-10. C-V characteristics of the T-chip devices having different modifications of the electrode surface.....	74
Figure 4-11. Equivalent circuit with the capacitive components of the (a) MOS and (MIE) capacitor.	78

Figure 4-12. Equivalent circuit with the capacitive components of the (a) MOS and (MIE) capacitor with the trap capacitance.....	79
Figure 4-13. The schematic illustration of the I-V characteristics of the bare, peptide (pep-SAM), and peptide-MB-SAM (pep-MB-SAM) devices and their structures.....	86
Figure 4-14. (a) Schematic illustration of the bare device. (b) C-V profiles of the bare device and its fitted numerical calculations.....	87
Figure 4-15. (a) Schematic illustration of the peptide-SAM device. (b) C-V profiles of the peptide-SAM device and its fitted numerical calculations.	88
Figure 5-1. (a) T-chip platform. The peptide SAM is immobilized on the electrode by adopting Au-thiol bonding. The end of the peptide is modified with methylene blue (MB) as a redox state acting as a donor-like trap where the tunneling event occurs. (b) The equivalent circuit. The large capacitance component at the EDL and SCR: the EDL component is formed between the electrolyte and the bare electrode uncovered by the SAM, while the SCR component is formed between the SAM and the electrolyte. The MB state and its tunneling rate can be equivalently described as C_q and R_t , respectively.....	93
Figure 5-2. Electrical potential (small signal < 50 mV) and its corresponding current responses for (a) the staircase and (b) square-wave Cyc-V. Both measurement methods take only a single point of the tunneling current, which appears after decaying of the capacitive current with delay time. (c) Transient tunneling current can be extracted by eliminating the capacitive current in the suggested pulse method. The electrical potential (large signal ~500 mV) is applied to maximize the amplitude of the tunneling current.	94

Figure 5-3. Measurement system with device connection. The electrical potential of the electrolyte is stabilized by the virtual ground of the op-amp. The current response of the input voltage pulse is converted into the voltage signal and captured by a digital oscilloscope..... 95

Figure 5-4. (a) Reference electrode-free device (T-chip) and its concentric electrode structure. (b) Due to the area asymmetry of the electrodes, the electrical potential of the bulk electrolyte is stabilized by capacitive coupling, called “*self-gating effect*.” (c) MB-modified peptide SAM is immobilized on the gold electrode. (d) Potential profile from the working electrode to the counter electrode. Most of the potential drop occurs through the SAM and SCR. 98

Figure 5-5. Schematics of the devices functionalized by the SAM with MB (pep-MB-SAM) and without MB (pep-SAM) and their equivalent circuits. (a, c) Measured current responses and their differences. (b, d) Plotted current responses are captured from the 2nd stage of the circuit shown in Fig. 5-3. The transient tunneling current (blue in (d)) is extracted in the case of pep-MB-SAM, while no appreciable tunneling current (red in (b)) is observed in the case of pep-SAM. 103

Figure 5-6. Additional control experiments. The bare device (a) and the partially modified pep-MB-SAM device (c). Measured current responses and their differences (b, d). The capacitive currents are not fully eliminated in both cases..... 104

Figure 5-7. Transient current characteristics after subtracting the capacitive current components (The plots from Figs. 5-5 and 6 are reorganized). The pep-SAM device without electron tunneling (a, red) and the pep-MB-SAM device with electron tunneling (c, blue). Additional control samples: the bare device (b, purple) and the partially modified pep-MB-

SAM device (d, green).....	105
Figure 5-8. C-V characteristics of the various devices under different surface conditions. The potential of the working electrode is swept from 0 to -0.5 V and +0.5 V, while the counter electrode is grounded. The bare electrode shows either a nonlinear or an asymmetric profile (purple). After introducing the peptide SAM on the metal electrode, the capacitance becomes quite symmetric (red). The existence of MB states is observed in the negative-bias region (blue). The MB state can be considered as the trap state (donor-like), which is similar to the interface trap or the oxide trap of the solid-state devices. It can be described as capacitance, C_q , in Figs. 5-1 and 5. By utilizing this symmetrized capacitance (red), the capacitive current can be eliminated and the tunneling current can be extracted in the pulse method. This indicates that the pulse method would not work for the partially modified pep-MB-SAM device (green) with the asymmetric capacitive characteristic.	106
Figure 5-9. Measurement configuration. Two devices are connected and its transient characteristics are measured in parallel. The measurement system consists of the three stages including the amplification stages and the 1 st order low pass filter stages which covert the current signals to voltage signals. At the end of each stages the voltage signals are captured by oscilloscopes.	109
Figure 5-10. (a) Three oscilloscopes for the three stages of the measurement system and the function generator. (b) PCB board of the measurement system.	110
Figure 5-11. Schematic plot of the transient current characteristics of the total current (gray) and the tunneling current (blue). The drastic decreases of	

the current characteristics in transient time are plotted in the log-log plot.
..... 111

Figure 5-12. Measured plots of the transient current characteristics of the total current (gray) of the T-chip device, the current differences of the pep-SAM (red) device, and the extracted tunneling currents from the pep-MB-SAM device (blue). The transient current characteristics are plotted in (a) linear plot, (b) semi-log-x plot, (c) semi-log -y plot, and (d) log-log plot..... 112

Figure 5-13. Histogram of the current values at 7 μ s, 110 μ s, and 1.1 ms in the transient time for each stage. The total 86 devices: 43 devices for the pep-SAM device (red) and 43 devices for the pep-MB-SAM device (blue) were used. 115

Figure 5-14. Confusion matrix also known as an error matrix obtained from the histogram by varying the cut-off level..... 116

Figure 5-15. Receiver operating characteristic (ROC) curve of the two predictors obtained from the histogram and the confusion matrix of each stage by varying the cut-off value of the current level. One is for the experimental dataset and the other is for the numerically fitted dataset. At the 1st stage the estimated accuracy is about 90%, however, at the 2nd and 3rd stages, the estimate accuracies are 100 %, which means that the capacitive current mismatch can be distinguishable from the tunneling current..... 117

Figure 5-16. C-V characteristics of the pep-SAM (up) and pep-MB-SAM (down) devices and their change in time for 600 s. at the initial condition, the C-V characteristic is asymmetric and the capacitive current cannot be eliminated by voltage pulse method. The asymmetric C-V characteristics of the pep-SAM device becomes symmetrized because the structural

transformation of the peptide SAM occurs when its structure is stabilized in the electrolyte solution..... 121

Figure 5-17. Monitored C-V characteristics and the current difference of the pep-SAM device (up) and pep-MB-SAM device (down) for 600 s. In the case of the pep-SAM device, the current difference of the pep-SAM device becomes small as the C-V characteristic of that becomes symmetrized. Whereas the current difference of the pep-MB-SAM device in transient time has negative value after the stabilization, which indicates the electron tunneling at the negative voltage pulse. 122

Figure 5-18. Correlation between the current difference and the positive-to-negative capacitance difference (PNCD). The PNCD values are obtained from the maximum values of the capacitance at the positive and negative voltage region of the pep-SAM device and from the peak capacitance value at the negative voltage region and the capacitance value at the positive voltage region where the absolute value of the positive and the negative voltages are same. As the stabilization progressed for 600 s, the correlation between the current difference and PNCD of the pep-SAM device shows linear trace (red) while that of the pep-MB-SAM device shows negatively biased trace (blue). 123

Figure 6-1. The measurement configuration of the experiment. The monitored features are (a) the positive peak current value of the Cyc-V measurement and (b) the current value at 500 μ s in transient time..... 130

Figure 6-2. Signal suppression of the peak current in the Cyc-V measurement as a function of reaction time. (a) The nonspecific BSA is dissolved in DPBS as a control. (b)–(d) Concentration of Trypsin is varied from 10 to 1000 nM. (e) The device is incubated under the pure DPBS condition. 131

Figure 6-3. Signal suppression of the tunneling current extracted from the pulse method. (a) The nonspecific BSA is dissolved in DPBS as a control. (b)–(d) The Trypsin concentration is varied from 10 to 1000 nM. (e) The device is incubated in the pure DPBS condition. Compared to the Cyc-V in Fig. 6-1, the nonspecific effect is reduced and the sensitivity is enhanced. 132

Figure 6-4. Calibration curves of the sensor device for the Cyc-V measurement (the black line) and the pulse method (the blue line). Different background levels of the nonspecific effect (the gray and red lines) are observed in both cases. 133

Figure 6-5. Specific-to-nonspecific signal ratio, SNR $t_r=1000$ s, of the sensor device adopting the conventional Cyc-V and the suggested pulse method. 137

Figure 6-6. (a) Schematic of nonspecific adoption and (b) its representation as a series capacitance C_{BSA} in equivalent circuit. 138

Figure A1-1. (a) Schematics of the peptide-MB only device, peptide-MB with MCP, peptide-MB with MCH, and peptide-MB with MCN. 148

Figure A1-2. (a) I-V characteristics and (b) C-V characteristics of the T-chip device with different back-filing material conditions. 151

Figure A1-3. Monitored peak current values of the I-V characteristics of each device. The suppressed signal values were normalized by the current values right before the injection of the Trypsin sample solution at 250 s. The maximum current change was shown in the case of the peptide device with the back-filing material of MCH (the blue line). The other three cases showed similar but less changes than MCH; MB-peptide only (the black line), back-filing material of MCP (the red line), and MCN (the green line). 152

Figure A1-4. Schematic view of the peptide cleaving event. Because the cleaving site of the peptide sequence (carboxyl side of the amino acid arginine) is located close to the electrode surface, the longest back-filling material of MCN hindered the approach of the target biomolecule. In the other cases with shortest back-filling material of MCP and without back-filling material, the probe sequence cannot form proper structure in the electrolyte solution. Although the Trypsin can approach the cleaving site of the probe peptide, the reaction activity between the probe peptide and Trypsin decreased..... 153

Figure A2-1. Schematic illustration of the 1-D diffusion equation..... 159

Figure A2-2. Menten-Michaelis kinetics..... 160

Figure A2-3. Reflecting boundary condition and Neumann boundary condition. 161

Figure A2-4. Correspondence between Menten-Michaelis kinetics and the NBTI model. 162

Figure A2-5. Solution of the reaction-diffusion equation at the reaction time (a) 0, (b) 800, and (c) 1600 s. (left) Bulk concentration of the target protein (green) and the fragment of the probe peptide (blue) generated by the probe-target cleaving event. (right) Normalized surface concentration of the probe peptide (purple) and sum of that and the peptide-enzyme intermediate states (red)..... 163

Figure A2-6. (left) MNA by solving the differential algebraic equation and (right) the linear algebraic equation with the companion model. 168

Figure A2-7. Example of MNA for the R-C circuit and its matrix formulations of DAE and LAE with the companion model. 169

Figure A2-8. (up) Jacobian matrix and its elements calculated analytically. (down) Numerical Jacobian matrix and the its elements, which can

change its size and the elements automatically according to the given matrix equation.....	170
Figure A2-9. (a) equivalent circuit of the T-chip device and (b) simulated I-V characteristics by using MNA in the case of the initial condition (blue) and the case of the device with BSA capacitance, which describe the nonspecific effect to the circuit component equivalently. Each circuit components were dealt with in the previous chapter.	171
Figure A3-1. Schematic of the voltage pulse method to extract the transient tunneling current.	176
Figure A3-2. Schematic of the generalized voltage pulse method based on integration of the tunneling charge.....	177
Figure A4-1. (a) MIE structure, (b) MIE capacitor, (c) EIS structure, and (d) ISFET.....	182
Figure A4-2. (up) C-V characteristics of the MIE capacitor with the various pH conditions. (down) Line plot of the flat-band voltage according to the pH value.....	183

Chapter 1.

Introduction

1.1. POCT in general: trend of market and society

Point-of-care testing (POCT), near patient or bedside testing, is essential for the rapid detection of biochemical analytes (biomarkers and chemical markers) without complex extra laboratory-level testing. POCT facilitates better diagnosis of disease, monitoring of a patient's condition and managing the health of the general public. At field sites in an emergency or at regions with the lack of professional manpower, it enables quick medical decisions. Also, disease diagnosis at an early stage by using POCT helps patients to start necessary medical treatment in appropriate time.

The global POCT market is expected to grow from US\$ 23.71 billion in 2017 to US\$38.13 billion in 2022 at the compound annual growth rate (CAGR) of 10.0% during the forecast period [1]. Most of the POCT market is occupied by North America, followed by Europe. Asia-Pacific's POCT market is now growing at its

fastest CAGR of 14.2% [2]. The demands of the POCT product has been increasing due to rising preference for the home health care across the globe and high needs for the compact sensor device to diagnose infectious diseases and to prevent its prevalence in developing countries. However, the POCT market is biased towards the diabetes monitoring device and limited to a few applications. The POCT devices for the glucose and the HbA1c testing occupies the major portion of the total POCT market share. Though demand and supply for the POCT personal home application is growing, still most portion of the POCT market share is dominated by the clinics, hospitals, and healthcare facilities (Fig. 1-2) where the several market participants (i.e., Roche, Abbott Laboratories, Siemens Healthcare, and Danaher Corporation) are leading in the commercialized market and POCT technology [1].

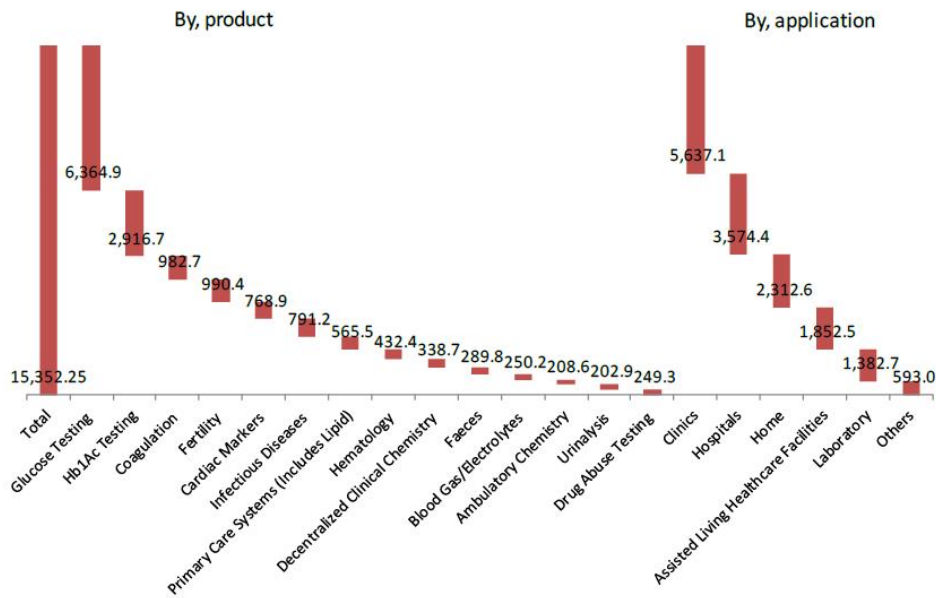
The new trend in POCT is based on the smart devices especially equipped with mobile-healthcare, which can be expected to achieve personalized healthcare monitoring and management services in real-time[3]. One of the most promising mobile-healthcare technology is cellphone-based POCT technology. Since the number of cellphone users in global has already exceeded 7.4 billion, 70% of which are in developing countries, where POCT devices are most needed, the cellphone can be a general platform for the personalized POCT industry. The exemplary application of cellphone-based POCT includes the readout of colorimetric, fluorescent, chemiluminescent, electrochemical, lateral flow, and label-free assays; detection of cells, biomolecules, nanoparticles, and microorganism; and other

diagnostic applications [4].

Some successful smart applications based on the cellphone devices have been started to be commercialized for the monitoring and managing the basic health parameters in person, such as blood glucose, blood pressure, weight, body analysis, pulse rate, electrocardiogram, and physical activity. However, those parameters are focused on general indicators monitored for the health management rather than on the indicators for diseases diagnosis. Although lots of demand on POCT devices for early diagnosis of disease is required, still there is a lack of supply of POCT devices with high accuracy and reliability. Therefore, the current state of the POCT market and industry indirectly indicates how the successful POCT device for disease diagnosis is difficult to be achieved.



Figure 1-1. POCT diagnostics market segmentation & scope [1]. The segments are categorized by products, applications, and regions.



Source: WHO, U.S. CDC, FDA, Investor Presentations, Primary Interviews, Grand View Research

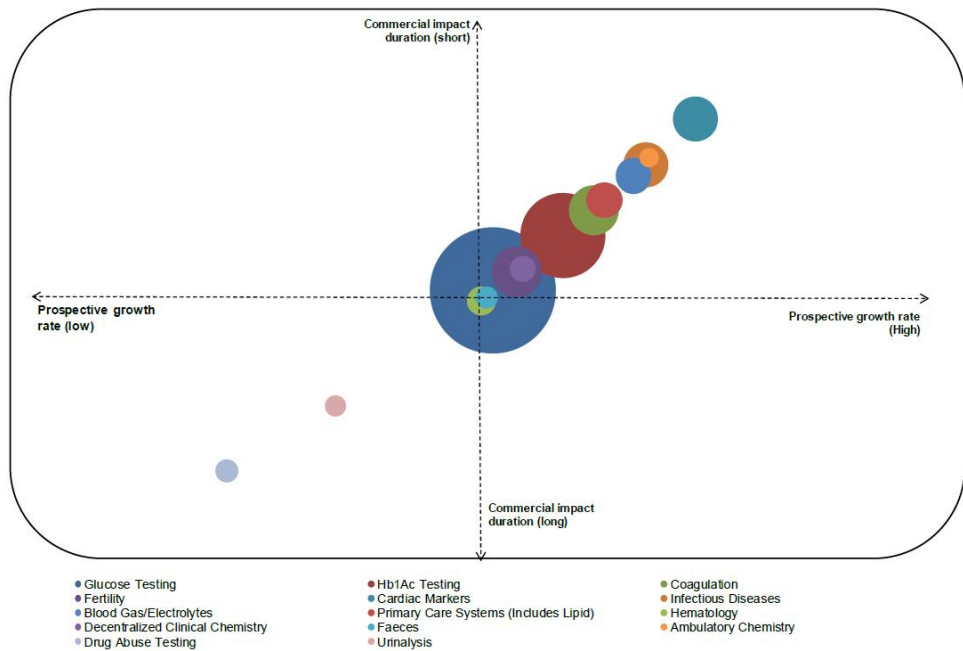
Figure 1-2. Summary of the POCT market [1]. Most of the POCT market share is occupied by the products for diabetes including glucose and HbA1c testing and by the applications for specialized institutions including clinics, hospitals, and healthcare facilities.

Companies	Parameters						
	Company size	Distribution network	Product portfolio	Segment coverage	Geographic presence	Collaborations	Final Score
Abbott Laboratories (Abbott & Alere)	Green	Green	Green	Green	Green	Green	Green
Roche	Green	Green	Green	Green	Green	Green	Green
Siemens Healthcare	Yellow	Yellow	Green	Green	Green	Green	Green
Danaher Corporation (Radiometer, Beckman Coulter)	Yellow	Green	Green	Green	Yellow	Green	Green
bioMerieux	Orange	Orange	Green	Green	Yellow	Green	Green
Johnson & Johnson	Orange	Yellow	Green	Orange	Yellow	Green	Yellow
Nova Biomedical	Green	Green	Yellow	Red	Green	Green	Green
Instrumentation Laboratory	Orange	Orange	Yellow	Green	Yellow	Green	Yellow
Sekisui Diagnostics	Red	Red	Yellow	Green	Yellow	Red	Red
OraSure	Red	Yellow	Yellow	Orange	Red	Yellow	Orange
Qiagen N.V. (AmniSure)	Yellow	Orange	Red	Red	Yellow	Green	Orange
Quidel Corporation	Orange	Orange	Yellow	Orange	Red	Orange	Orange
Abaxis, Inc.	Green	Red	Yellow	Orange	Red	Yellow	Red
Spectral Diagnostics	Orange	Orange	Red	Red	Red	Orange	Red

Legend	Color Scale					
	Very High	High	Med	Low	Very Low	

Source: WHO, IVDtechnology.com, Annual Reports, Investor Presentations, Primary Interviews, Grand View Research

Figure 1-3. Major market participants in the POCT market [1].



Source: Industry Journals, Annual Reports, Investor Presentations, Primary Interviews, Grand View Research

Figure 1-4. Segmental positions of the POCT product in 2015 [1].

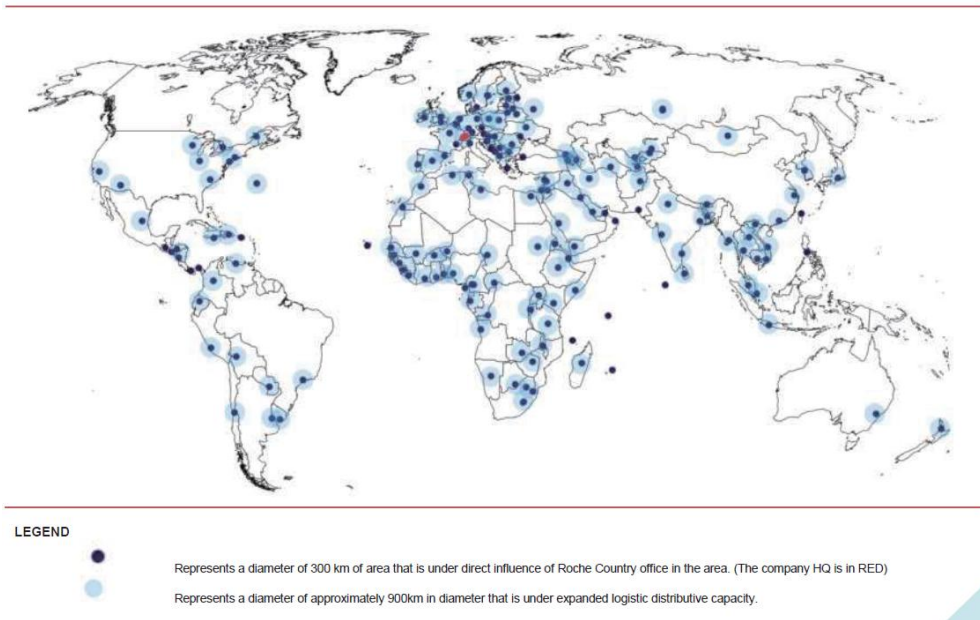


Figure 1-5. Roche distribution presence [1].



Figure 1-6. Werfen Group distribution presence [1].

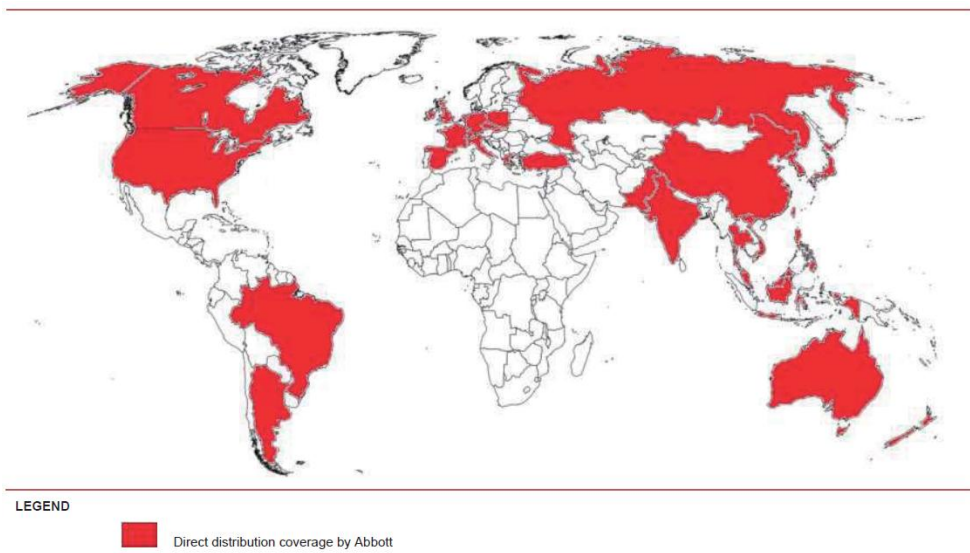


Figure 1-7. Abbott Laboratories distribution network coverage [1].

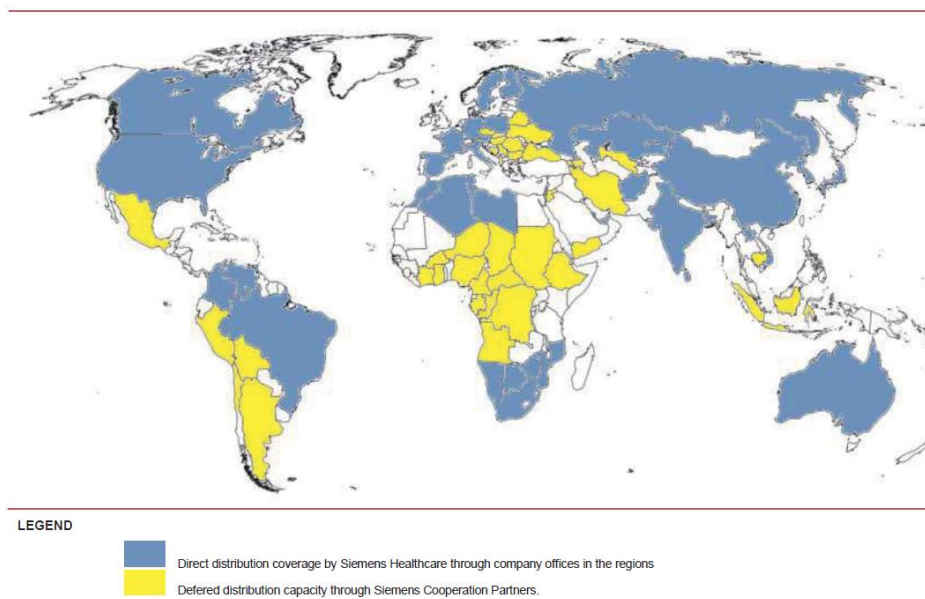


Figure 1-8. Siemens Healthcare distribution presence [1].

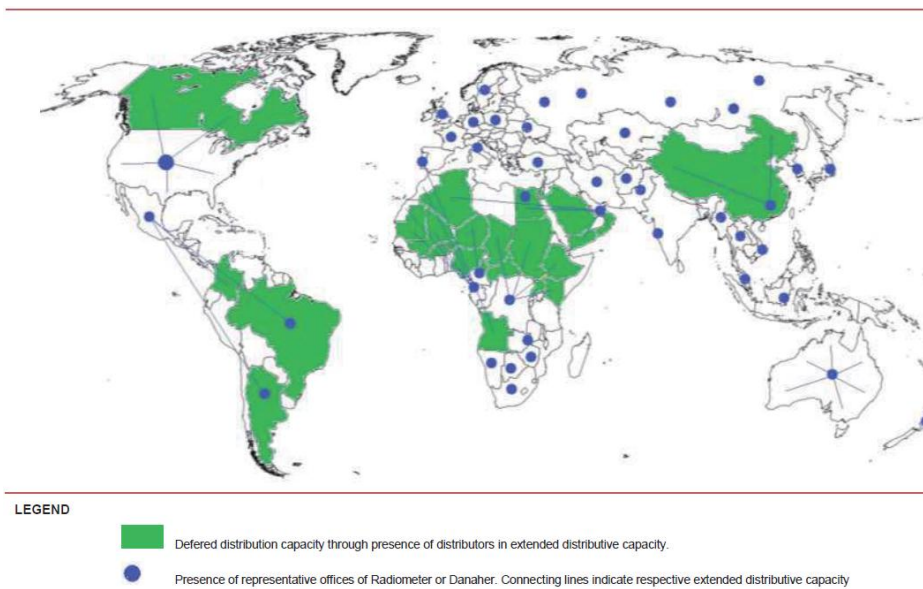


Figure 1-9. Danaher distribution presence [1].

	Operating strategies	Competitive Edge	Weaknesses
Mature players Illumina Inc. Roche Sequencing Oxford Nanopore Technologies	<ul style="list-style-type: none"> ➤ These players are involved in the development of novel platforms that offer portability as well as efficiency of sequencing ➤ R&D pertaining to introduction of companion diagnostics in collaboration with pharmaceutical entities and biotechnology organizations 	<ul style="list-style-type: none"> ➤ Presence of wide product portfolio which covers every range of sequencing platforms and can serve different end-users 	<ul style="list-style-type: none"> ➤ Growing competition and decreasing profitability ➤ Government regulations and stringent approval guidelines for use of NGS as <i>in-vitro</i> diagnostic tests
Emerging players Qiagen Pacific Bioscience Inc. Life Technologies Corporation	<ul style="list-style-type: none"> ➤ Collaborations with the prominent participants in order to develop companion diagnostics and platforms that enable clinical testing in laboratories 	<ul style="list-style-type: none"> ➤ Presence of regional and main headquarters in the untapped and developing market space ➤ Strong product portfolio with respect to the pre-sequencing reagents and solutions 	<ul style="list-style-type: none"> ➤ Absence of skilled personnel ➤ Labor charges ➤ Non-value based reimbursement structure

Source: WHO, U.S. CDC, FDA, NIH Journals, Investor Presentations, Primary Interviews, Grand View Research

Figure 1-10. Categorization of market participants of the POCT industry [1].



Figure 1-11. Smartphone-based POCT sensor devices (a) Wireless blood pressure monitor (BP) developed by iHealth Lab Inc., (b) iHealth BP dock, (c) wireless BP wrist monitor, (d) wireless digital scale, (2)wireless body analysis scale, (f) wireless activity and sleep tracker, (g) wireless pulse oximeter, (h) wireless Smart Gluco-monitoring system, and (i) iHealth Smartphone Algnr [4].

1.2. Competing technologies for POCT application

In the pathological signal processes, including inflammation and tumor metastasis, protease proteins play a crucial role [5][6][7]. For example, cancer cell invasion, metastasis, can occur accompanying extensive proteolysis of the extracellular matrix at the invasive front of a tissue. To degrade the extracellular matrix, the inflammatory cells secrete proteases such as matrix metalloproteinase (MMP) series (MMP2 and MMP9) [8], where MMP expression is promoted by inflammatory cytokines IL-1, TNF- α , and IL-6 [9]. As a result of the pathological signal processes in inflammation and tumor metastasis, the increased concentration of MMP is the factor to be known for the medical applications.

To detect the activity and inhibition of these protease proteins, the novel biosensor designs and measurement techniques which can specify the target proteases are required for the POCT applications. The basic approach is utilizing an enzymatic cleaving reaction between peptide-protease (probe-target) pairs. As proteases can naturally recognize and cleave peptide bonds specifically, the polypeptide can serve as natural protease substrates (probe) [8]. Protease detection methods used in the conventional laboratory convert this cleaving event to a signal readout (usually the optical signal) based on various detection mechanisms. The

conventional optical approach in laboratory includes enzyme-linked immunosorbent assay (ELISA) [9], fluorescent resonance energy transfer (FRET) [10][11], luciferase [12][13] or fluorescent quenching [14][15]. Those sensors are designed to measure the intensity of light signals related to the activity of the proteases which is related with the biological and pathological process.

However, rather than those conventional ones, for portable and compact size of the POCT biosensor platform, the electrical or electrochemical approaches are desirable. The established POCT biosensor platforms are based on field-effect transistor (FET) [16], electrochemical impedance spectroscopy (EIS) [17], surface plasmon resonance (SPR) [18], and square-wave cyclic voltammetry (SWV) [19]. The platforms can exclude complex optical components including light-emitting diodes (LEDs), photodetectors (PDs), optical lenses, and light guide system and only require metal electrodes and dielectric structures in micro-scale. Though there are many key challenges including the plasma separation inside the sensor device, low reproducibility, nonspecific effect, the performance of the electrical POCT devices has been continuously improved. In the table 1.1, the performance of various POCT technologies for sensing of MMP9 is compared. Although it is impossible to compare the performance of the POCT techniques under the same condition, the performance of the FET and SPR based POCT devices may approach that of the commercial ELISA when ruling out the nonspecific effect which is known to be the weakness of the PCT sensors.

Table 1-1. Summary of the sensing performance with various protease biosensor platforms for MMP9 detection.

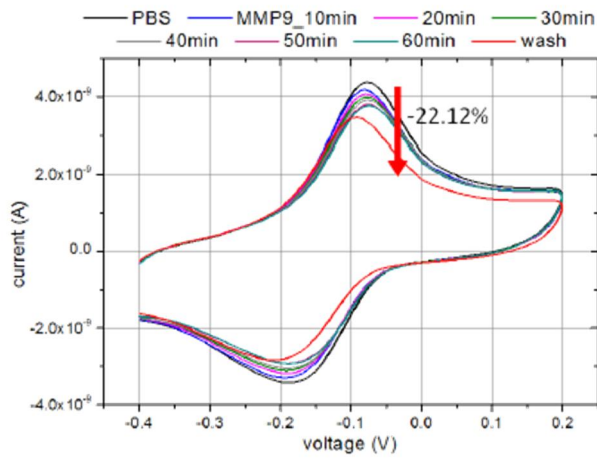
<i>Methods</i>	<i>Detection Limit</i>	<i>Linear Range</i>	<i>Selectivity</i>
Field-effect transistor (FET)	10 pM	10 pM -1 nM	No cross-reactivity with unknown concentration of BSA
Electrochemical impedance spectroscopy (EIS)	0.5 nM	0.5 nM -4 nM	<1% with 2 nM MMP-2
Surface plasmon resonance (SPR)	62.5 pM	62.5 pM -1.22 nM	Not determined
Fluorescence resonance energy transfer (FRET)	0.5 nM	0.5 nM -10 nM	No cross-reactivity with 2.5 nM of MMP-2,3,7
Commercial enzyme-linked immunosorbent assay (ELISA)	2 pM	2 pM -0.24 nM	< 0.5% cross-reactivity < 50% cross species
Square-wave cyclic voltammetry (SWV)	60 pM	60 pM -50 nM	No cross reactivity with 50 nM tumor necrosis factor- α -converting enzyme (TACE) and urokinase-type plasminogen activator (uPA)

1.3. Review of electrochemical biosensor (T-chip) based on electron tunneling

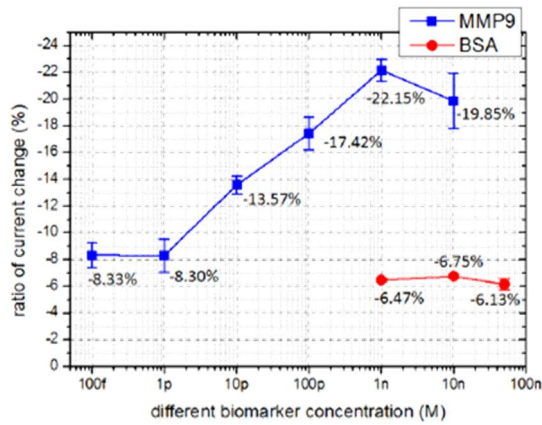
In this dissertation, the electrochemical protease biosensor (T-chip) platform is studied. Due to its unique structural features based on two simple asymmetry electrodes, the T-chip has the advantage when used as a biosensor platform compared to other platforms. By introducing the *self-gating effect* [20], [21], the T-chip platform can exclude the external reference electrode [22] which is essential electrode component in the conventional three-electrode electrochemical system for stabilizing the electrostatic potential of the electrolyte.

The motivation of the research has come from that of the Shin's group [19] and the previous research on T-chip in our group focused on the detection of MMP9 [22], [23] and MMP2 [24] for the specific applications diagnosing the cancer. This reference-electrode free structure with the simple two-electrode device utilizes the electron tunneling phenomenon between its gold electrode and geometrically fixed redox states. To measure and monitor the electron tunneling current, the cyclic-voltammetry (Cyc-V) measurement was used. In Fig. 1-12, the I-V characteristics of Cyclic voltammetry results after injecting 1 nM MMP9 solution and the ratio of current decreases (calibration curve) in different concentrations of MMP9 and BSA

after 1 hour are shown. In Fig. 1-13 the I-V characteristics of Cyclic voltammetry results after injecting human serum solution and the ratio of current decreases (calibration curve) in different concentrations of MMP2 in human serum after 1 hour are shown.

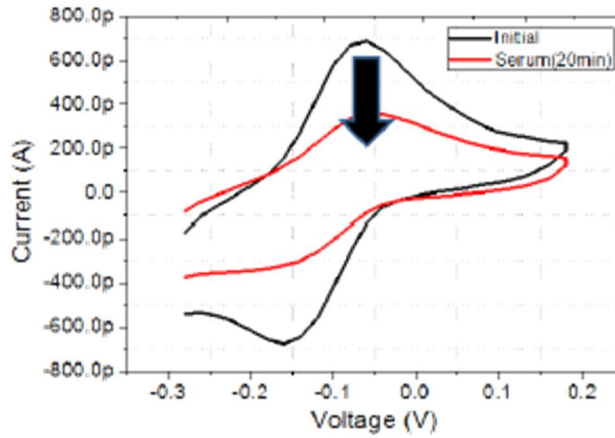


(a)

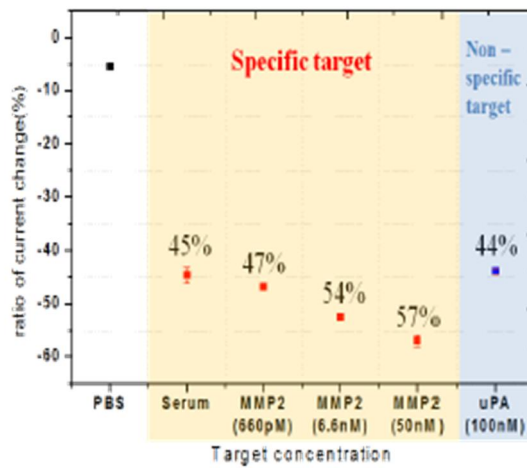


(b)

Figure 1-12. (a) I-V characteristics of Cyclic voltammetry results after injecting 1 nM MMP9 solution, (b) Ratio of current decreases (calibration curve) in different concentrations of MMP9 and BSA after 1 hour.



(a)



(b)

Figure 1-13. (a) I-V characteristics of Cyclic voltammetry results after injecting human serum solution, (b) Ratio of current decreases (calibration curve) in different concentrations of MMP2 in human serum after the reaction for 1 hour.

Chapter 2.

T-chip

This chapter describes the fabrication process of the T-chip platform. The reference electrode-free electrochemical biosensor device with an asymmetric two electrode system is the unique feature of the T-chip device. The gold electrodes are formed on the silicon dioxide layer by using the standard CMOS and MEMS fabrication processes.

2.1. Device fabrication and structure of T-chip

The T-chip device with one metal layer was fabricated at the Inter-University Semiconductor Research Center (ISRC) in Seoul National University using standard CMOS and MEMS fabrication processes. The 4-inch bare N-type silicon wafer with a resistivity of 1-20 $\Omega\cdot\text{cm}$ was used as a substrate. The whole fabrication process is

as follows.

Residual organic materials on the bare wafer were removed by Sulfuric acid and peroxide mixture (SPM) cleaning. The metal impurities on the wafer were removed by NSC-1 (Standard Cleaning-1) NH_4OH solution and SC-2 (Standard Cleaning-2) HCl solution. The native oxide on the wafer surface was cleaned by using Hydrofluoric acid (HF) cleaning. As an insulating substrate with hydrophilicity on the surface, the silicon dioxide (SiO_2) layer of 1 μm thickness was grown by the high-temperature wet-oxidation process with Tetraethoxysilane (TEOS) at 900 $^\circ\text{C}$ for 10 hours.

To form the M-1 metal electrode structure, photolithography, metal evaporation, and lift-off process were performed. First, the negative photoresistor (PR) was spin coated on the oxidized wafer surface. After soft-baking process, the PR coated wafer was exposed to the patterned ultra-violet (UV) illumination through the soda-lime Cr photomask with 10 μm of the minimum line width by using aligner MA6-III (i-line, 365 nm). After development and hard-baking process, the patterned PR structure was formed. Second, by using E-gun evaporator, 50 \AA thick of Ti as an adhesion layer and 2000 \AA thick of Au electrode layer were evaporated on the wafer surface through the patterned PR structure. Finally, the PR structure was removed leaving the patterned M-1 metal electrodes by lift-off process with ultrasonication in acetone solution for 30 minutes.

The 5 mm x 5mm die chip was separated from the wafer by dicing process [25]. The final device structure consists of 200 nm thick of concentric gold electrode arrays on the 1 μm thick of TEOS SiO_2 layer. On the top of the hydrophilic die chip surface, a PDMS block with a thickness of 3 mm was located providing a well structure for biochemical experiment. The total process of the chip fabrication is listed in table 2-1 and schematically described in Fig. 2-1.

Table 2-1. Fabrication process of the T-chip device.

No.	Process	Remark
01	W13A(WA-13,C1-6) SPM-CLEANING	Sulfuric acid and peroxide (SPM) mixture. To remove residual organic material.
02	W5A(WA-5,C1-6) SC-1,2 CLEANING	Hydrofluoric acid (HF) cleaning To remove the thin oxide layer and some fraction of ionic contaminants.
03	CMOS FURNACE I WET OXIDATION	To produce silicon dioxide layer using Tetraethoxysilane (TEOS) process.
04	MEMS SPIN COATING	Negative Photoresist (PR).
05	MASK ALIGN AND UV EXPOSURE (MA6-III)	Soda-lime and Cr Mask with 10 μm of the minimum line with UV exposure with the aligner MA6-III 365 nm (i-line).
06	MEMS WET-STATION /WS-18A,DEVELOP	Development of the patterned PR.
07	E-GUN EVAPORATOR	Ti/Au : 50/2000 \AA .
08	PHOTORESISTOR LIFT-OFF	30 min sonication with the ultra-sonic in acetone. 10 sec DIW rinsing.
09	DICING SAW II(SI)	5 mm x 5 mm device dicing with Sawing machine II.

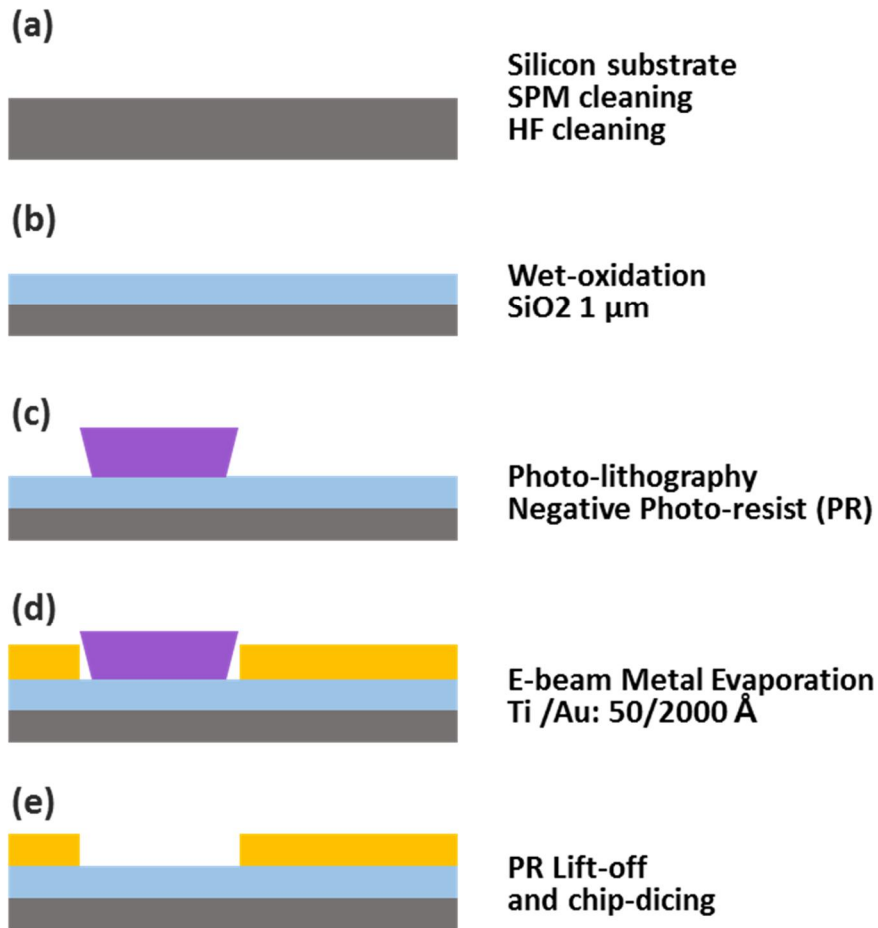
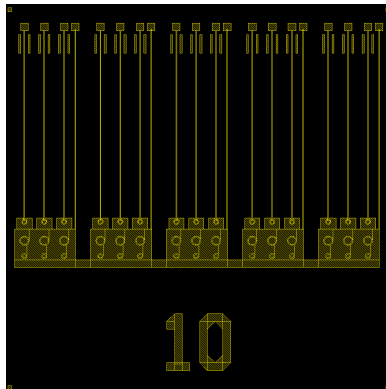
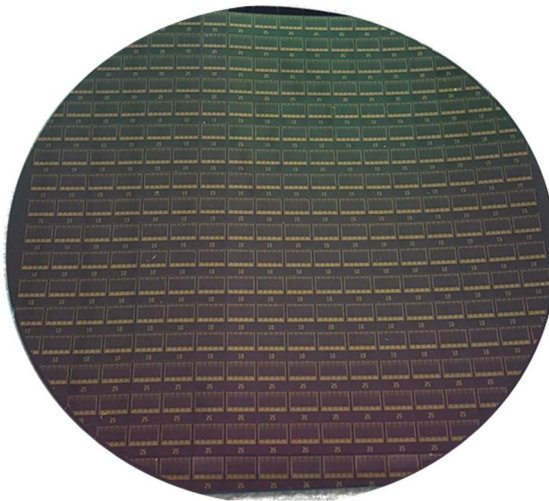


Figure 2-1. Illustration of the total fabrication process of the T-chip device. (a) Cleaning process, (b) TEOS wet oxidation, (c) photolithography, (d) E-gun metal evaporation, (e) lift-off process and chip-dicing.



(a)



(b)

Figure 2-2. (a) Lay out of the T chip having the size of 5 mm x 5 mm. (b) the fabricated 4-inch wafer after dicing process.

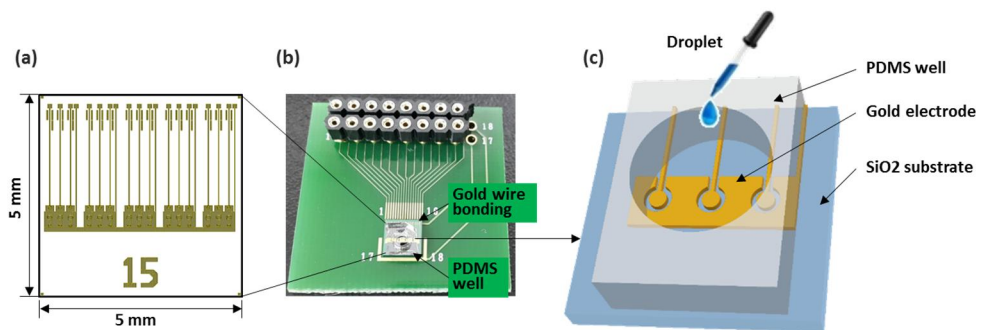


Figure 2-3. (a) Layout of the T-chip device. (b) T-chip mounted on the PCB board. (c) Schematic of T-chip integrated with the PMDS well.

2.2. Immobilization of probe peptide

The sequence of the peptide (Gly-Pro-Leu-Gly-Met-Trp-Ser-Arg-Cys; GPLGMWSRC) was selected as the self-assembled monolayer (SAM) [19], [22], [26] and its end terminal was modified with Methylene blue (MB) as a redox molecule. The detailed immobilization process are same as the references [22], [26] and summarized as follows.

The bare device with the gold electrodes was cleaned by sonicating in acetone for 10 minutes. After the sonication, the device was washed thoroughly with isopropanol, ethanol and DI water for 5 minutes respectively, and then dried with a stream of nitrogen. The cleaned gold electrodes were incubated in 1 M of MB-peptide diluted solution with dimethyl sulfoxide (DMSO) at room temperature for 2 hours. After washed with DI water for 30 s and dried with the stream of nitrogen, the electrodes were incubated in 1 mM of 6-mercapto-1-hexanol (MCH) diluted solution with Dulbecco's phosphate-buffered saline (DPBS) for 1 hour. Finally, the electrodes were washed with DI water and dried again. A polydimethylsiloxane (PDMS) well was mounted on the device surface to prevent the solution from flowing over the surface of the device and to provide the micro-chamber for biochemical reactions.

We injected Dulbecco's Phosphate-Buffered Saline (DPBS) droplet of 10 μL into the PDMS well to initialize the device. Finally, at the electrode surface, metal-insulator-electrolyte (MIE) structure is constructed where each component corresponds to gold, peptide-SAM, and electrolyte solution with space charge region (SCR). The geometrical and physical similarity between the MIE and the metal-oxide-semiconductor (MOS) will be discussed in chapter 4 by measuring the electrical characteristics and presenting their equivalent circuit.

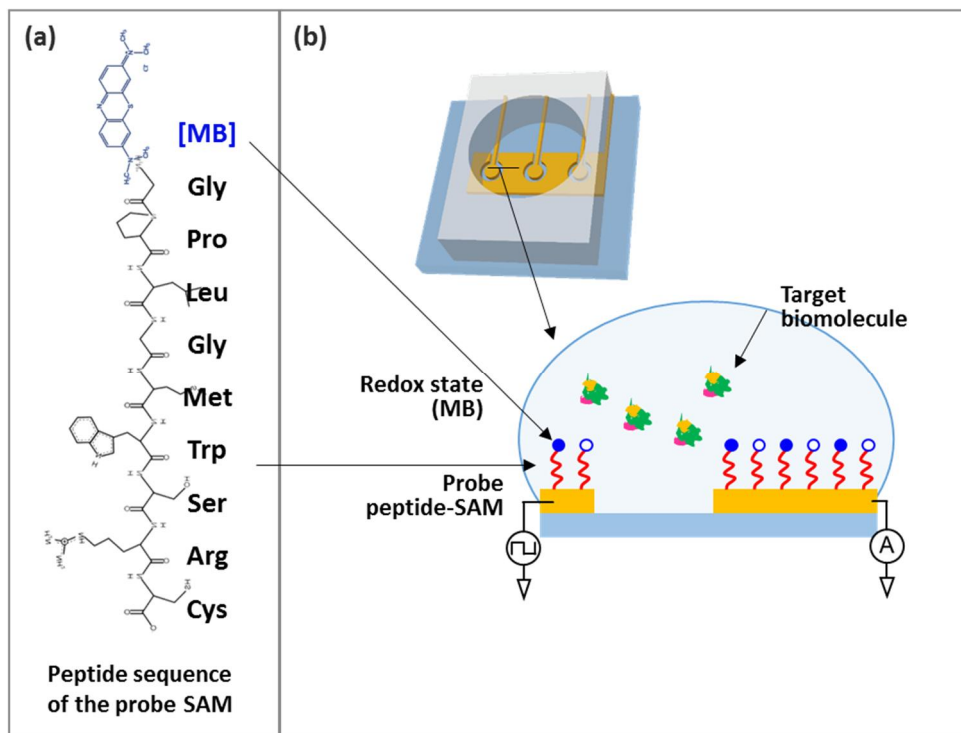


Figure 2-4. (a) Sequence of probe peptide. Methylene blue (MB) is modified at the end of the peptide. Thiol of Cys was used to immobilize the peptide on the gold electrode by forming the Au-thiol covalent bond. (b) Schematic of the electrode surface.

2.3. Reference electrode-free electrochemical device

The self-gating effect has been reported by our group to indicate that the electrostatic potential of the electrolyte solution is stabilized by the capacitive coupling with the surrounding electrode through the electric double layers (EDL). The value of the EDL capacitance is proportional to the area of the electrode[20]–[22], [26]. Accordingly, the electric potential of the bulk electrolyte solution is determined by the ratio between the two capacitance values: one residing at the surface of the working electrode and the other at the surface of the counter electrode. Since the capacitance value of the counter electrode is much larger than that of the working electrode, the electric potential of the bulk electrolyte solution is strongly capacitive-coupled with the electrical potential of the counter electrode.

By introducing the self-gating effect, the potential of the bulk electrolyte solution can be stabilized by that of the counter electrode, thereby the reference electrode can be excluded. This two electrode system is the unique feature of the T-chip device compared with the conventional electrochemical devices with three-electrode system including the external reference electrode.

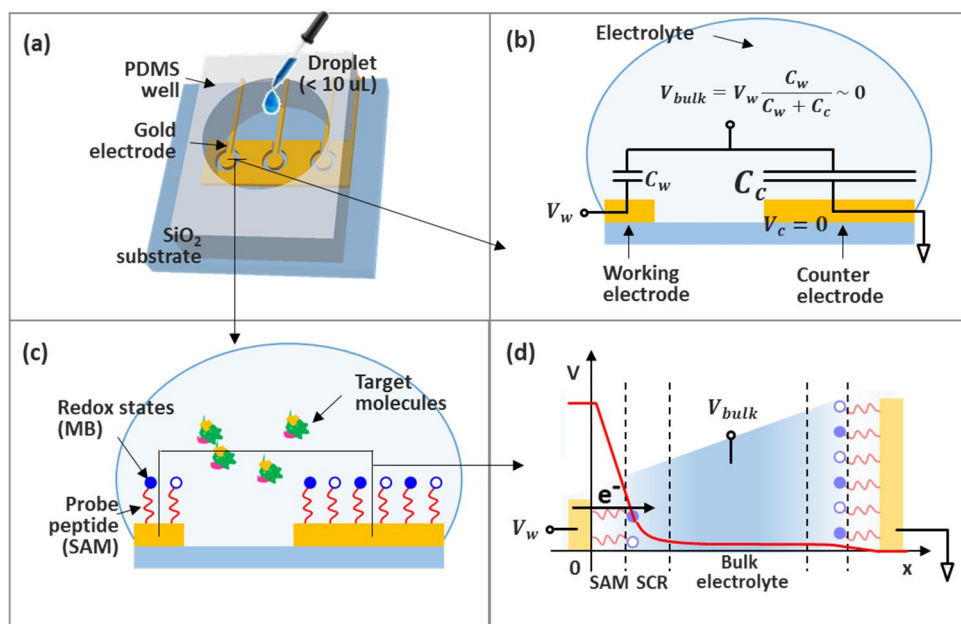


Figure 2-5. (a) Reference electrode-free device (T-chip) and its concentric electrode structure. (b) Due to the area asymmetry of the electrodes, the electrical potential of the bulk electrolyte is stabilized by capacitive coupling, called “self-gating effect.” (c) MB-modified peptide SAM is immobilized on the gold electrode. (d) Potential profile from the working electrode to the counter electrode. Most of the potential drop occurs through the SAM and SCR.

2.4. Strategy for detection of biomarkers

The T-chip device, protease biosensor, platform adopts the peptide as a probe molecule. As mentioned in the previous chapter, the peptide biosensor platform can detect the proteins generally enzymes present in the electrolyte solution as a target molecule. The sequence of the probe peptide was designed to be cleaved by the target protein with specificity. Therefore, the target protein cleaves the probe peptide with a high selectivity. Additionally, the redox molecule, here methylene blue (MB) is modified at the end of the probe peptide. The MB state can capture and release the electrons from the metal electrode. By controlling the electric potential of the electrode, we can measure the tunneling current, which indirectly indicates the state of the probe peptide. If the measured tunneling current does not change, we understand that the number of the peptides cleaved are negligible. After the target-probe reaction, the number of the MB states reduces once the fragment of the peptide diffused from the electrode surface. The reaction event is closely related with the intensity of the tunneling current that we measure.

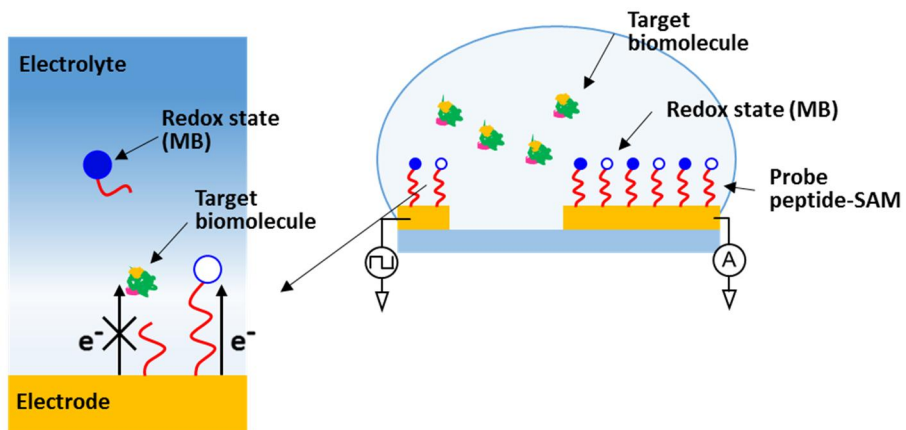


Figure 2-6. Illustration of the target-probe cleaving event. The target biomarker (protease or enzyme) cleaves the probe peptide. After the target-probe reaction, the number of the fixed MB states on the electrode surface reduces once the fragment of the peptide diffused from the electrode surface. The reduction of the tunneling current indicates the concentration of the target biomolecules.

2.5. Target biomarker: Trypsin

There are many biomarkers for the protease biosensor platform. The series of matrix metalloproteinase (MMP) are one example. In this research, Trypsin [27], [28] a member of the trypsin family of serine proteases, which is secreted by the pancreas was chosen as an exemplar target biomolecule. Since the discovery of its stable enzymatic property in cleaving the carboxyl side of the amino acid arginine, Trypsin has been used to evaluate the performance of the protease biosensors. [29] The concentration of Trypsin was varied from 0 to 100 nM in the DPBS solution.

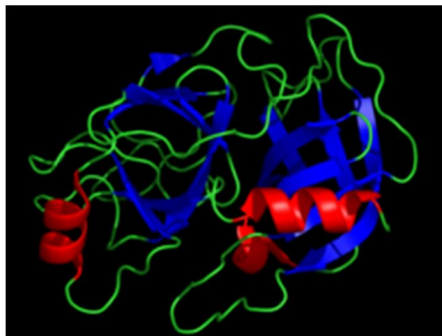


Figure 2-7. Crystal structure of bovine Trypsin (EC 3.4.21.4) [23]. Trypsin is one of the serine protease and it found in the digestive system of vertebrates.

Chapter 3.

Electrochemical characteristics of T-chip

3.1. I-V characteristics of T-chip

Cyclic voltammetry (Cyc-V) is one of the general and conventional technique for the characterization of the electrochemical devices. By sweeping a stair-case voltage signal, the basic electrochemical properties of the T-chip device were measured by using Agilent 4156C. The schematic illustration of the I-V characteristics (see Fig. 3-1) of the bare, peptide (pep-SAM), and peptide-MB-SAM (pep-MB-SAM) devices and their structures are shown in Fig. 3-2.

The electrical potential is applied to the working electrode. The voltage is varied from -0.4 V (hold time 5 s) to 0.2 V with 0.02 V steps (delay time 200 ms and scan rate 1 V/s) while the counter electrode was grounded and the electrical potential of the bulk solution is stabilized with that of the counter electrode. The measured current value was sampled for 16.6 ms of integration time at the end of the

voltage stairs with 200 ms of duration.

The measured I-V characteristics of various sensor devices with bare electrode, electrodes decorated with pep-SAM, and pep-MB-SAM devices are shown in Fig. 3-3. In the case of the bare electrode, the combination of the remaining capacitive current of the EDL and the leakage current due to weak electrolysis is plotted with the black line. The current value decreased after immobilizing the pep-SAM layer on the electrode surface as plotted in the red line. In addition, with the MB modification at the end of the pep-SAM, the peak current shape appears where the electron tunneling occurs between the gold electrode and the MB (redox) states according to their energy level and occupancy of the MB states. The tunneling current is proportional to the multiplication of electron tunneling rate and the concentration of the redox states. The electron tunneling rate is expressed as [30]

$$k_f = \frac{4\pi^2}{h} |M|^2 D_S \int f(E) D_{ox} dE \quad (3.1.1)$$

$$k_b = \frac{4\pi^2}{h} |M|^2 D_S \int [1 - f(E)] D_{red} dE \quad (3.1.2)$$

where k_f and k_b are the forward and reverse electron tunneling rates. The density of states of substrate, oxidized, and reduced redox sites are D_S , D_{ox} , and D_{red} , respectively. $|M|$ represents the electronic coupling between oxidized and reduced species and h is Plank's constant. The Fermi-Dirac distribution is the function of the electron energy $f(E)$. Finally, we arrives at the expression of the electron tunneling, I_t , which is expressed as the time derivative of the concentration of the

unoccupied MB states, $[MB^+]$, or the occupied LMB states, $[LMB^0]$.

$$\begin{aligned} I_t &= -q \frac{d[MB^+]}{dt} \\ &= -q(k_f[MB^+] - k_r[LMB^0]) \end{aligned} \quad (3.1.3)$$

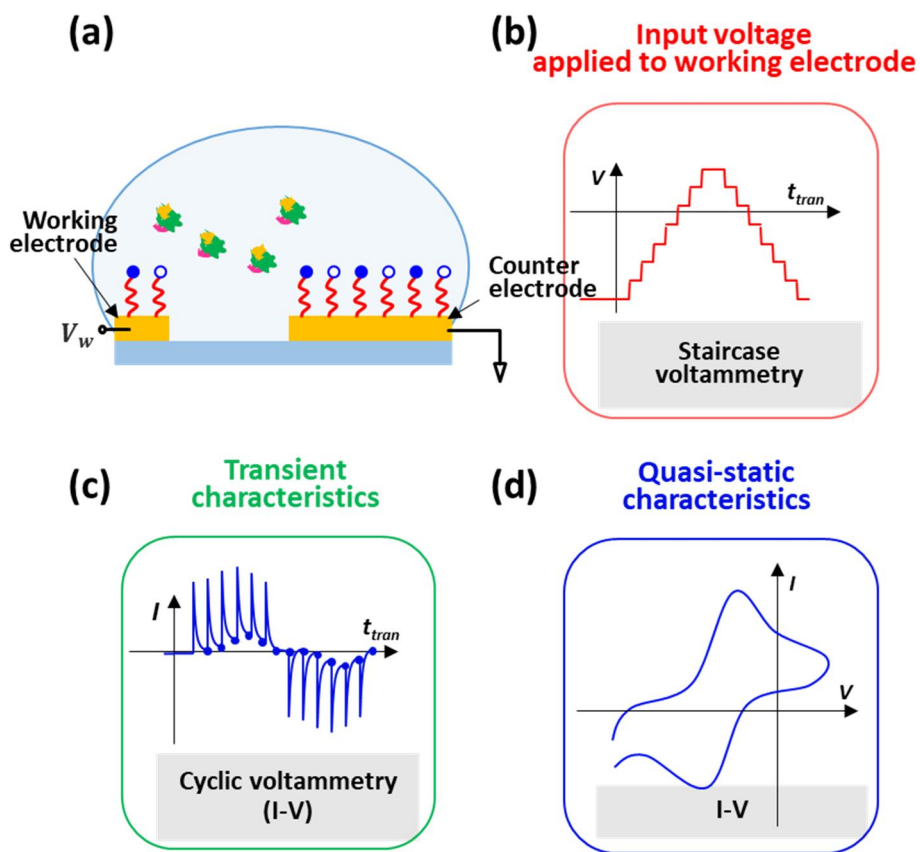


Figure 3-1. Schematic illustration of (a) the T-chip device, (b) Stair-case input voltage, (c) its transient current characteristic, and (d) I-V characteristics of the T-chip device.

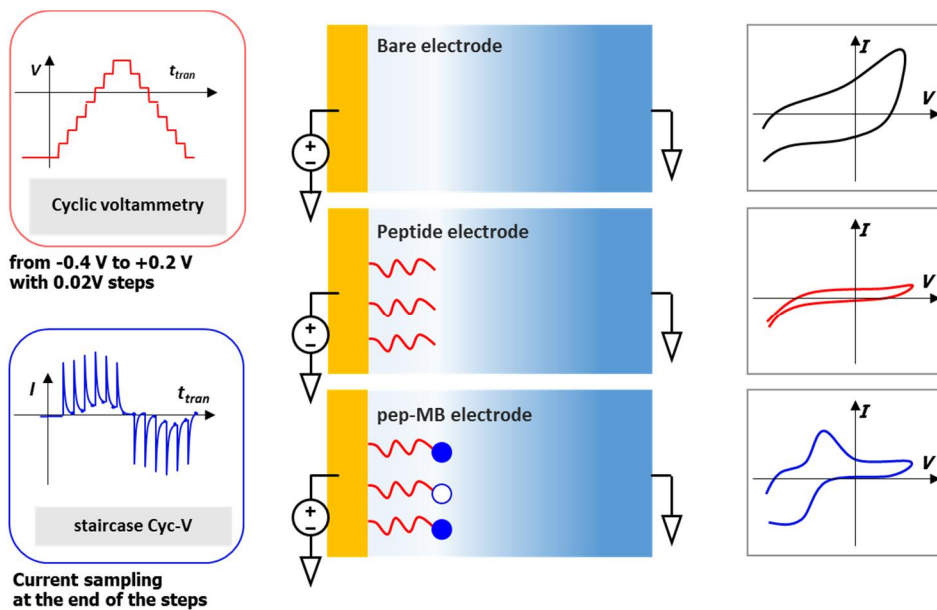


Figure 3-2. Schematic illustration of the I-V characteristics of the bare, peptide (pep-SAM), and peptide-MB-SAM (pep-MB-SAM) devices and their structures.

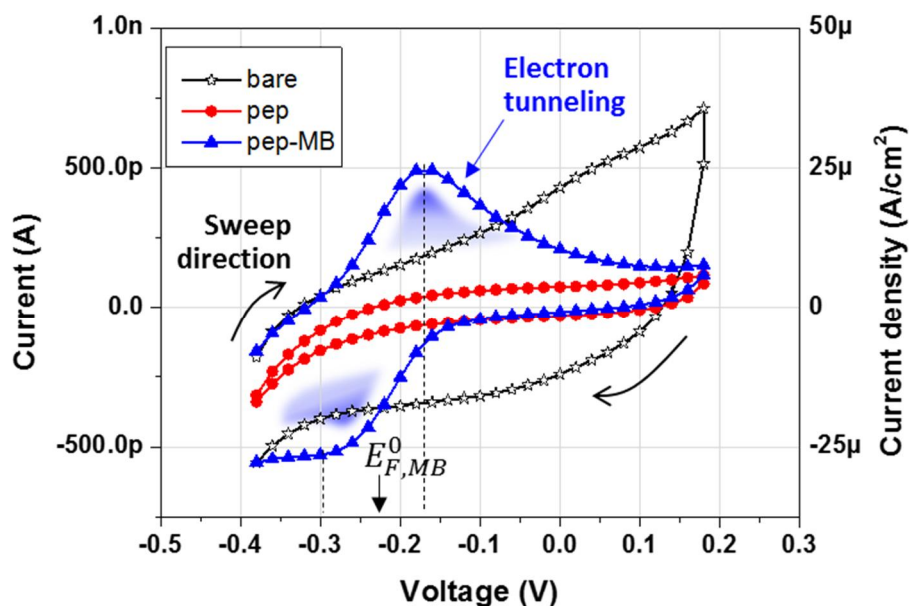


Figure 3-3. Measured I-V characteristics of the bare (black), pep-SAM (red), and pep-MB-SAM (blue) devices. In the case of the bare electrode, the combination of the remaining capacitive current of the EDL and the leakage current due to weak electrolysis is plotted in the black line. Both current value decreased after immobilizing the pep-SAM layer on the electrode surface as plotted in the red line. Without MB modification (red) only capacitive and leakage background current is observed. With MB modification (blue) the tunneling event occurs. The electrical potential applied to the working electrode was varied from -0.4 V (hold time 5 s) to 0.2 V with 0.02 V steps (delay time 20 ms and scan rate 1 V/s) while the counter electrode was grounded.

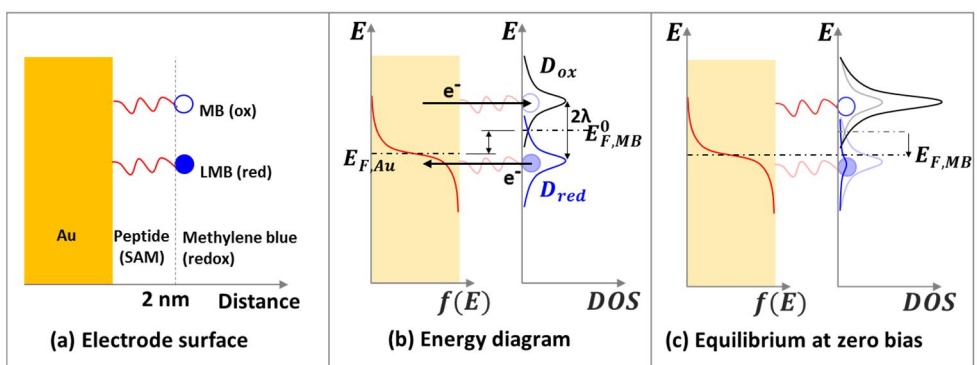


Figure 3-4. Schematic illustration of (a) peptide-MB immobilized on the gold electrode and (b and c) its energy band diagram.

3.2. C-V characteristics of T-chip

The useful information from the T-chip device other than the IV characteristics can be obtained from the capacitance-voltage (C-V) characteristics. Different from the Cyc-V measurement which measures the current values of the device, the quasi-static capacitance-voltage (QSCV) measurement measures the capacitive components of the metal-electrolyte interface. The QSCV technique has been known to be one of the general and conventional techniques for the characterization of solid-state devices, especially metal-oxide-semiconductor (MOS). By sweeping a staircase voltage signal to the working electrode, the capacitive characteristics of the T-chip device were measured by using Agilent 4156C. The schematic illustration of the C-V characteristics (see Fig. 3-5) of the bare, peptide (pep-SAM), and peptide-MB-SAM (pep-MB-SAM) devices and their structures are shown in Fig. 3-6.

As same in the case for the Cyc-V measurement, the electrical potential profile applied to the working electrode was swept and varied from -0.4 V (hold time 5 s) to 0.2 V with 0.02 V steps (delay time 200 ms and scan rate 1 V/s) while the counter electrode was grounded and the electrical potential of the bulk solution is stabilized with that of the counter electrode. The measured capacitance value was sampled by integration the current divided by the step voltage. The measured C-V characteristics

of the bare, pep-SAM, and pep-MB-SAM devices are shown in Fig. 3-7. In the case of the bare electrode, the nonlinear and asymmetric electric double layer (EDL) capacitance which consists of the stern layer capacitance and the diffusion layer capacitance, is plotted in the black line. The capacitance plot becomes quite symmetrical as plotted in the red line for the device after immobilizing the pep-SAM layer on the electrode surface. In addition, with the MB modification at the end of the pep-SAM, the peak capacitance shape appears when the electron tunneling occurs between the gold electrode and the MB (redox) states according to their energy level and occupancy of the MB states. The detailed explanation of the C-V characteristics will be given in the next chapter.

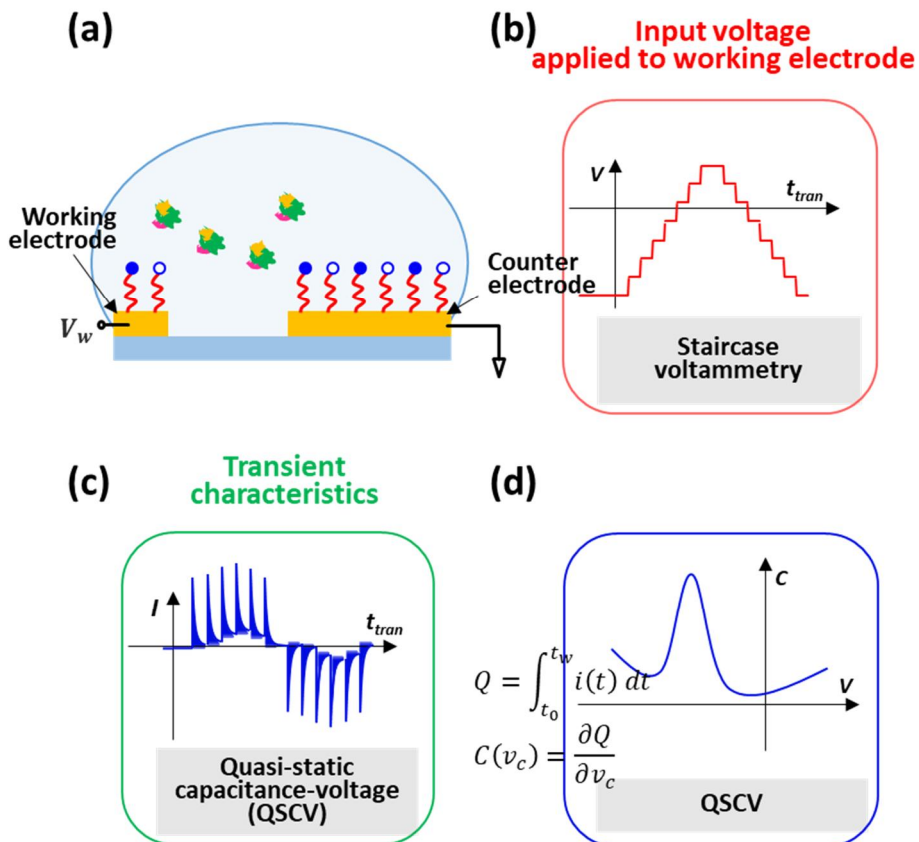


Figure 3-5 Schematic illustration of (a) the T-chip device, (b) Stair-case input voltage, (c) its transient current characteristic, and (d) C-V characteristics of the T-chip device.

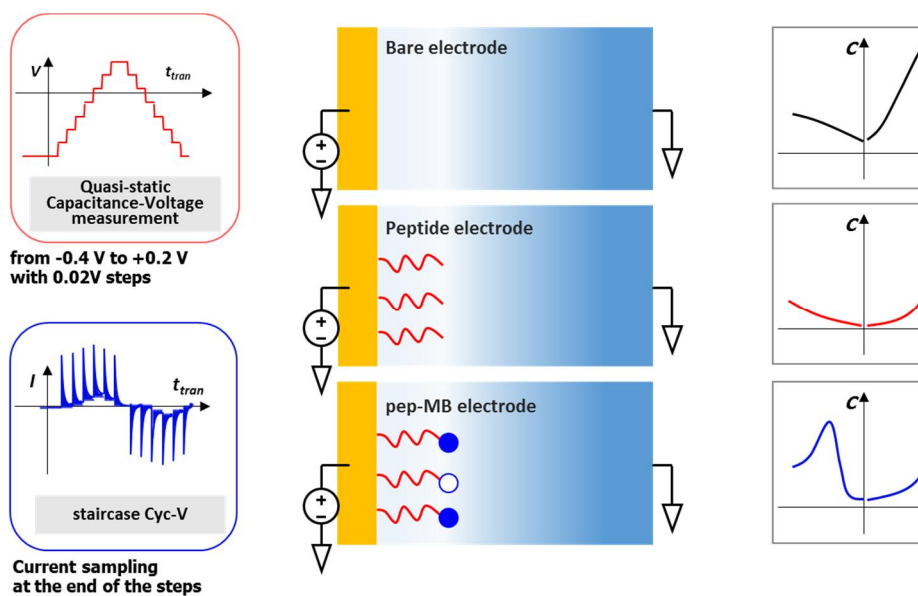


Figure 3-6. C-V characteristics of the various devices with different surface conditions. The potential of the working electrode was swept from 0 V to -0.5 V and +0.5 V.

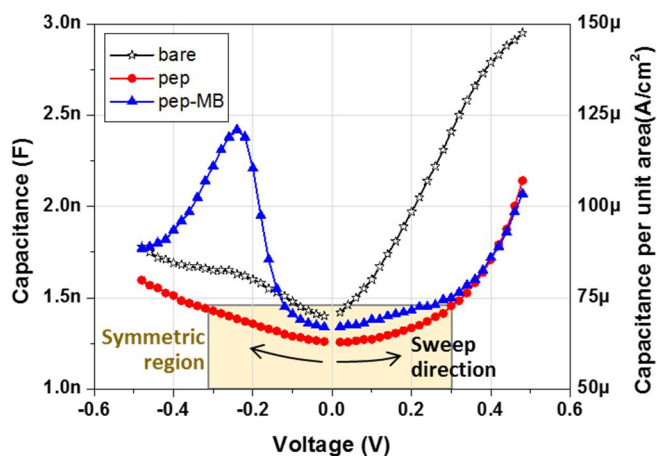


Figure 3-7. C-V characteristics of the various devices with different surface conditions. The potential of the working electrode was swept from 0 V to -0.5 V and +0.5 V and the counter electrode was grounded. The bare electrode shows either nonlinear and asymmetric profile. (the black) After introducing peptide SAM on the metal electrode, the capacitance become quite symmetric (the red). By facilitating this symmetrized capacitance, the capacitive current can be eliminated and the tunneling current can be extracted in the pulse method. The existence of the MB states is observed in the negative bias region indicating that the standard redox energy level of the MB is higher than the Fermi level of the gold electrode. The MB state can be considered as the trap state (donor-like) which is similar to the interface or oxide trap of the solid state devices. It can be described as the capacitance, C_q .

Chapter 4.

Metal-insulator-electrolyte capacitor

4.1. Similarity between metal-insulator-electrolyte (MIE) and metal-oxide-semiconductor (MOS) capacitors

As aforementioned, the electric potential of the bulk electrolyte solution in the T-chip device can be stabilized by that of the counter electrode. By considering the electrical potential of the bulk electrolyte is grounded by “self-gating effect”. In this chapter, taking the advantage of “self-gating effect”, the electrolyte solution of the metal-insulator-electrolyte (MIE) can be regarded as a bulk semiconductor material of the metal-oxide-semiconductor (MOS) structure.

Because most electrical potential drops at the working electrode side of the T-chip, the major electrical and electrochemical phenomena can be expected to occur between the SAM layer on the working electrode. The cross-section view of the T-chip device and the electrical potential profile across through the device are

illustrated in Fig. 4-1. The vertical cross-section view of the T-chip device nearby the working electrode is shown in Fig. 4-2. From the figures, it is of note that both MIE and MOS capacitors have a similar structure. The peptide SAM and the electrolyte of MIE can correspond to the oxide and the semiconductor of MOS respectively since the peptide layer can be considered as a dielectric material as if the oxide layer with a dielectric constant.

The electrolyte solution with cations (positive ions) and anions (negative ions) can be considered as a counter-doped semiconductor material with a high concentration of the positive and the negative mobile charges. Those charges move at the interface of the metal electrode according to the electrical potential. The distribution of the charges can be predicted by the Poisson-Boltzmann equation, which causes the nonlinearity on the capacitance-voltage characteristics.

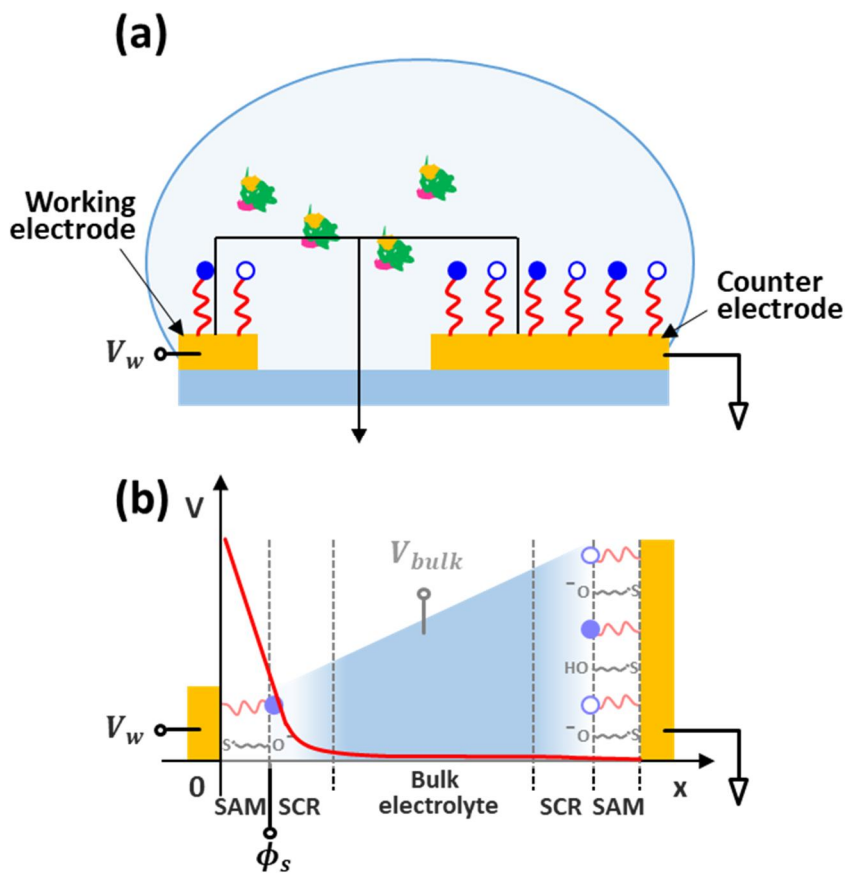


Figure 4-1. (a) Schematic illustration of the T-chip device and (b) electrical potential profile across the T-chip device.

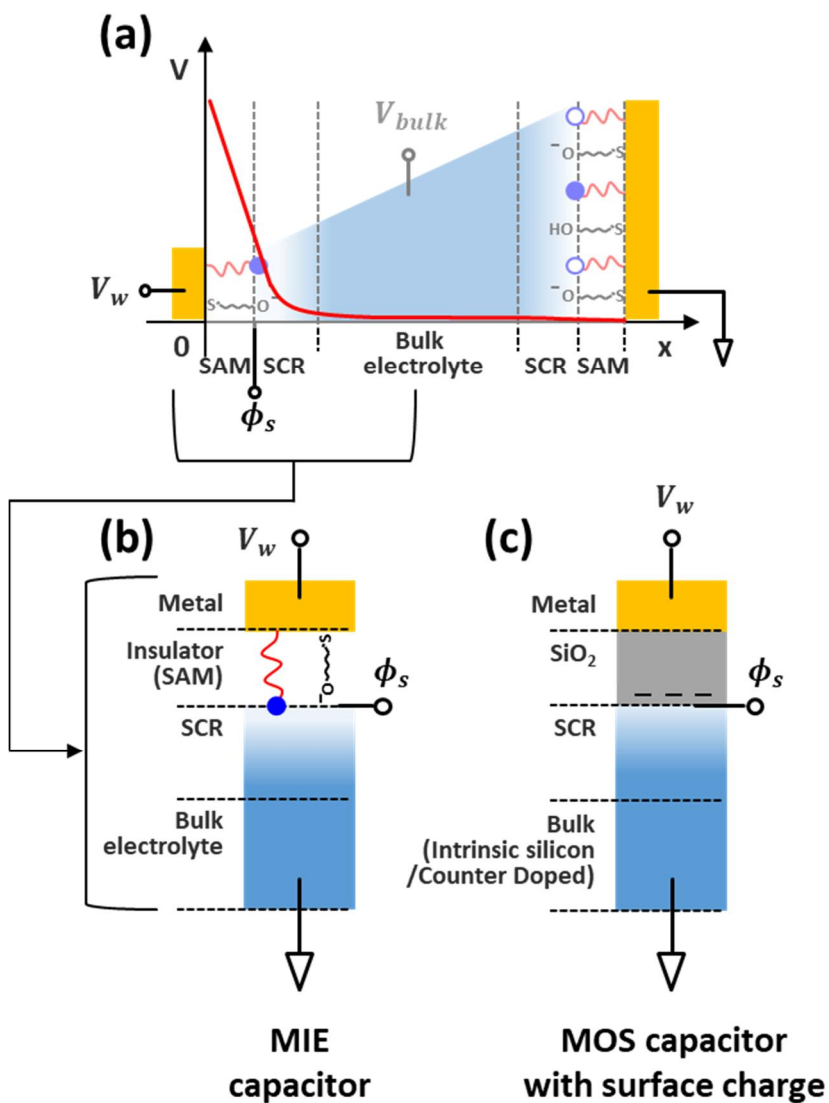


Figure 4-2. (a) Electrical potential profile across the T-chip device, (b) cross-sectional view of the T-chip device nearby the working electrode, which can be considered the MIE capacitor, and (c) that of the MOS capacitor structure.

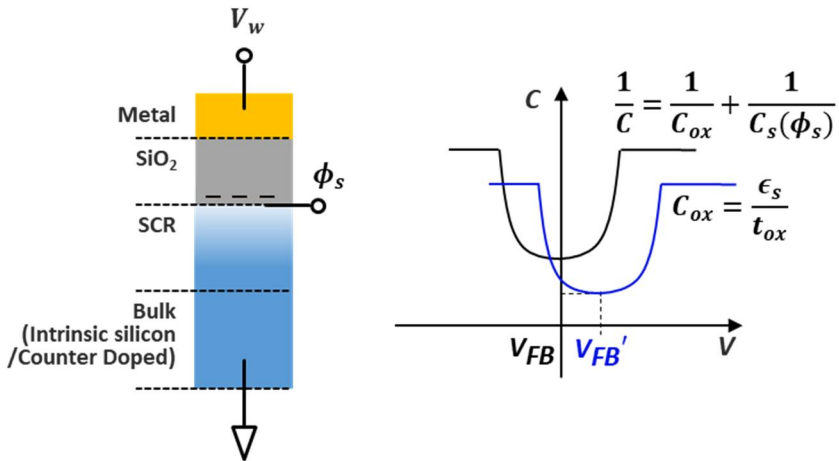
4.2. Concept of flat-band voltage

From the structural similarity and correspondence of the components of the MIE and the MOS capacitor devices, the basic concept, flat-band voltage, can be introduced to analysis of the T-chip device. The concept of flat-band voltage, which is the gate voltage applied to make the surface field to be zero, indicates the electrical potential difference between the metal gate and the bulk semiconductor when the energy band at the oxide-semiconductor interface and the semiconductor layer becomes flat and there is no net charge present.

In the MOS device, the flat-band voltage equals the work function difference between the gate metal and the semiconductor. However, in the MIE device, there is no work function and energy band structure of the electrolyte solution which corresponds to the semiconductor in the MOS device. The discrete redox states of hydrogen and oxygen ions in water solution can be used as if both conduction and valence band edge of the semiconductor respectively. In Figs. 4-4 and 4-5, both the MOS and MIE structure and their band diagram are schematically illustrated. In these figures the oxide layer containing the negative fixed charge corresponds to the peptide SAM with the negative hydroxyl group at the end of the MCH layer.

Because there is fixed negative charges at the oxide-semiconductor interface and the peptide SAM-electrolyte interfaces, the band edges of both MOS and MIE structure are initially curved upward under the zero-bias condition. In this case, the flat-band voltage can be defined as the working electrode voltage when the net charge is zero at the interfaces.

a) Metal-Oxide-Semiconductor (MOS)



b) Metal-Insulator-Electrolyte (MIE)

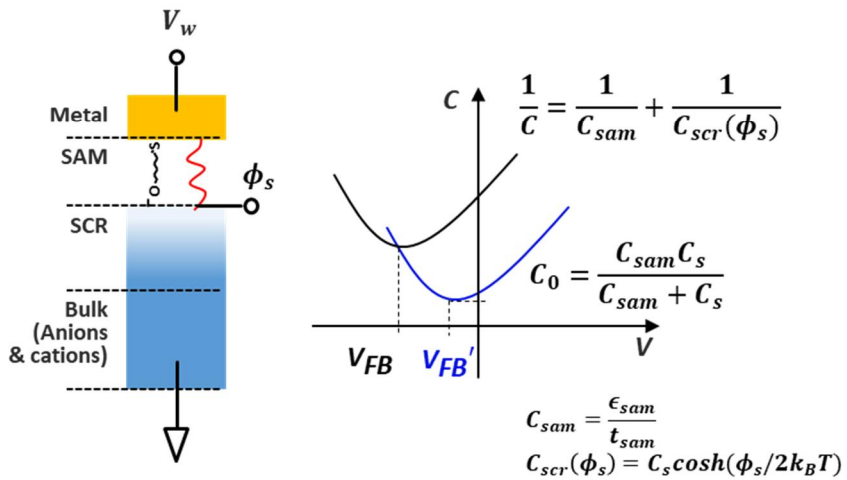


Figure 4-3. Schematic illustration of the (a) MOS and (b) MIE capacitors and their C-V characteristics. The concept of the flat-band voltage shift can be introduced.

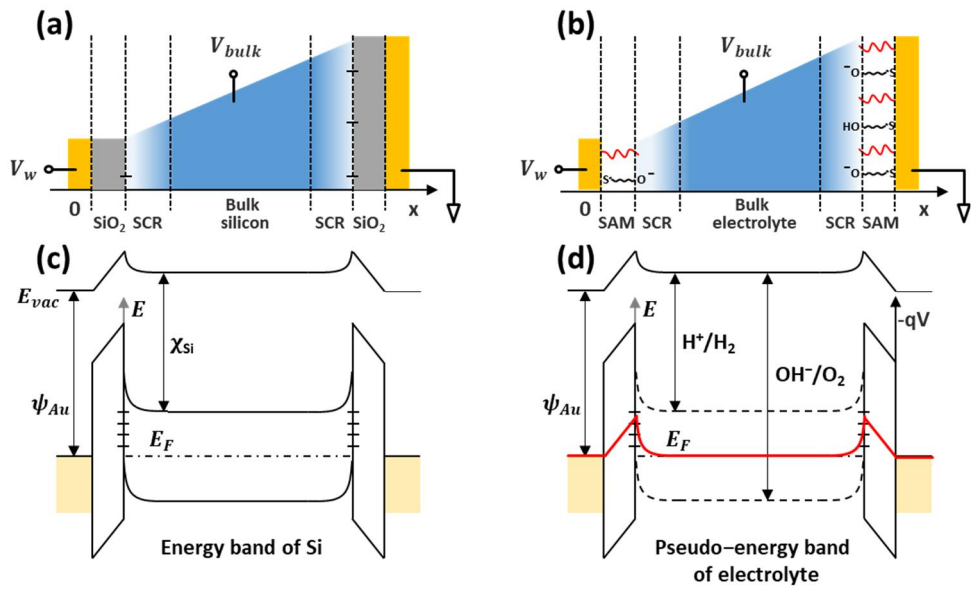


Figure 4-4. Energy band diagram and pseudo-energy band diagram of the MOSOS and MIEIM structure with negative fixed charge states.

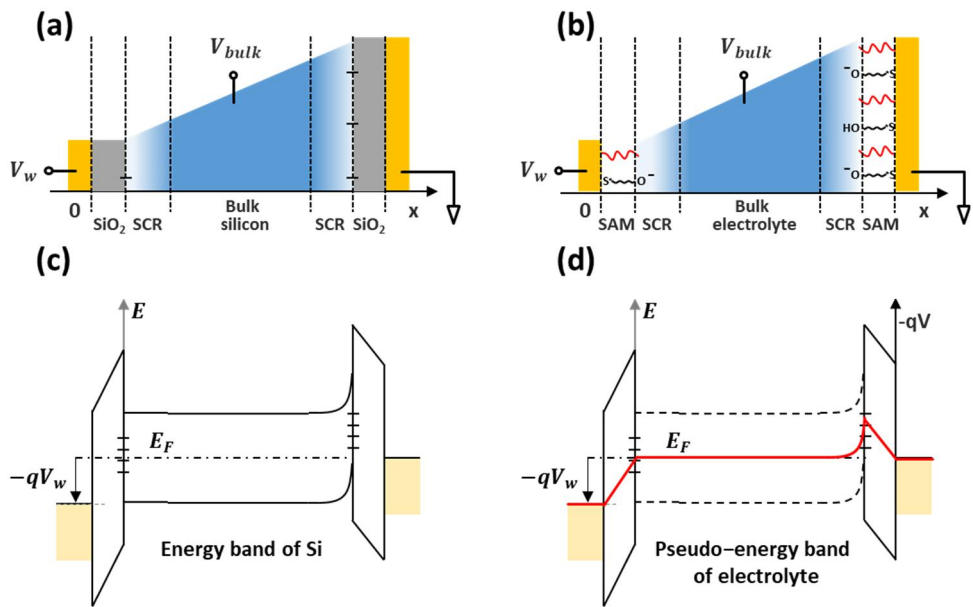


Figure 4-5. Energy band diagram and pseudo-energy band diagram of the MOSOS and MIEIM structure with negative fixed charge states under the flat-band voltage bias condition.

4.3. Flat-band voltage shifts and energy band diagram

To understand the electrostatic characteristics of the T-chip device without the electron tunneling, the C-V measurements were performed on the devices with different length of the pep-SAM layer. Four devices were prepared with different peptide SAM with n-Mercapto-1-Xols (MCX) series: (a) peptide only (b) peptide with 3-Mercapto-1-propanol (MCP) (c) peptide with 6-Mercapto-1-hexanol (MCH) (d) peptide with 9-Mercapto-1-nonanol (MCN). The thickness of the peptide SAM is determined by the carbon chain length of the back-filling material, MCXs, since without the back-filling materials the polypeptide chain does not have a fixed structural formation on the electrode surface after immobilization process. The schematic view of the four devices is illustrated in Fig. 4-6.

The measured C-V characteristics of the four devices are shown in Fig. 4-7. The flat-band voltage of the devices with the peptide only, the peptide with MCP, the peptide with MCH, and the peptide with MCN were -0.18 V, -0.09V, 0.0 V, and +0.16V, respectively. The flat-band voltage is positively shifted by increasing the thickness of the peptide-SAM. Under the assumptions that (a) the hydroxyl group at the end of the MCX-series acts as a negative surface charge of the peptide-SAM, (b) the surface charge densities, Q_i , of the four devices are the same, and (c) internal

charge, $\rho(x)$, in the peptide SAM (dielectric) is zero, the flat-band voltage, V_{FB} , can be expressed by following equations,

$$V_{FB} = \Phi_{MS} - \frac{Q_i}{C_{ox}} - \frac{1}{\epsilon_{ox}} \int_0^{t_{ox}} \rho(x) x dx, \quad (4.3.1a)$$

$$V_{FB} = \Phi_{MS} - \frac{Q_i}{C_{sam}} - \frac{1}{\epsilon_{sam}} \int_0^{t_{sam}} \rho(x) x dx. \quad (4.3.1b)$$

By increasing the thickness of the insulator layer (oxide and peptide SAM), the flat-band voltage shift is in the positive direction and proportional to the thickness of the insulator layer,

$$\Delta V_{FB} = -\frac{Q_i}{C_{ox}} = -\frac{Q_i}{\epsilon_{ox}} t_{ox}, \quad (4.3.2a)$$

$$V_{FB} = -\frac{Q_i}{C_{sam}} = -\frac{Q_i}{\epsilon_{sam}} t_{sam}. \quad (4.3.2b)$$

The energy diagram of the MCP, MCH, and MCN devices under the flat-band bias conditions are shown in Fig. 4-8. The energy band at the insulator-electrolyte surface is flat and there is no net charge and no electric field at the electrolyte side. In this condition, we can add the MB state (redox state) at the end of the peptide-SAM device. As shown in Fig. 4-9, the MB state acts as a donor-like trap state by capturing and releasing electrons according to the electric potential difference between the electrode and the electrolyte surface. The total charge of the MB state, Q_{MB} , due to the trapped electrons can be varied by the surface potential, ϕ_s , the MB state can be expressed as a capacitance, $C_{MB} = dQ_{MB}/d\phi_s$. This MB capacitance

is connected in parallel to the EDL capacitance and in serial to the peptide capacitance. It should be noted that the circuit configuration of the peptide SAM device is equivalent to that of the MOS device.

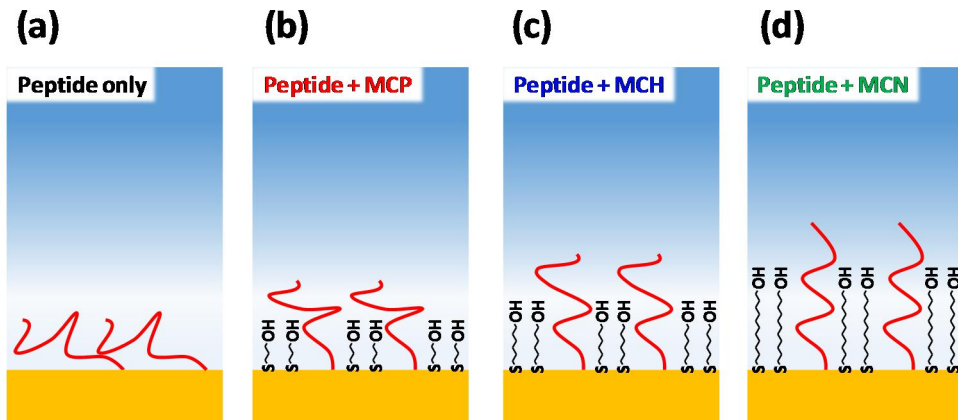
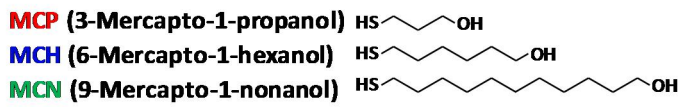


Figure 4-6. Schematics of the peptide only device, peptide with MCP, peptide with MCH, and peptide with MCN.

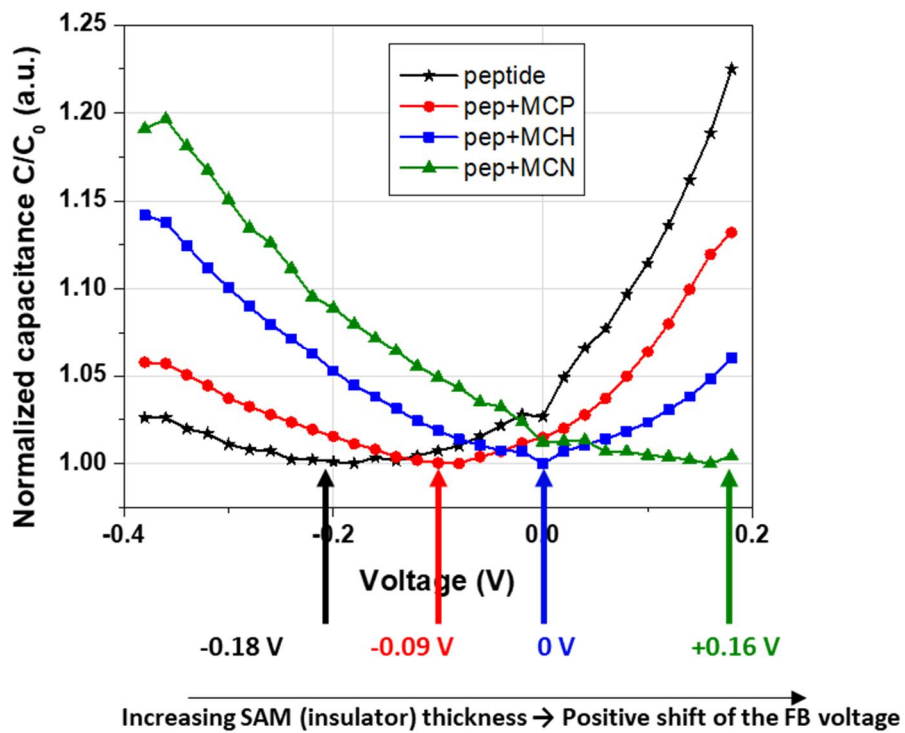


Figure 4-7. I-V characteristics of the devices for different SAM thickness.

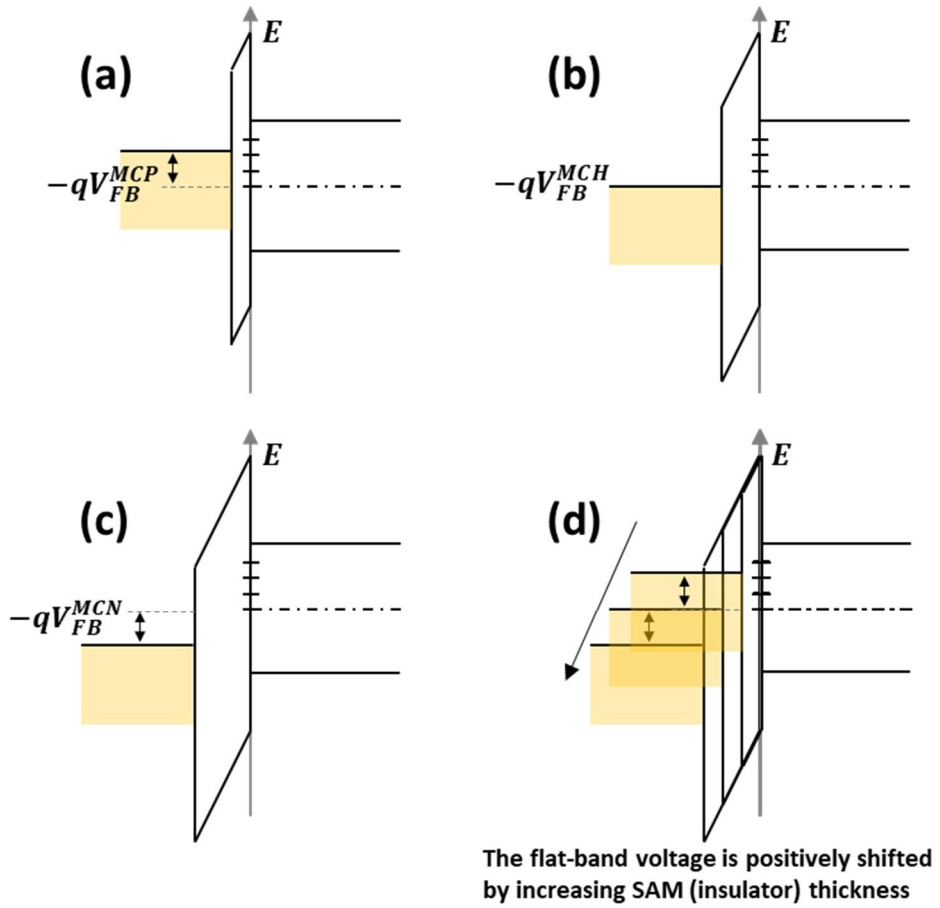


Figure 4-8. Energy band diagram of the devices with different thickness of the SAM under the flat-band voltage condition.

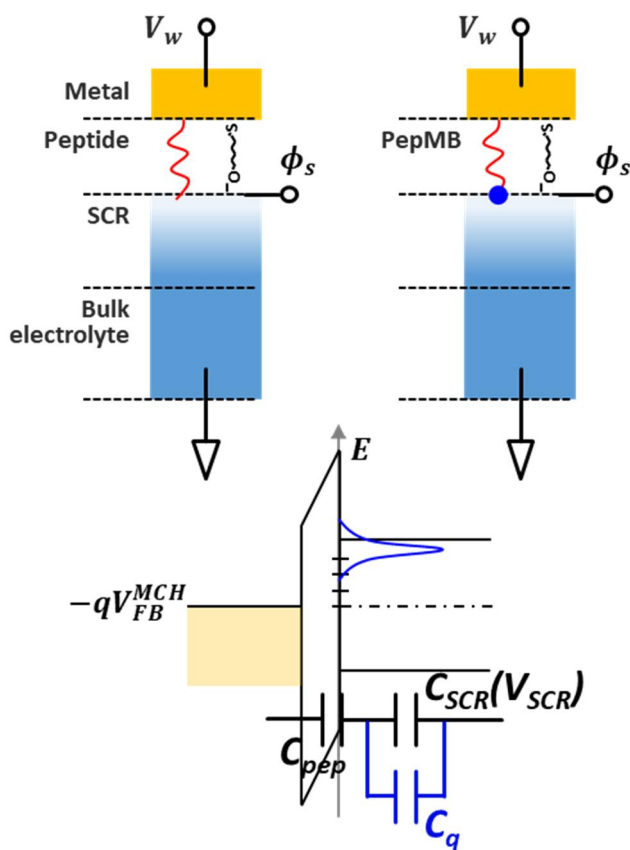


Figure 4-9. Energy diagram of the T-chip with the MB redox state. The MB redox state acts as the trap capacitance to capture and release the electron.

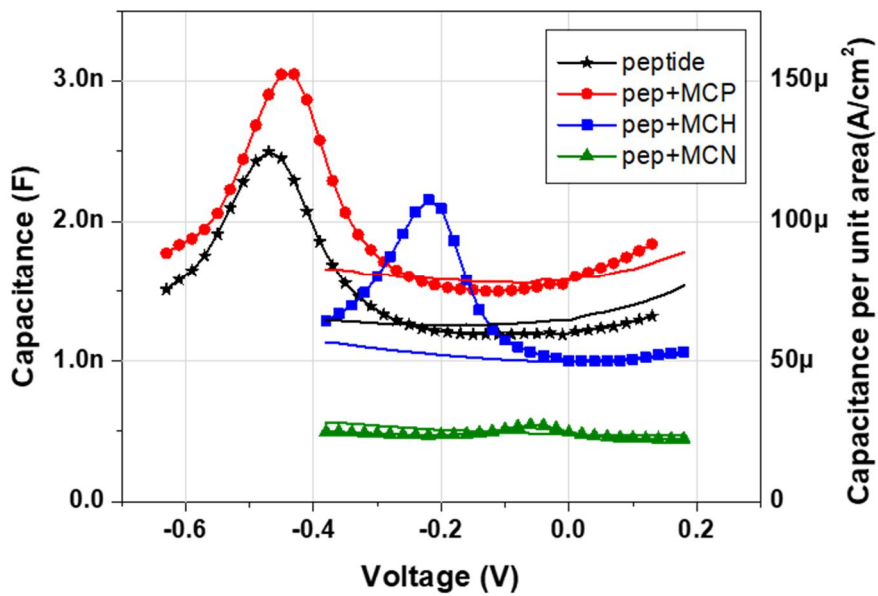


Figure 4-10. C-V characteristics of the T-chip devices having different modifications of the electrode surface.

4.4. Equivalent circuit model of T-chip

From the insight of the previous chapter dealing with the C-V characteristics of the peptide-SAM device, the following intuitive approach is possible. Since, basically MIE and MOS structure are the capacitors made of different layers between the electrode and electrolyte (semiconductor in this case of the MOS). Both devices can be represented by equivalent circuits with similar principle.

The charge components at the interface between the electrode and the electrolyte can be determined by the C-V characteristics of the MOS and MIE capacitors. First, we derive the capacitance-voltage relationships and describe the capacitance components and the equivalent circuit configuration with them. From the aforementioned energy band diagram of the MOS and MIE capacitors, the energy levels of the conduction band edges or the electrical potential in the neutral parts (bulk semiconductor and the bulk electrolyte solution) are taken as the zero reference potential. The surface potential, ϕ_s , is obtained from this reference level. The general formulation of the capacitance is defined as

$$C = \frac{dQ}{dV} \quad (4.4.1)$$

where the capacitance, C , is the change of total charge, Q , due to a change of voltage, V . Looking at the MOS and MIE capacitors from the working electrode,

the capacitance $C = dQ_w/dV_w$, where Q_w and V_w are the charge on the working electrode and the working electrode voltage respectively. First, since the total charge in the device must be zero, $Q_w = -(Q_s + Q_t)$, the voltage of the working electrode is partially dropped across the oxide (peptide-SAM) and semiconductor (electrolyte). This gives $V_w = V_{FB} + V_{ox} + \phi_s$, where V_{FB} is the flat-band voltage, V_{ox} is the oxide (peptide-SAM) voltage, and ϕ_s is the surface potential, allowing the previous equation to be rewritten as

$$C = -\frac{dQ_s + dQ_t}{dV_{ox} + d\phi_s}. \quad (4.4.2)$$

The semiconductor charge, Q_s , consists of hole charge density, Q_p , electron charge density, Q_n , bulk charge density, Q_b , with $Q_s = Q_p + Q_n + Q_b$ and the Eq. 4.4.2 becomes

$$C = -\frac{1}{\frac{dV_{ox}}{dQ_s + dQ_t} + \frac{d\phi_s}{dQ_p + dQ_n + dQ_b + dQ_t}}. \quad (4.4.3)$$

Utilizing the general capacitance definition of Eq. 4.4.1, Eq. 4.4.3 becomes

$$C = -\frac{1}{\frac{1}{C_{ox}} + \frac{1}{C_p + C_n + C_b + C_t}}. \quad (4.4.4)$$

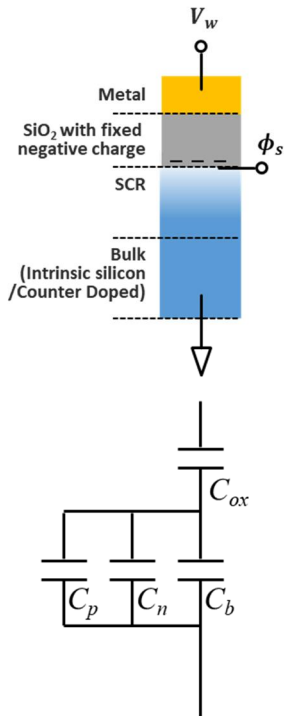
This derivation of the capacitance can be applied to the case of the MIE capacitor in the same way. The semiconductor charge, Q_s , which corresponds to the electrolyte charge, consists of total anions density, Q_{+ion} , and total cations, Q_{-ion} ,

which corresponds to Q_p and Q_n respectively. There is no fixed space charge in the electrolyte solution, so the no bulk charge density presents. In the same manner the electrolyte charge can be represented as $Q_S = Q_{+ion} + Q_{-ion}$ and capacitance formulation of the MIE capacitor becomes

$$C = - \frac{1}{\frac{1}{C_{pep}} + \frac{1}{C_{+ion} + C_{-ion} + C_t}} \quad (4.4.5)$$

The schematic illustration of the MOS and MIE capacitors and their equivalent circuits are shown in Fig. 4-11 and those with the components of the trap capacitance, where the trap charge is modulated by the surface potential, are shown in Fig. 4-12. The Stern and diffusion capacitances which exist between the peptide-SAM will be dealt with in the next chapter.

(a) Metal-Oxide-Semiconductor (MOS)



(b) Metal-Insulator-Electrolyte (MIE)

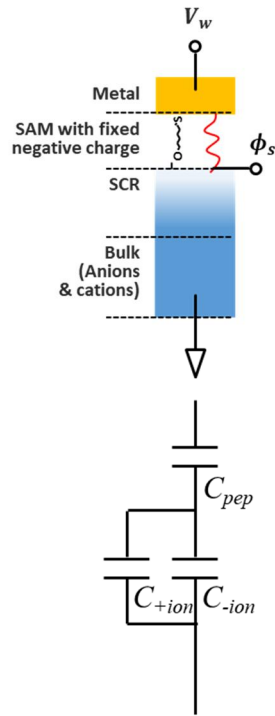
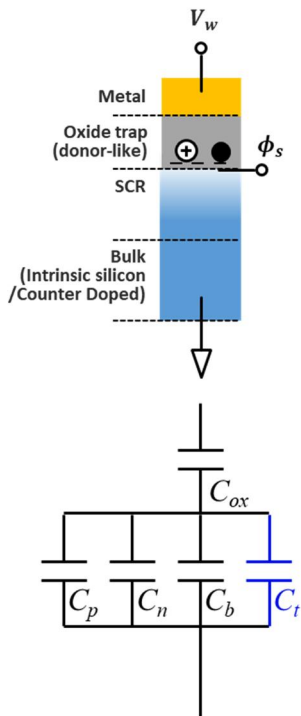


Figure 4-11. Equivalent circuit with the capacitive components of the (a) MOS and (MIE) capacitor.

(a) Metal-Oxide-Semiconductor (MOS)



(b) Metal-Insulator-Electrolyte (MIE)

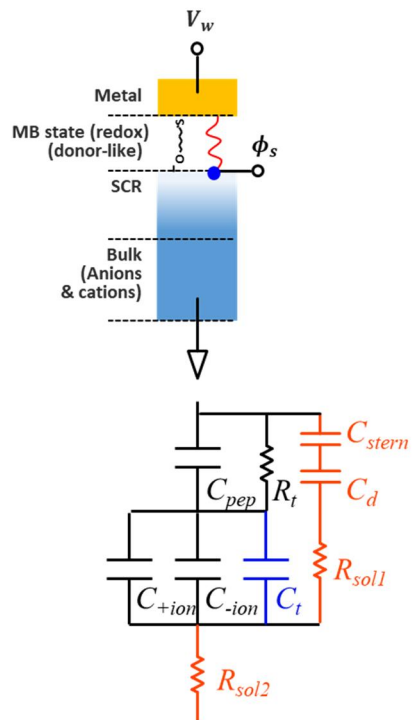


Figure 4-12. Equivalent circuit with the capacitive components of the (a) MOS and (MIE) capacitor with the trap capacitance.

4.5. Capacitive components of T-chip

From the previous chapter, the geometrical similarity between the MOS and MIE capacitors has been covered. Since the T-chip device, exactly the region nearby the working electrode at the interface between the peptide-SAM and the electrolyte, where most potential drop occurs can be considered as a capacitor, the flat-band voltage concept can be introduced to the C-V characteristics of the T-chip device. Individual capacitive components including C_{pep} , C_{+ion} , C_{-ion} , and C_t have been derived and the T-chip device has been represented by the equivalent circuit of these components. This chapter covers each capacitive component in more detail. The final equivalent circuit configuration of the bare, pep-SAM, and pep-MB-SAM devices and their C-V characteristics are schematically illustrated in Fig. 4-13.

In the case of the bare device, the C-V characteristic shows asymmetric and nonlinear characteristics. This is explained by the modified Gouy-Chapman theory, where the different hydrated radii of the anion and cation result in an EDL capacitance, C_{EDL} , to be asymmetric to the polarity of the electric potential of the working electrode [31]. The thickness of the stern layer of EDL becomes asymmetric according to the distance of closest approach of the anions and cations. The total capacitance of the bare device can be described as

$C_{EDL} = C_{st}(V_{st}) || C_{DL}(V_{DL})$, where C_{st} and C_{DL} are the stern and diffusion capacitance and are the function of the voltage across the stern layer, V_{st} and the diffusion layer, V_{DL} respectively.

$$C_{total}^{Bare} = C_{EDL} = C_{st} || C_{DL} \quad (4.5.1)$$

The capacitance of the stern layer is represented as by the following equations.

$$C_{st} = \frac{\epsilon_0 \epsilon_w}{t_{st}(V_{st})} \quad (4.5.2)$$

where ϵ_0 and ϵ_w are the dielectric constant of and water molecule respectively and t_{st} is the thickness of the stern layer and function of the polarity of the voltage across the stern layer V_{st} . The capacitance of the diffusion layer due to the transport of charge carriers is the derived from Poisson-Boltzmann equation as,

$$C_{DL} = C_0 \cosh\left(\frac{V_{dl}}{2k_B T \eta}\right) \quad (4.5.3)$$

where k_B is the Boltzmann constant, T is temperature, and η is the fitting factor for experimental data having different value according to the polarity of V_{st} . V_{dl} is the voltage across the diffusion layer and the C_0 is the capacitance when the surface charge density equals to the bulk charge density given as

$$C_0 = \sqrt{\frac{2z^2 q^2 \epsilon_0 \epsilon_w n_0}{k_B T}} \quad (4.5.4)$$

where z is the charge magnitude of each ion, q is the electric charge, and n_0 is the bulk ion concentration.

Since the measured capacitance value includes unknown factors in the real interface which cannot be expressed by the equivalent circuit, we introduced the fitting factor, η in an appropriate manner. In Fig. 4-14, the black line is the experimental data of the C-V characteristic of the bare device. Among the fitted curves shown with the red, yellow, and blue lines, the blue one is chosen as the best case with the fitting factor of 3 and 1.5 for the positive and the negative voltage region, respectively. The thickness of the Stern layer is chosen as 0.25 nm and 0.2 nm for the anion and cation respectively.

Now consider the peptide-SAM device after immobilizing the peptide layer on the bare electrode. The total capacitance value can be expressed as following,

$$C_{total}^{pep} = \gamma(C_{pep} || C_{SCR}) + (1 - \gamma)C_{total}^{Bare}. \quad (4.5.5)$$

Since the peptide-SAM is not a perfect layer, there is a crack and gap between each peptide chain and each back-filling materials. Therefore, the total capacitance of the peptide-SAM device can be expressed as a parallel sum of the peptide capacitance, C_{pep} , and the partial EDL capacitance obtained from the capacitance value of the bare device. The capacitance of the space charge region (SCR), C_{SCR} , is the same with C_{total}^{Bare} . Here surface covering factor of the peptide-SAM, γ , is introduced to reflect the incomplete coverage of the electrode layer and the value of 0.8 is chosen as the best case.

Finally, by connecting the MB capacitance (redox or quantum capacitance), C_q , with the SCR capacitance in parallel, the total capacitance expression of the T-chip device is completed as the following equation,

$$C_{total}^{pepMB} = \gamma(C_{pep} || (C_{SCR} + C_q)) + (1 - \gamma)C_{total}^{Bare}. \quad (4.5.6)$$

Here the chemical capacitance [32], [33], (redox capacitance, electrochemical capacitance, or quantum capacitance) of the MB state is expressed as, C_q . By the definition of the capacitance,

$$C_q = \frac{dQ}{dV_{C_q}} \quad (4.5.7)$$

where V_{C_q} is the voltage across the C_q same as the surface potential, ϕ_s , considering the electrical potential of bulk electrolyte solution as the reference potential of zero. The charge of the MB state, Q , is simply $-qnf$, determined by the product of the elementary charge, q , the total density of state of MB, n , and the Fermi-Dirac distribution function, f , as following,

$$f(E - E_{F_n}) = 1 / (1 + \exp[(E - E_{F_n})/k_B T]) \quad (4.5.8)$$

where k_B is Boltzmann's constant and E_{F_n} is the Fermi level. The electrochemical potential of electrons, $\bar{\mu}_n$, (Fermi level, E_F) at the side of the MB state is varied by the change of the surface potential, $d\phi_s = -d\bar{\mu}_n/q$. The change of the chemical potential of electrons, μ_n , in the MB states is associated by the variation of the filled density of state of MB, dnf , of which average occupancy is determined by the Fermi-Dirac distribution function. The change of the surface potential varies the

distribution as expressed,

$$\frac{df}{dE_F} = \frac{1}{k_B T} f(1 - f). \quad (4.5.9)$$

By combining the previous equations, the chemical capacitance of the MB states in Eq. 4.5.7 becomes as following,

$$\begin{aligned} C_q &= q^2 \frac{dnf}{d\phi_s} \\ &= \frac{q^2 n}{k_B T} f(1 - f). \end{aligned} \quad (4.5.10)$$

The derived capacitance components and the equivalent circuit diagram can describe the C-V characteristics of the T-chip devices with the electrodes for the various surface modifications and its parameters can be estimated by fitting to the experimental data. Though this configuration may not perfectly reflect the situations on the electrode surface with complex electrochemical and physical phenomena, for all the bias conditions and environmental conditions, the simplified equivalent circuit expression based on the perspective of the MIE capacitor structure can give us the intuitive insight for the T-chip device and the fundamental meaning of its physical behavior.

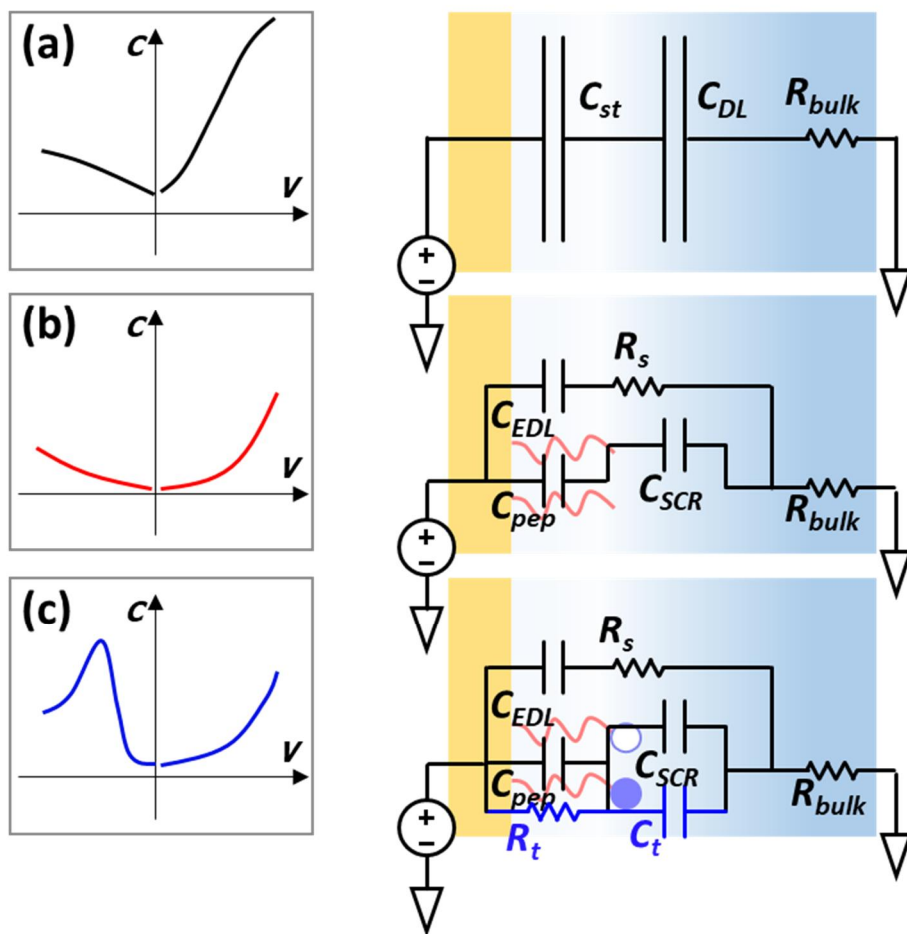


Figure 4-13. The schematic illustration of the I-V characteristics of the bare, peptide (pep-SAM), and peptide-MB-SAM (pep-MB-SAM) devices and their structures.

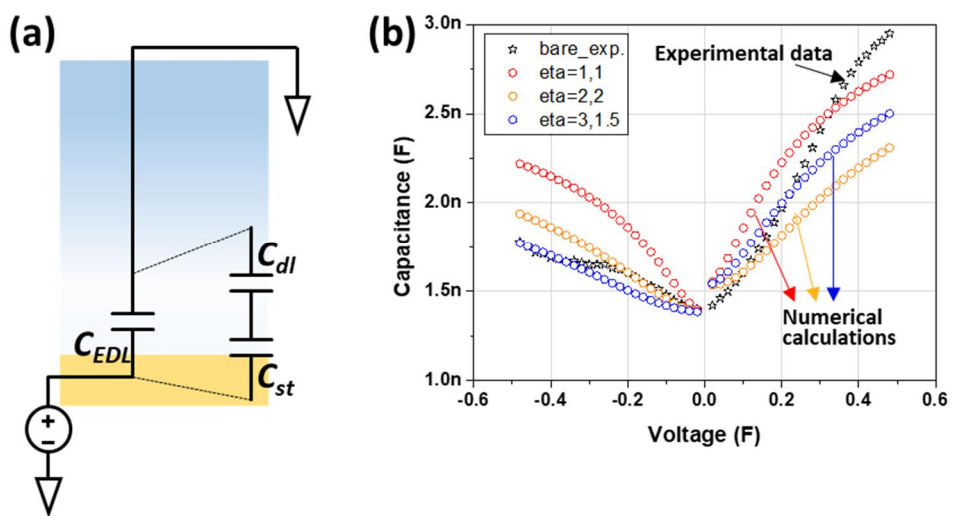


Figure 4-14. (a) Schematic illustration of the bare device. (b) C-V profiles of the bare device and its fitted numerical calculations.

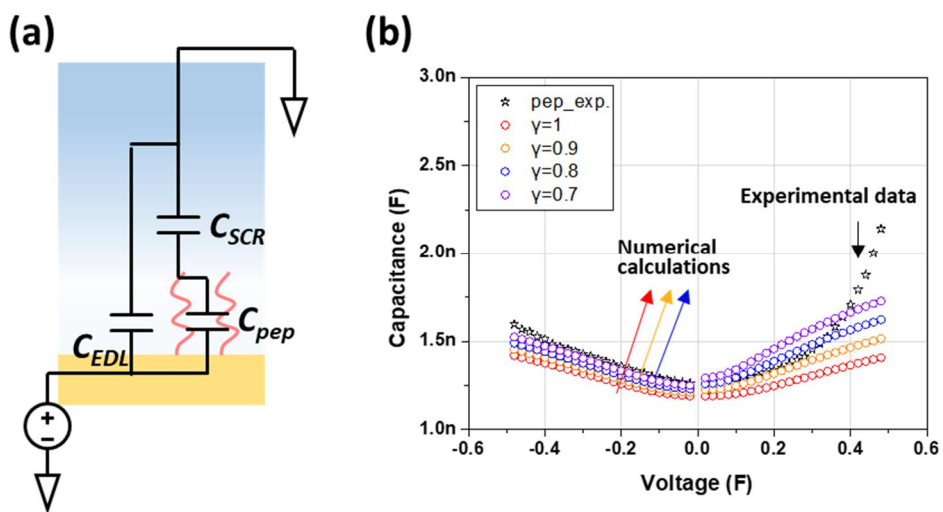


Figure 4-15. (a) Schematic illustration of the peptide-SAM device. (b) C-V profiles of the peptide-SAM device and its fitted numerical calculations.

Chapter 5.

Voltage pulse method

5.1. Motivation

The redox-active self-assembled monolayer (redox-SAM) [34]–[36] and its biosensor application have attracted much attention in the field of electrochemistry for decades [37]–[40]. To understand its versatile and unique electrical characteristics, various electrochemical measurement methods based on cyclic voltammetry (Cyc-V) have been developed. The key concept of these methods is to force a voltage signal and measure the current response, which includes both capacitive current and tunneling current (i.e., the faradaic current or the reduction/oxidation of redox molecules). By doing so, the change in the redox-SAM after interaction with the target biomolecules in the electrolyte is detected as the sensing signal.

The following two components are used to evaluate the state of the redox-SAM:

capacitive current and tunneling current (see Fig. 5-1). The capacitive current is determined by the capacitance components at the electrical double layer (EDL) and space charge region (SCR), which are formed between the electrolyte and the bare electrode uncovered by the SAM and between the SAM and the electrolyte, respectively. Both capacitance components are a function of the charge density of mobile ions distributed by the electrical potential profile along the electrolyte. The tunneling component is determined by the electron transfer rate between electrons in the metal and redox states at the SAM. The electron transfer rate is a function of electrical potential through the SAM and the density of states (DOS) of the redox molecules. We mainly aim to accurately extract electron tunneling current from the total current, which includes the capacitive component in transient time. To be noticed is that the tunneling current is the signal indicating the number of redox states introduced as the MB states as described in the previous chapter. The tunneling current is maximized in the early transient phase of the pulse when the electric field in the SAM is strong and several redox molecules are yet to be reacted.

A difficulty arises because the tunneling current (the signal) is much smaller than that of the capacitive current. For this reason, several measurement techniques have been developed to exclude the capacitive current. In Cyc-V with the staircase and the square-wave voltage signals, as shown in Fig. 5-2(a) and (b), the tunneling current for each voltage step (<50 mV) is measured after the decay of the capacitive current, and hence, these methods have become the most widely used technique in

electrochemistry. [41], [42] However, they only use a single-point value of the tunneling current at the end of the voltage steps, so considerable information in the tunneling current, especially in the early state of the pulse, is missed. Additionally, the low amplitude of the voltage steps (small signal) and delay time for the decay of the capacitive current require long measurement time.

We propose a new approach for using the entire transient characteristic of the tunneling current, instead of the single-point value, at a special time when the capacitive current is expected to diminish. A schematic of this method is shown in Fig. 5-2(c), which comprises large-signal voltage pulses (~ 500 mV) with positive and negative signs. Once the pulses are applied to the working electrode, the current is measured from the counter electrode using the conventional operational-amplifier (OP-amp) with a low-pass filter and an oscilloscope (Fig. 5-3). Under the positive pulse, only the capacitive charging current flows without the tunneling event, while a combination of the tunneling and capacitive current flows under the negative pulse (the dependence of the electron tunneling current on the polarity of the pulses will be dealt with in the discussion session). If the capacitive current components are same for both positive and negative polarities of the pulse potential, the tunneling current can be extracted from the current response of the negative pulse for the entire transient time.

We will show experimentally that this method not only provides much more

information about the redox molecules on the electrode but also enhances the signal intensity. By applying the method to the T-chip platform [26] as an example, we will show that the method increases the sensor performance in terms of sensitivity and selectivity. We believe that this method can be a powerful tool for characterizing a redox-SAM device and applying a protease-based biosensor using the SAM as the probe molecule.

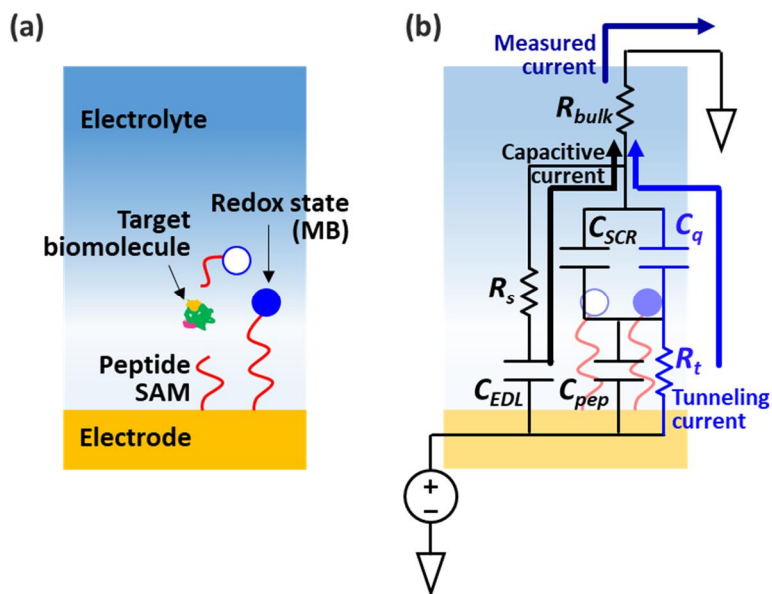


Figure 5-1. (a) T-chip platform. The peptide SAM is immobilized on the electrode by adopting Au-thiol bonding. The end of the peptide is modified with methylene blue (MB) as a redox state acting as a donor-like trap where the tunneling event occurs. (b) The equivalent circuit. The large capacitance component at the EDL and SCR: the EDL component is formed between the electrolyte and the bare electrode uncovered by the SAM, while the SCR component is formed between the SAM and the electrolyte. The MB state and its tunneling rate can be equivalently described as C_q and R_t , respectively.

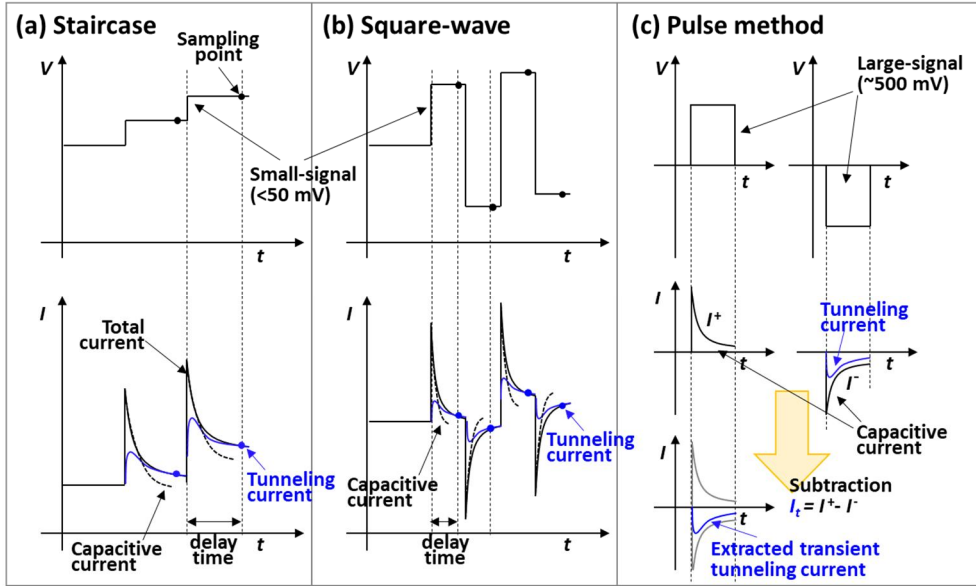


Figure 5-2. Electrical potential (small signal < 50 mV) and its corresponding current responses for (a) the staircase and (b) square-wave Cyc-V. Both measurement methods take only a single point of the tunneling current, which appears after decaying of the capacitive current with delay time. (c) Transient tunneling current can be extracted by eliminating the capacitive current in the suggested pulse method. The electrical potential (large signal ~ 500 mV) is applied to maximize the amplitude of the tunneling current.

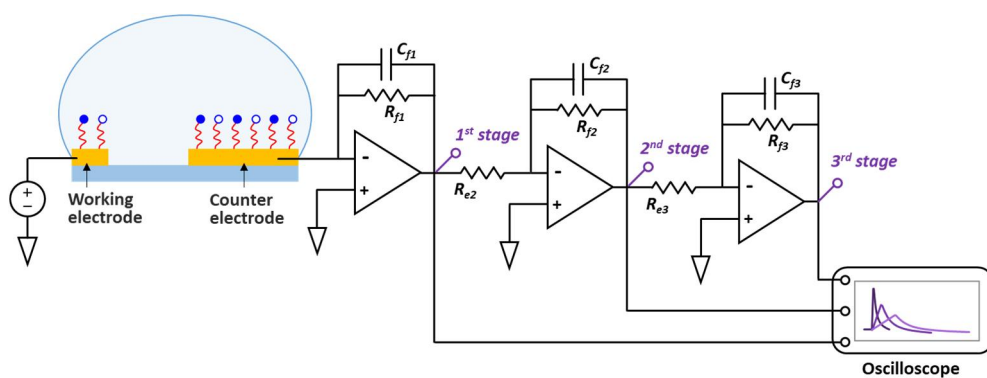


Figure 5-3. Measurement system with device connection. The electrical potential of the electrolyte is stabilized by the virtual ground of the op-amp. The current response of the input voltage pulse is converted into the voltage signal and captured by a digital oscilloscope.

5.2. Preparation of sensor device and electrical measurement

As reported in the reference [22], [26], the concentric electrode structure of a sensor device stabilizes the electrical potential of the electrolyte. Because of the larger area of the counter electrode as compared to that of the working electrode, the electrical potential of the bulk electrolyte is stabilized following the voltage of the counter electrode, through the “*self-gating effect*.” [20], [21] The structure of the device and its potential profile are illustrated in Fig. 5-4.

The peptide sequence which is given as Gly-Pro-Leu-Gly-Met-Trp- Ser-Arg-Cys; GPLGMWSRC was selected as the SAM and its end terminal was modified with methylene blue (MB) as the redox molecule [19], [22], [26]. The immobilization process of the peptide SAM is described hereafter. The bare device with the gold electrodes was cleaned by sonicating in acetone for 10 minutes. After the sonication, the device was washed thoroughly with isopropanol, ethanol and DI water for 5 minutes respectively, and then dried with a stream of nitrogen. The cleaned gold electrodes were incubated in 1 M of MB-peptide diluted solution with dimethyl sulfoxide (DMSO) at room temperature for 2 hours. After washed with DI water for 30 s and dried with the stream of nitrogen, the electrodes were incubated in 1 mM of 6-mercapto-1-hexanol (MCH) diluted solution with Dulbecco’s phosphate-

buffered saline (DPBS) for 1 hour. Finally, the electrodes were washed with DI water and dried again. A polydimethylsiloxane (PDMS) well was mounted on the device surface to prevent the solution from flowing over the surface of the device and to provide the micro-chamber for biochemical reactions. We injected 10 μ L of DPBS droplet into the PDMS well, and thereby on the device, to initialize the device.

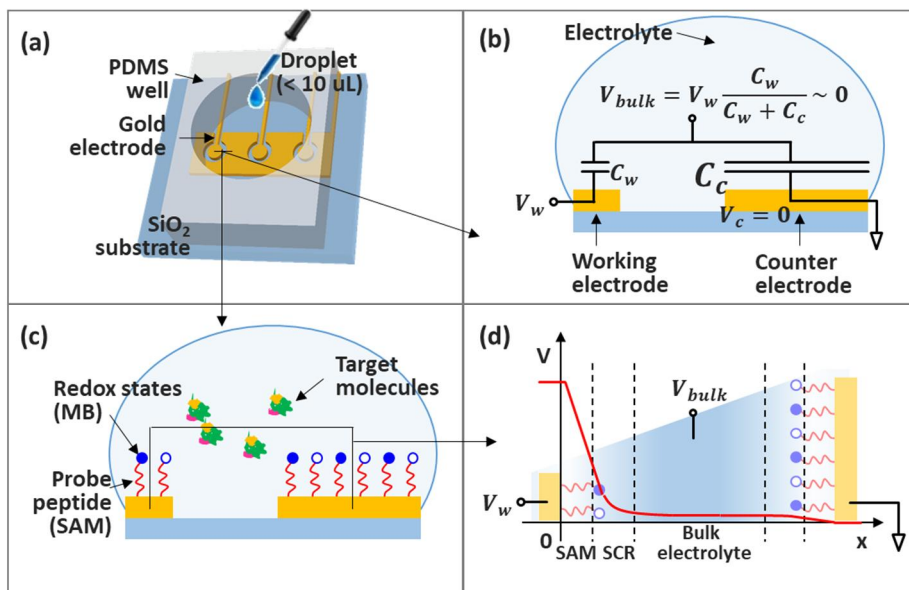


Figure 5-4. (a) Reference electrode-free device (T-chip) and its concentric electrode structure. (b) Due to the area asymmetry of the electrodes, the electrical potential of the bulk electrolyte is stabilized by capacitive coupling, called “*self-gating effect*.” (c) MB-modified peptide SAM is immobilized on the gold electrode. (d) Potential profile from the working electrode to the counter electrode. Most of the potential drop occurs through the SAM and SCR.

5.3. Extraction of transient tunneling current

To confirm the validity of the method experimentally, two devices were prepared: one without MB (pep-SAM), as a control, and the other with MB (pep-MB-SAM), as the redox molecule. The schematics of the devices are shown in Fig. 5-5 and their equivalent circuits (each component will be detailed in the next section) are overlaid on them. The difference between both devices is the existence of the MB state. The tunneling phenomenon between the metal electrode and the MB state in the SAM can only occur for the pep-MB-SAM device (Fig. 5-5(c)) under the negative pulse. However, the intensity of the capacitive current is much larger than that of the tunneling current during the transient time. In this section, we show that the tunneling current can be extracted by eliminating the capacitive current using the pulse method.

As briefly aforementioned in Fig. 5-2(c), the basic procedure of the pulse method is as follows: (1) Apply pairs of positive (V^+) and negative (V^-) potential steps with the same amplitude. (2) Capture the corresponding current (I^+ and I^-) responses. (3) Extract the tunneling current by subtracting the captured current ($I^+ - I^-$) at the positive pulse from that at the negative pulse. The amplitude of the input voltage pulse was varied from 0.05 to 0.5 V in 0.05 V steps. The current

responses showing the R-C charging characteristic are plotted in Fig. 5-5(b) and (d) (see the black lines). By subtracting both positive (I^+) and negative (I^-) currents, we obtained the differences of the currents. Note that negligible difference was observed from the pep-SAM device (red lines in Fig. 5-5(b)). On the other hand, in the case of the pep-MB-SAM device, an appreciable amount of tunneling current (denoted by the blue lines) was observed and increased with the pulse amplitude.

Since a small mismatch in the capacitive currents can cause a large error in the extracted tunneling current, we must check how equal the magnitudes of the capacitive current components in the positive and negative pulses are. The difference in currents in the case of the pep-SAM device (red line) is smaller than 2.5% of the total capacitive current, which indicates that the capacitive component of the pep-SAM device shows characteristics that are quite symmetric to the polarity of the input voltage pulse. Additional control samples, the bare device and partially modified-MB-SAM device (immobilization time for the peptide-SAM and MCH were 2 minutes and 1 minute respectively.) were prepared. Their experimental results were shown in Figs. 5-6 and 5-7 to show that the pulse method would not work for the device system with asymmetric capacitive components. (The discussion on the capacitive and electron tunneling components are dealt with in the C-V characteristics shown in Fig. 5-8.)

To support the results of the pulse method showing the symmetry of the

capacitive current in the pulses of opposite polarity, we show the quasi-static capacitance-voltage ($QSCV$) measurement (by using HP-4156C) results for four samples in Fig. 5-8: bare (purple line), pep-SAM (red line), pep-MB-SAM (blue line), and the partially modified-MB-SAM (green line). However, a major concern here is the nonlinear and particularly asymmetric capacitance-voltage ($C-V$) characteristics of the device with the electrolyte solution (purple line). This is explained by the modified Gouy-Chapman theory, where the different hydrated radii of the anion and cation result in an EDL capacitance, C_{EDL} , asymmetric to the polarity of the electrode potential. The strategy of the pulse method is based on the reduction of the portion of the asymmetric and nonlinear capacitance from the total capacitance of the device.

After introducing the pep-SAM to the gold electrode, the peptide layer occupies a major area of the electrode surface and pushes away the water molecules and ions in the electrolyte solution. The area of EDL between the electrode and the electrolyte reduces, and therefore, the asymmetric $C-V$ characteristics are moderated (red line). In addition, due to the existence of peptide capacitance, C_{pep} , which is serially connected with SCR capacitance, C_{SCR} , the potential drop across the SCR layer, V_{SCR} , for the input potential is capacitively divided by C_{pep} and C_{SCR} , so the nonlinear $C_{SCR}(V_{SCR})$ does not increase dramatically. Therefore, in the case of the pep-SAM device, the capacitive currents in the pulse method can be eliminated with negligible error.

In the case of the pep-MB-SAM device (blue line), there exists an additional current component of electron tunneling between the electrode and redox MB states for the negative-bias region. The MB state can be considered as a trap state (donor-like) that is similar to the interface states in MOS devices. This is demonstrated by introducing the redox capacitance, C_q , and tunneling resistance, R_t (see blue circuit components in Fig. 5-5(c)). By observing that the position of the peak shape of $C-V$, the standard redox energy level of MB, where the numbers of unfilled and filled states of MB are equal, is higher than the Fermi level of the gold electrode, which causes the polarity dependence of the tunneling current. At the zero bias in equilibrium, most MB states are empty, so only the negative pulse can supply the tunneling current filling the unoccupied MB states, while the positive pulse cannot.

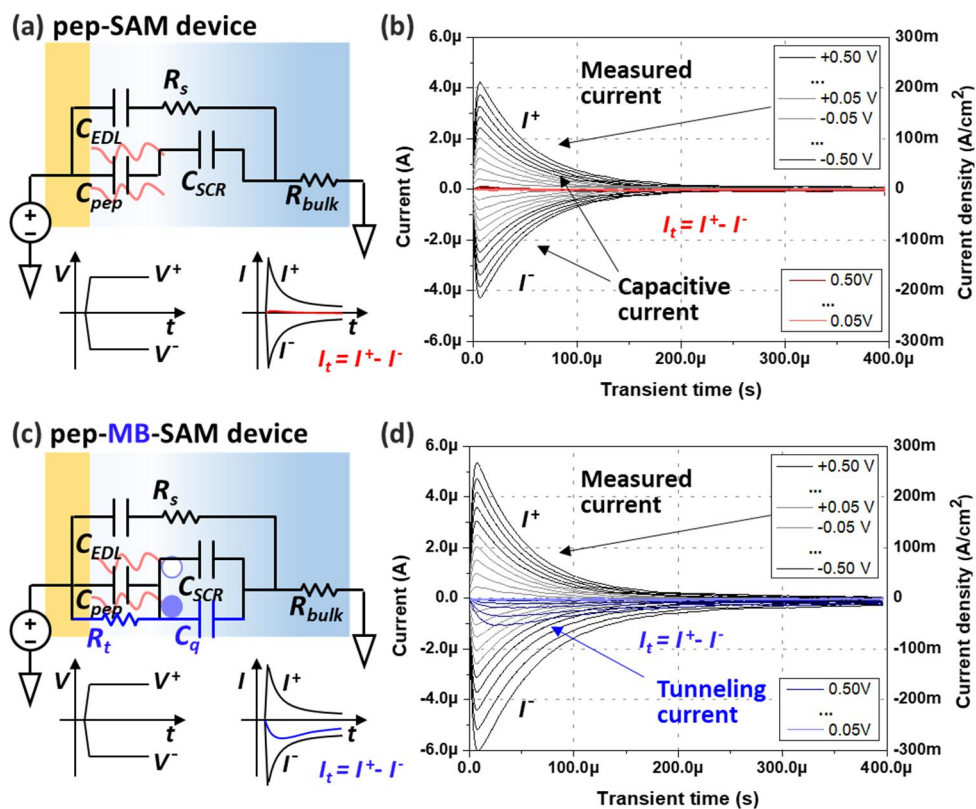


Figure 5-5. Schematics of the devices functionalized by the SAM with MB (pep-MB-SAM) and without MB (pep-SAM) and their equivalent circuits. (a, c) Measured current responses and their differences. (b, d) Plotted current responses are captured from the 2nd stage of the circuit shown in Fig. 5-3. The transient tunneling current (blue in (d)) is extracted in the case of pep-MB-SAM, while no appreciable tunneling current (red in (b)) is observed in the case of pep-SAM.

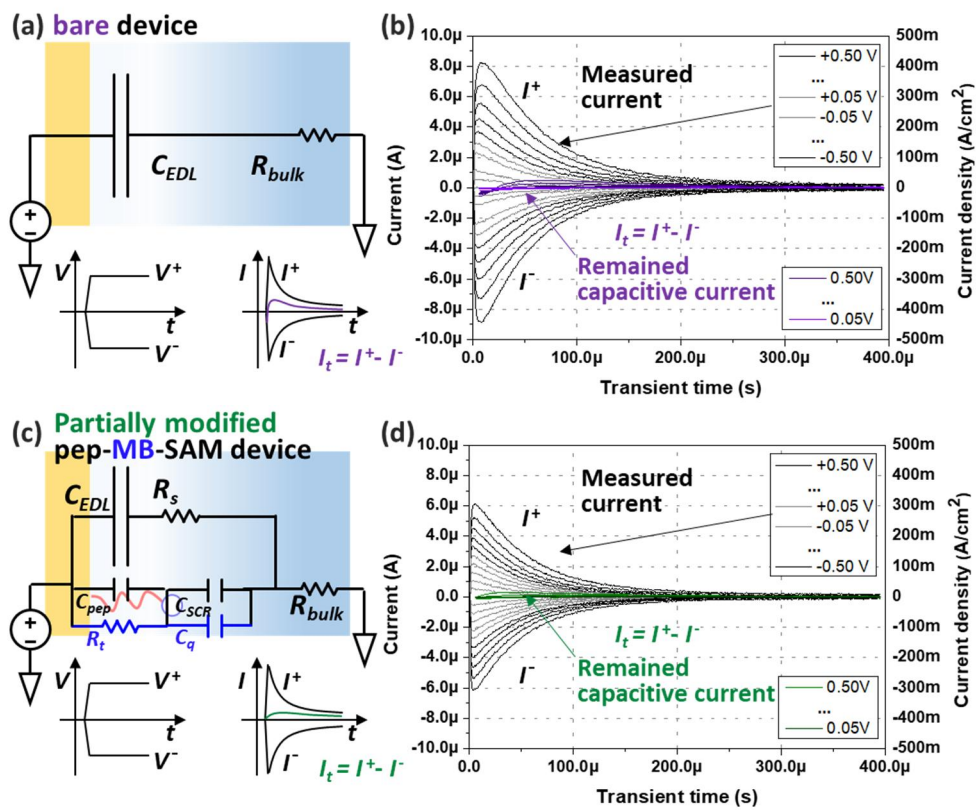


Figure 5-6. Additional control experiments. The bare device (a) and the partially modified pep-MB-SAM device (c). Measured current responses and their differences (b, d). The capacitive currents are not fully eliminated in both cases.

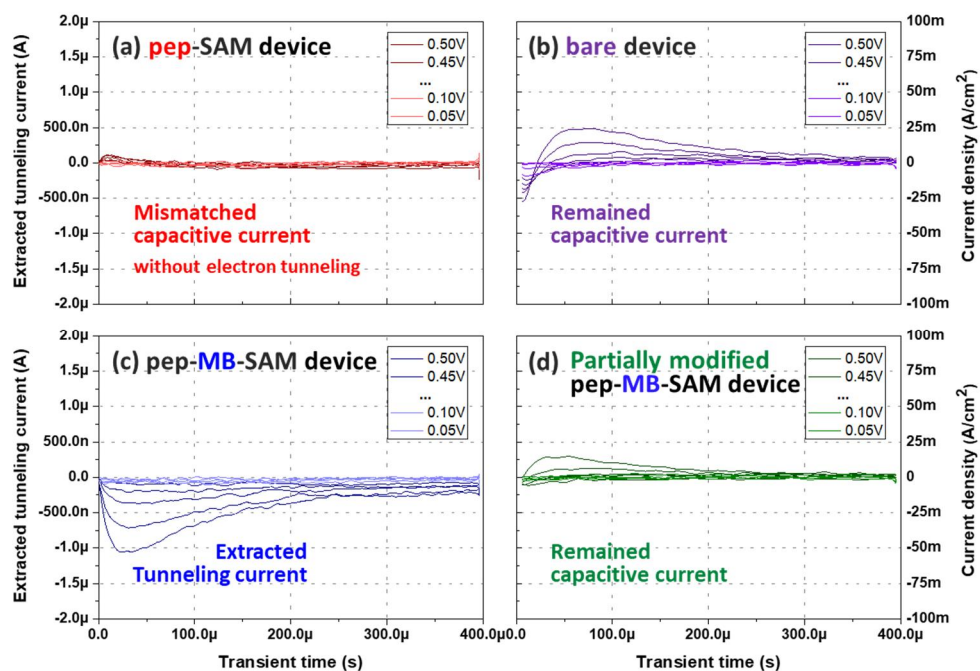


Figure 5-7. Transient current characteristics after subtracting the capacitive current components (The plots from Figs. 5-5 and 6 are reorganized). The pep-SAM device without electron tunneling (a, red) and the pep-MB-SAM device with electron tunneling (c, blue). Additional control samples: the bare device (b, purple) and the partially modified pep-MB-SAM device (d, green).

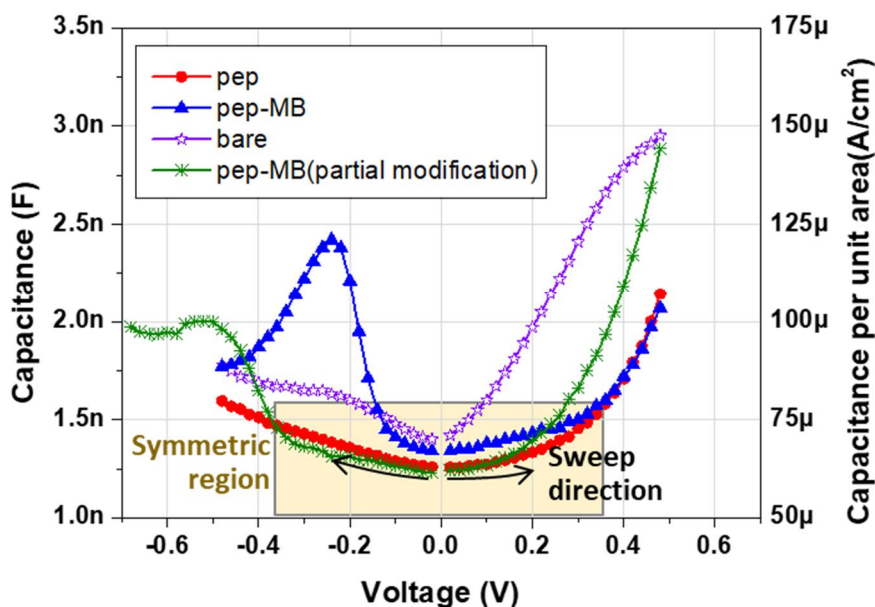


Figure 5-8. C-V characteristics of the various devices under different surface conditions. The potential of the working electrode is swept from 0 to -0.5 V and +0.5 V, while the counter electrode is grounded. The bare electrode shows either a nonlinear or an asymmetric profile (purple). After introducing the peptide SAM on the metal electrode, the capacitance becomes quite symmetric (red). The existence of MB states is observed in the negative-bias region (blue). The MB state can be considered as the trap state (donor-like), which is similar to the interface trap or the oxide trap of the solid-state devices. It can be described as capacitance, C_q , in Figs. 5-1 and 5. By utilizing this symmetrized capacitance (red), the capacitive current can be eliminated and the tunneling current can be extracted in the pulse method. This indicates that the pulse method would not work for the partially modified pep-MB-SAM device (green) with the asymmetric capacitive characteristic.

5.4. Verification of voltage pulse method

5.4.1. Practical problem: voltage and time windows

The current components measured in the T-chip device are the capacitive currents and the tunneling current, which are the transient current. Notice that the tunneling current also transient as the current diminishes when the MB states are all filled or unfilled with the tunneled electrons and there is no steady-state current. Hence, the measured transient current is expected to drastically decrease after applying the voltage step by using the voltage pulse method. Due to the exponential decay rate of the transient current characteristics, a practical difficulty arises to measure accurately the current in transient time.

The major problem is the voltage and time resolution limit of the measurement equipment. In this research, the oscilloscope with 10-bit voltage resolution was used to capture the transient current characteristics of the T-chip device. Therefore it is important to set appropriate voltage and time windows for the measurement. Here, in the measurement system, two devices are connected and its transient characteristics are measured in parallel. The measurement system consists of the three stages including the amplification stages and the 1st order low pass filter stages which covert the current signals to voltage signals. At the end of each stages

the voltage signals are captured by the oscilloscopes. The cut-off frequencies of the low-pass filters at each stages are 1 MHz, 100 kHz, and 2 kHz, respectively. The voltage resolutions of the oscilloscopes were 50 mV, 20 mV, and 200 mV and the time resolution of those were 400 ns, 8 μ s, and 1 ms respectively.

In Fig. 5-12 the transient current characteristics of the total current, current of the T-chip device, the current difference of the pep-SAM device, and the extracted tunneling current of the pep-MB-SAM device were plotted in the linear, the semi logarithmic x (semi-log-x), the semi logarithmic y (semi-log-y), and the logarithmic-logarithmic (log-log) plots. In the log-log plot, the current levels of total current of the T-chip device, current difference of the pep-SAM device, and the tunneling current of the pep-MB-SAM device is continuous in each stage.

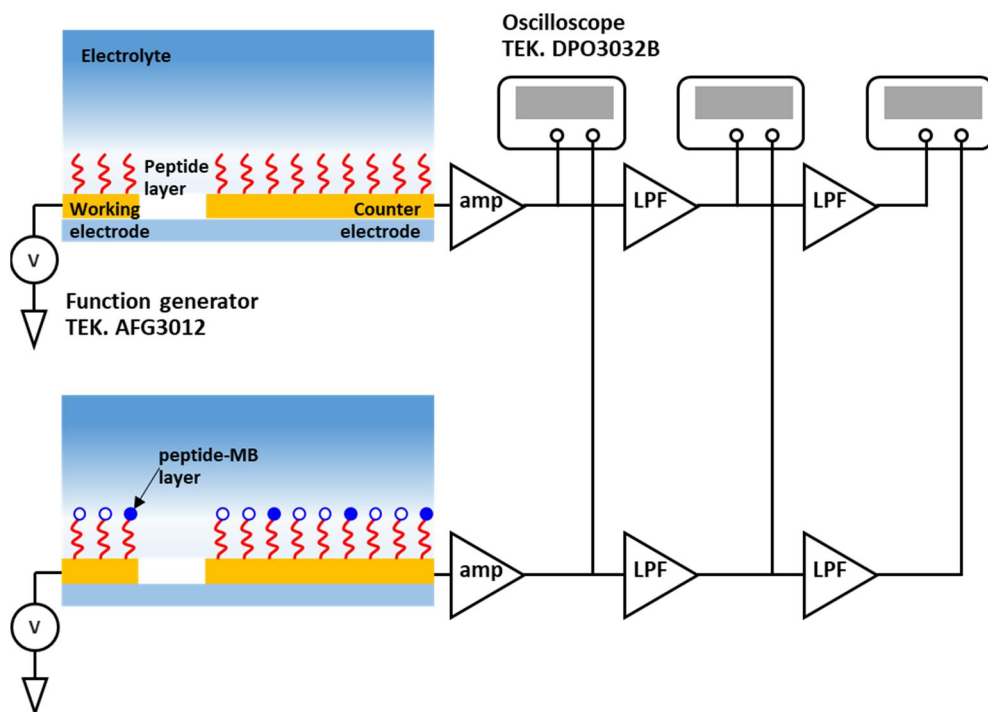
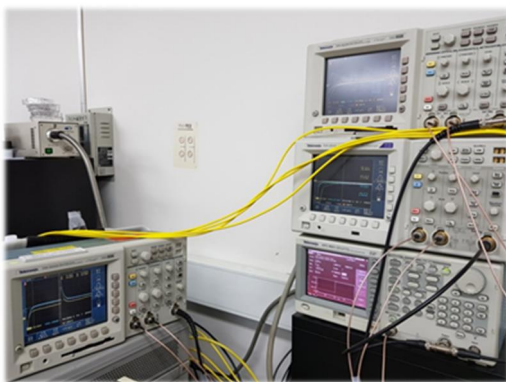
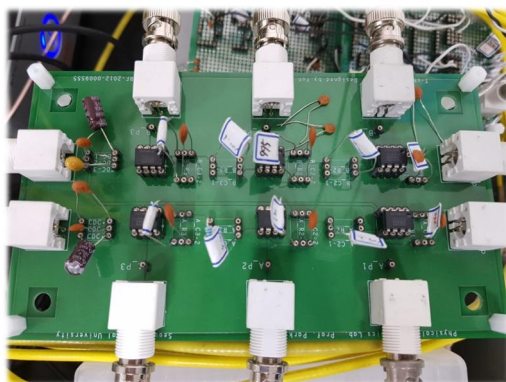


Figure 5-9. Measurement configuration. Two devices are connected and its transient characteristics are measured in parallel. The measurement system consists of the three stages including the amplification stages and the 1st order low pass filter stages which convert the current signals to voltage signals. At the end of each stage the voltage signals are captured by oscilloscopes.



(a)



(b)

Figure 5-10. (a) Three oscilloscopes for the three stages of the measurement system and the function generator. (b) PCB board of the measurement system.

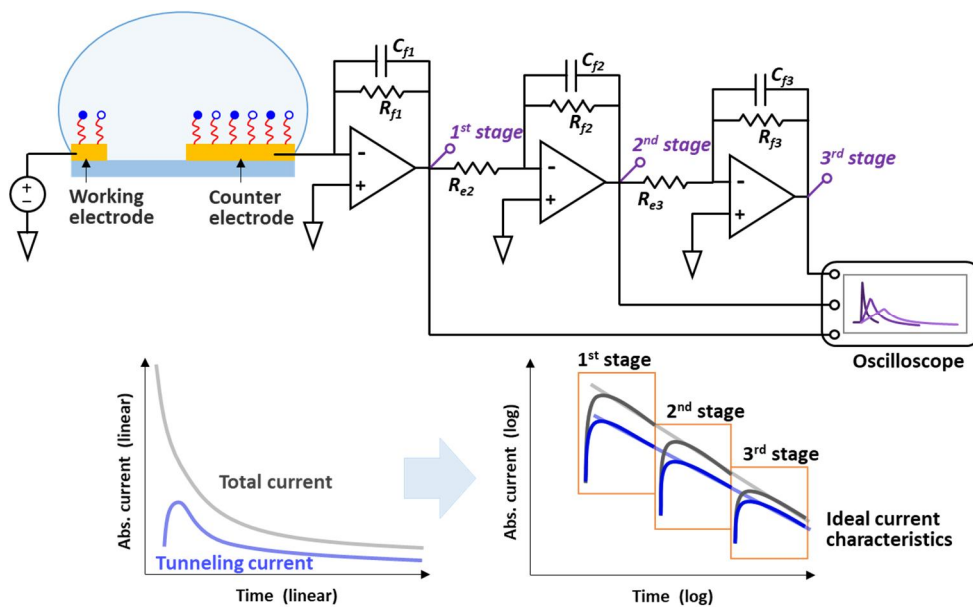


Figure 5-11. Schematic plot of the transient current characteristics of the total current (gray) and the tunneling current (blue). The drastic decreases of the current characteristics in transient time are plotted in the log-log plot.

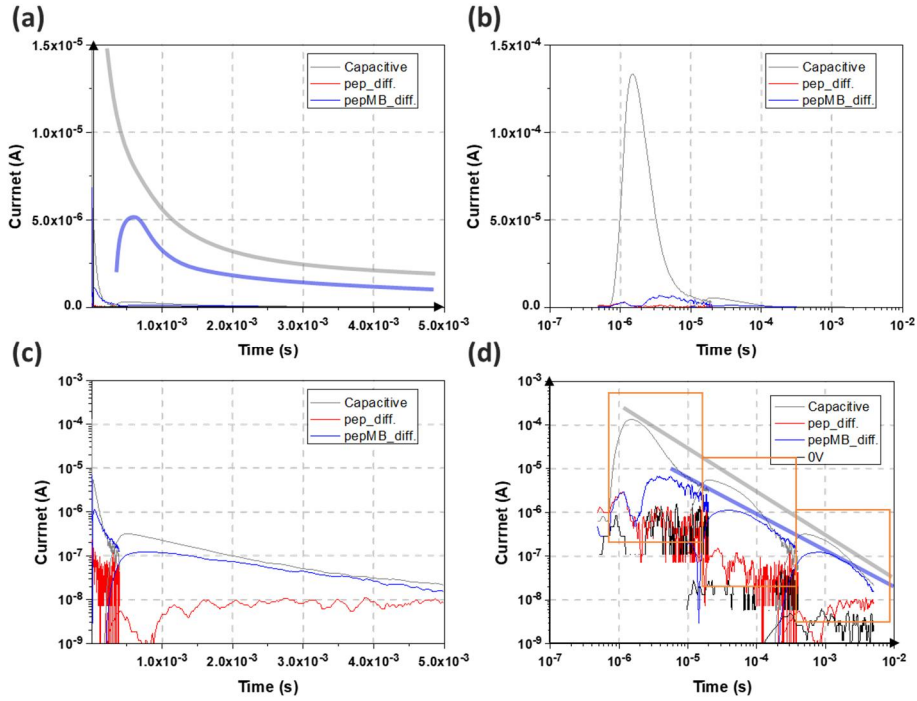


Figure 5-12. Measured plots of the transient current characteristics of the total current (gray) of the T-chip device, the current differences of the pep-SAM (red) device, and the extracted tunneling currents from the pep-MB-SAM device (blue). The transient current characteristics are plotted in (a) linear plot, (b) semi-log-x plot, (c) semi-log -y plot, and (d) log-log plot.

5.4.2. Validation of eliminating capacitive current and extracting tunneling current for voltage pulse method

In the voltage pulse method, it is important to check how the capacitive components are well eliminated and how the tunneling current is well extracted. The mismatch of the capacitive current components can cause an error in the extraction of the tunneling current. The error becomes large especially in the early phase of the voltage pulse since the tunneling current gradually rises in the early phase of the voltage pulse according to the intensity of the electric field and the electron transfer rate in transient time.

To confirm the accuracy of the voltage pulse method the repetitive measurements have been performed with a total 86 devices: 43 for pep-SAM devices and 43 for pep-MB-SAM devices. The current values to be drawn in the histogram in Fig. 5-13 were sampled at 7 μ s, 110 μ s, and 1.1 ms in the transient time for each stage. Each histogram is fitted with the Gaussian distribution. Confusion matrix also known as an error matrix used in statistics and supervised machine learning is obtained from the histogram by varying the cut-off level. In this confusion matrix, the pep-MB-SAM device and pep-SAM device are the type of the dataset. The matrix categorizes the dataset into four divisions, the true positive (TP), the true negative (TN), the false positive (FP), and the false negative (FN). Two

probability values of the true positive rate (sensitivity) and the true negative rate (specificity) can be calculated by the ratio of TP to the total number of pep-MB-SAM devices and that of NP to the total number of pep-SAM devices respectively. What we want to know is the accuracy, how the current difference and the tunneling current are well distinguishable. The accuracy is calculated by dividing the sum of TP and TN with the total number of the devices. The detail explanation and meaning of the well-known basic terminologies are not covered in this chapter.

Receiver operating characteristic (ROC) curve of the two predictors are obtained from the histogram and the confusion matrix of each stage by varying the cut-off value of the current level. One is for the experimental dataset and the other is for the numerically fitted dataset. At the 1st stage estimated accuracy is about 90%, however, at the 2nd and 3rd stage, the estimate accuracies are 100 %, which means that the capacitive current mismatch can be distinguished from the tunneling current.

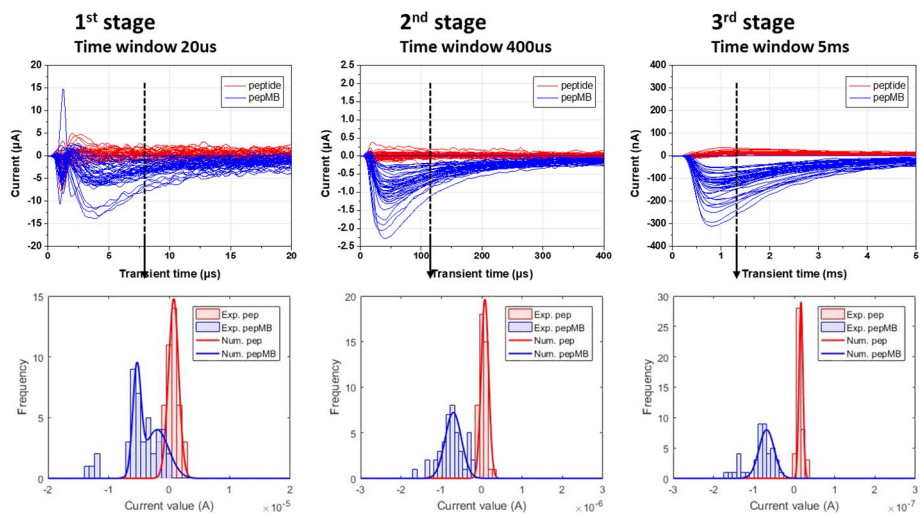
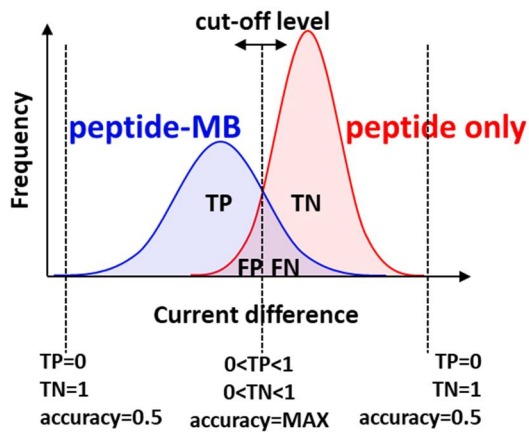


Figure 5-13. Histogram of the current values at 7 μ s, 110 μ s, and 1.1 ms in the transient time for each stage. The total 86 devices: 43 devices for the pep-SAM device (red) and 43 devices for the pep-MB-SAM device (blue) were used.



Cut-off (variable)		Device n (86)		total
		pepMB (43)	pep (43)	total (86)
kif RO	tunnl.	TP (a)	FP (c)	
	cap. diff.	FN (b)	TN (d)	
True Positive rate (Sensitivity)		a/(a+b)		
True Negative rate (Specificity)			d/(c+d)	
Accuracy		(a+d) / n		

Figure 5-14. Confusion matrix also known as an error matrix obtained from the histogram by varying the cut-off level.

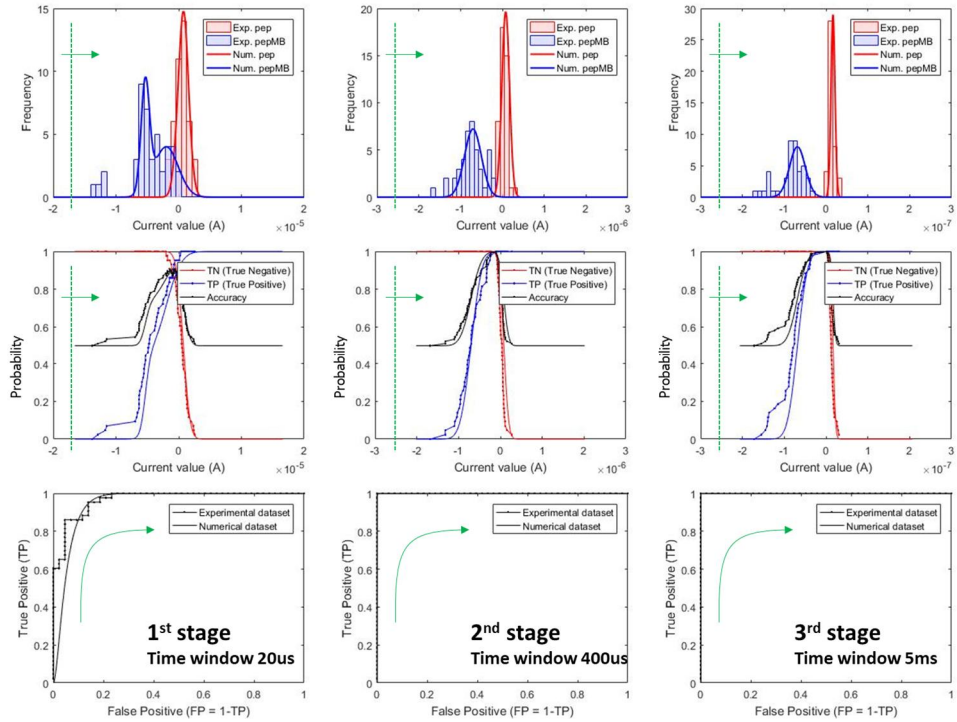


Figure 5-15. Receiver operating characteristic (ROC) curve of the two predictors obtained from the histogram and the confusion matrix of each stage by varying the cut-off value of the current level. One is for the experimental dataset and the other is for the numerically fitted dataset. At the 1st stage the estimated accuracy is about 90%, however, at the 2nd and 3rd stages, the estimate accuracies are 100 %, which means that the capacitive current mismatch can be distinguishable from the tunneling current.

5.4.3. Correlation between the C-V characteristics and results of voltage pulse method

One possible way to verify the validity of the voltage pulse method is to compare the electrostatics C-V characteristics with the result of the voltage pulse method. We applied both measurements to the pep-SAM and pep-MB-SAM devices. At the initial condition, the C-V characteristics of those devices are not stabilized. During the stabilization process for 600 s, the C-V characteristics and the current difference obtained from the voltage pulse method of those devices are monitored.

At first, the C-V characteristics of the pep-SAM device is asymmetric and it is expected that the capacitive current cannot be eliminated by voltage pulse method. The asymmetric C-V characteristics of the pep-SAM device become symmetrical because the structural transformation of the peptide SAM occurs when its structure is stabilized in the electrolyte solution. In the case of the pep-SAM device, the current difference of the pep-SAM device becomes small as the C-V characteristic of that becomes symmetric. The current difference of the pep-MB-SAM device in transient time has negative value after the stabilization because the existence of the electron tunneling from the gold electrode to the MB states under the negative bias causes the asymmetric C-V characteristic of the T-chip device.

To show the validity of the voltage pulse method quantitatively, the relation between the current difference and the positive-to-negative capacitance difference (called PNCD) are plotted. The PNCD value, which is the index to define the degree of the symmetry of the C-V characteristics is calculated from the capacitance values at the positive and negative voltage regions, where their absolute value is same. After the stabilization progressed for 600 s the devices in the electrolyte solution, the correlation between the current difference and PNCD of the pep-SAM device shows the linear trace with the red line while that of the pep-MB-SAM device shows negatively biased trace with the blue line as shown in Fig. 5-18.

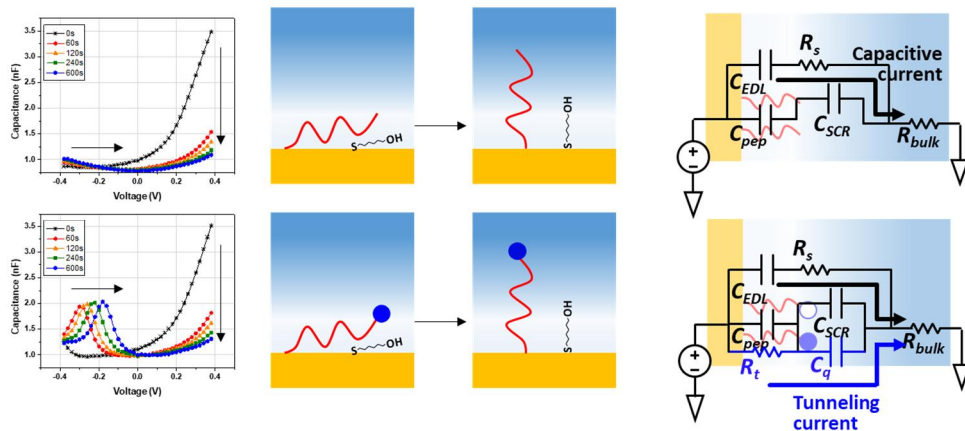


Figure 5-16. C-V characteristics of the pep-SAM (up) and pep-MB-SAM (down) devices and their change in time for 600 s. at the initial condition, the C-V characteristic is asymmetric and the capacitive current cannot be eliminated by voltage pulse method. The asymmetric C-V characteristics of the pep-SAM device becomes symmetrized because the structural transformation of the peptide SAM occurs when its structure is stabilized in the electrolyte solution.

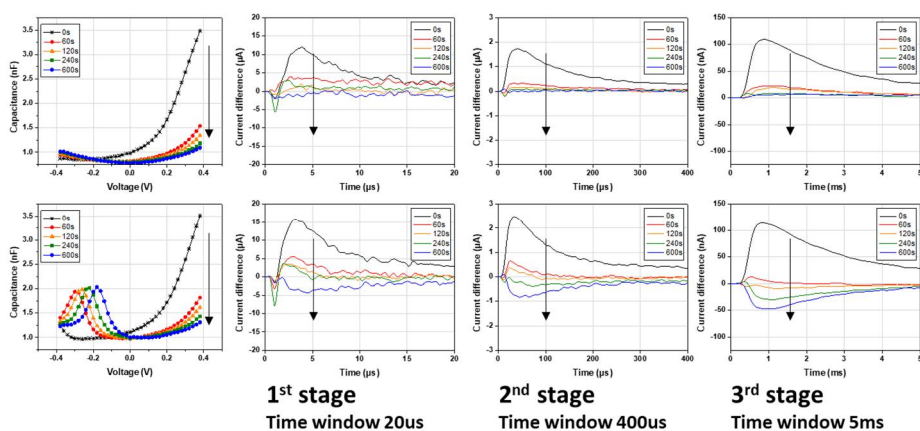


Figure 5-17. Monitored C-V characteristics and the current difference of the pep-SAM device (up) and pep-MB-SAM device (down) for 600 s. In the case of the pep-SAM device, the current difference of the pep-SAM device becomes small as the C-V characteristic of that becomes symmetrized. Whereas the current difference of the pep-MB-SAM device in transient time has negative value after the stabilization, which indicates the electron tunneling at the negative voltage pulse.

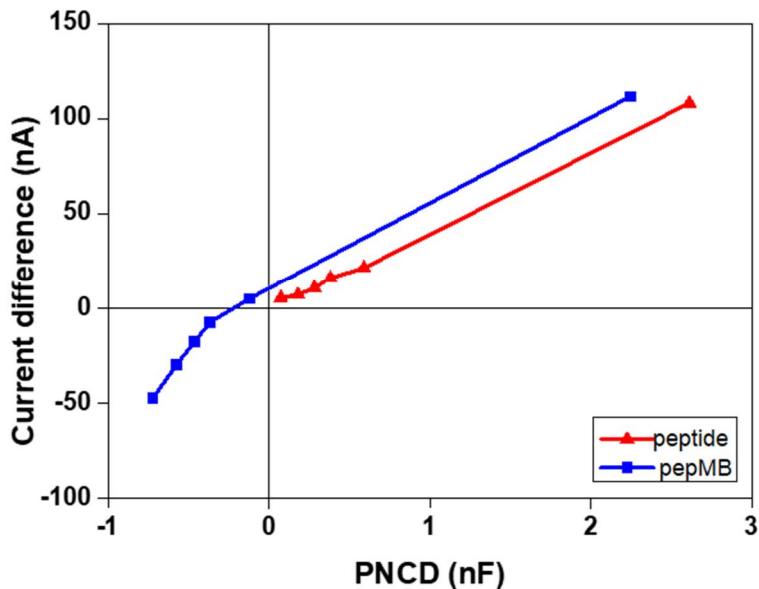


Figure 5-18. Correlation between the current difference and the positive-to-negative capacitance difference (PNCD). The PNCD values are obtained from the maximum values of the capacitance at the positive and negative voltage region of the pep-SAM device and from the peak capacitance value at the negative voltage region and the capacitance value at the positive voltage region where the absolute value of the positive and the negative voltages are same. As the stabilization progressed for 600 s, the correlation between the current difference and PNCD of the pep-SAM device shows linear trace (red) while that of the pep-MB-SAM device shows negatively biased trace (blue).

Chapter 6.

Application to protease biosensor

6.1. Trypsin detection

The detection of Trypsin as a biomarker will be reported. We will show that the method not only gives the better sensitivity but also the better immunity to the nonspecific adsorption effect with the noisy protein than the Cyc-V measurement.

Trypsin, a member of the trypsin family of serine proteases, is secreted by the pancreases and is chosen as an exemplar target biomolecule. Since the discovery of its stable enzymatic property cleaving the carboxyl side of the amino acid arginine, Trypsin has been used to evaluate the performance of protease biosensors. [26], [29]. The concentration of Trypsin was varied from 0 to 100 nM in the DPBS solution, where 500 μ M of bovine serum Albumin (BSA) was dissolved as nonspecific molecules. Because Albumin is the most abundant protein in human serum, we used BSA with an extremely high concentration to imitate the condition of the serum.

6.2. Experimental result of sensing Trypsin

First, the devices were incubated for 180 s under the same bias condition used for the Trypsin detection. The applied bias conditions were as following: Cyc-V measurement (from -0.4 V to +0.2 V with 0.02 steps; 4 s for initial hold time and 10 ms for delay time), and pulse method (-0.4 V and +0.4 V pulses; 2 ms for pulse width and 100 ns for rising time). After device stabilization, 10 μ L of droplets of the Trypsin sample solution were injected onto the devices. The conventional Cyc-V measurement and the suggested pulse method were carried out alternately. Two features were monitored during the reaction time (2000 s): a positive peak current value of the Cyc-V measurement and a tunneling current at 500 μ s in transient time. The intensity of the tunneling current in both measurement methods directly indicated the remaining quantity of the peptide layer yet to be cleaved by Trypsin. Here, we define the index of signal suppression, $S(t_r)$, as follows:

$$S(t_r) = \frac{I(t_r) - I(0)}{I(0)}, \quad (6.2.1)$$

where $I(t_r)$ is the value of the current at a certain reaction time, t_r , which can be the peak current of the Cyc-V measurement or the extracted tunneling current of the pulse method. Now, the current change, $I(t_r) - I(0)$, at a certain reaction time is normalized by $I(0)$, which is the initial value of the current just before the sample solution was incubated.

As shown in Figs. 6-2 and 6-3, Trypsin molecules caused the signal suppression, $S(t_r)$, by cleaving the peptide SAM. The darker (black and blue) lines indicate a higher concentration of Trypsin. The current suppression increases when more peptides are cleaved. The peptide cleaving event is the major factor of signal suppression in the protease biosensor application. The calibration curves of the sensor device for the Cyc-V measurement and the pulse method are plotted in Fig. 6-4. The different background levels of the nonspecific effect are observed in both cases. The limit of detections (LODs) for the Cyc-V measurement and the pulse method were estimated as 30 nM and 10 nM respectively. The pulse method shows slightly better LOD performance than the Cyc-V measurement. The value of LOD was obtained from the concentrations of which sensitivity is the 3-fold standard deviation of the 1 nM data [43] with independent experiments (n=6).

Now let us consider the stability of the sensor device under the pulse bias. As shown in the red line in Fig. 6-3, the device showed the stable characteristic over time for 2000 s under the pulse bias in the DPBS condition. This is because that the amplitude of the pulse is sufficiently small (400 mV) to cause the undesirable effects including the electrolysis of water (1.2 V). In addition, although there may exist the weak electrolysis of water under the pulse bias, the pulse width is sufficiently short to have influence on the stability of the sensor device. When it comes to reusability of the sensor, this peptide platform is not appropriate for reuse. Unlike the antibody

or DNA used in affinity biosensor platforms, the probe peptide used in this platform is cleaved by the target proteins. However, the gold electrode of the device might be reusable if the probe peptide can be removed with a proper cleaning process.

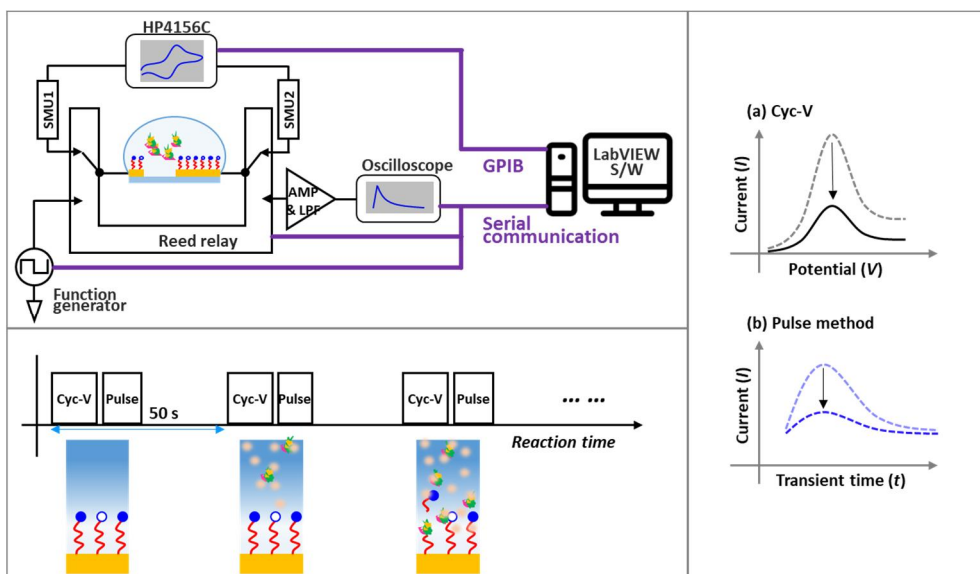


Figure 6-1. The measurement configuration of the experiment. The monitored features are (a) the positive peak current value of the Cyc-V measurement and (b) the current value at 500 μ s in transient time.

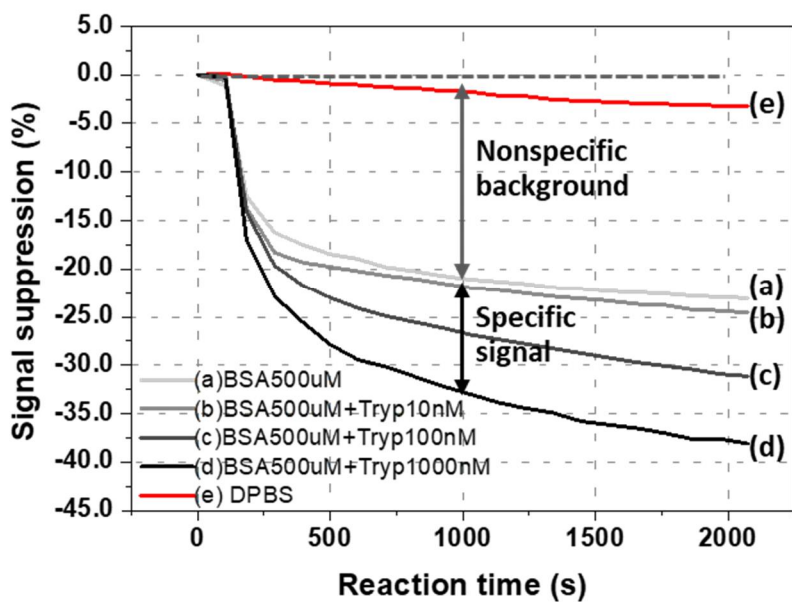


Figure 6-2. Signal suppression of the peak current in the Cyc-V measurement as a function of reaction time. (a) The nonspecific BSA is dissolved in DPBS as a control. (b)–(d) Concentration of Trypsin is varied from 10 to 1000 nM. (e) The device is incubated under the pure DPBS condition.

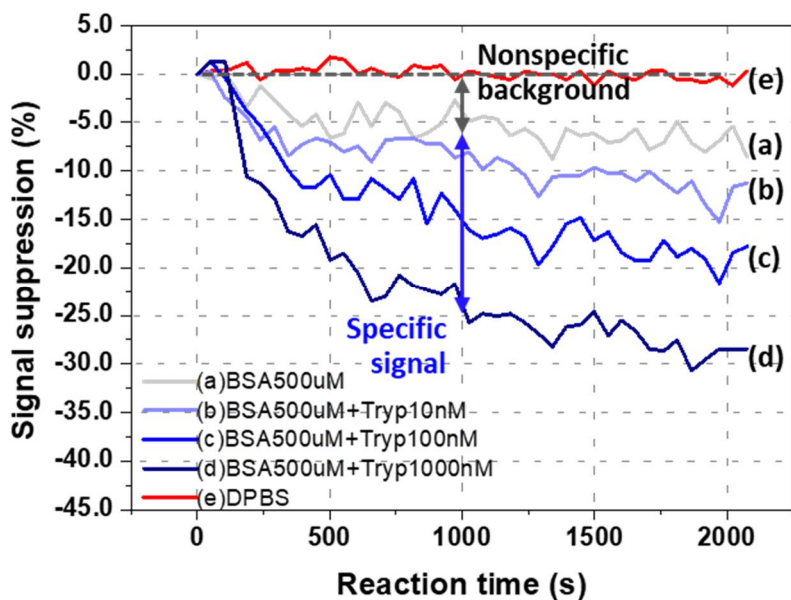


Figure 6-3. Signal suppression of the tunneling current extracted from the pulse method. (a) The nonspecific BSA is dissolved in DPBS as a control. (b)–(d) The Trypsin concentration is varied from 10 to 1000 nM. (e) The device is incubated in the pure DPBS condition. Compared to the Cyc-V in Fig. 6-1, the nonspecific effect is reduced and the sensitivity is enhanced.

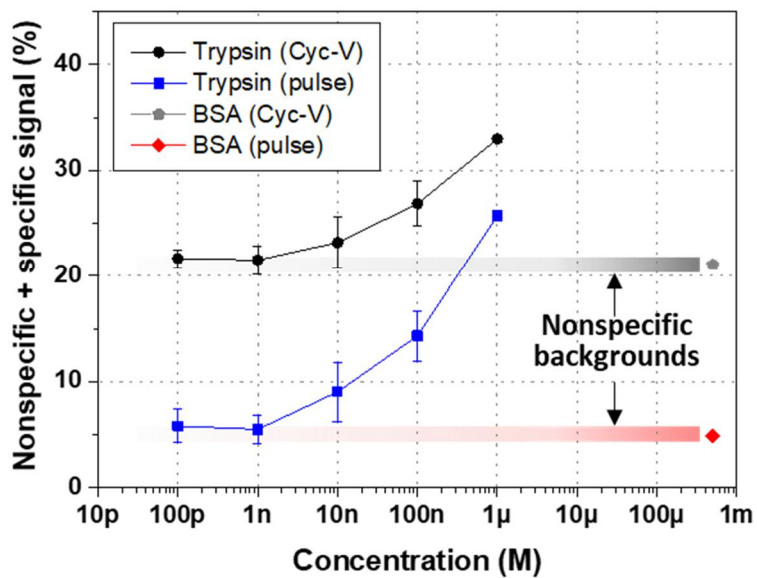


Figure 6-4. Calibration curves of the sensor device for the Cyc-V measurement (the black line) and the pulse method (the blue line). Different background levels of the nonspecific effect (the gray and red lines) are observed in both cases.

6.3. Effect of nonspecific adsorption

The current was also degraded in the case where only a high concentration of the nonspecific BSA protein was injected, in order to serve the control experiment (the lightest gray lines (a) in Figs. 6-2 and 3). The experimental results showed that $S(t_r)$ includes not only the specific signal (SS) of the cleaving event but also the nonspecific effect (NS).

$$S(t_r) = SS(t_r) + NS(t_r). \quad (6.3.1)$$

Here, we introduce an additional index to evaluate the performance of the measurement method. The specific-to-nonspecific effect ratio, $SNR(t_r)$, can be defined as follows, which is quite similar to the signal-to-noise ratio used in general electronic sensors.

$$SNR(t_r) = \frac{SS(t_r)}{NS(t_r)}. \quad (6.3.2)$$

As shown in Fig. 6-5, the SNR in the case of the pulse method is much higher than that in the case of Cyc-V measurement. This indicates that the influence of nonspecific binding on the tunneling current becomes weaker in the transient time region.

Although a complex atomic interaction might exist between the nonspecific molecules and the probe molecule, we speculate one possible mechanism from the perspective of the equivalent circuit by introducing the nonspecific component, C_{BSA} (Fig. 6-6). When BSA molecules diffuse from the bulk solution and are adsorbed on the peptide layer, we can consider BSA as an additional insulator between the SAM and electrolyte solution. Serially connected C_{BSA} modulates the total capacitance of the device and reduces the capacitive components of C_q effectively. Therefore, without any peptide cleaving event, the effective C_q of MB can decrease due to the nonspecific adsorption of the BSA protein.

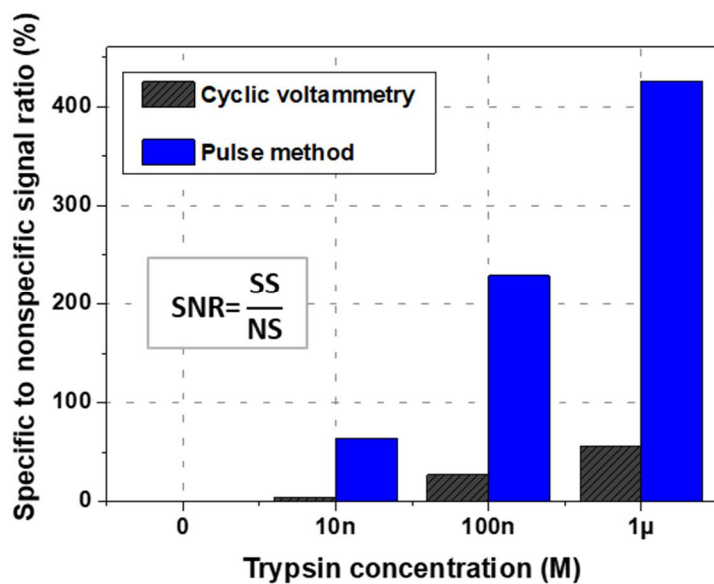


Figure 6-5. Specific-to-nonspecific signal ratio, SNR ($t_r=1000$ s), of the sensor device adopting the conventional Cyc-V and the suggested pulse method.

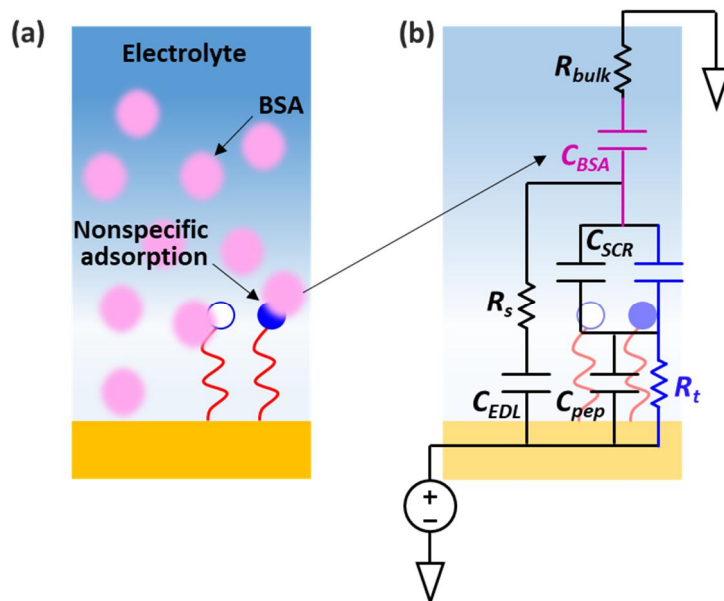


Figure 6-6. (a) Schematic of nonspecific adsorption and (b) its representation as a series capacitance C_{BSA} in equivalent circuit.

Chapter 7.

Conclusion

The electrochemical biosensor based on the electron tunneling between a metal electrode and redox states at the other end of the attached probe molecules has been considered as one of the unique platforms to measure enzymatic reaction between the target and probe molecules. The biochemical state of the device surface can be characterized and the concentration of the target molecules in the electrolyte solution can be estimated by observing the tunneling current as the electrical signal.

In this dissertation, the fundamental electrochemical characteristics of the sensor device with the redox-modified peptide self-assembled monolayer (SAM) is explained. The T-chip platform is based on the two electrode device free of the reference electrode. By adopting the self-gating effect, the two electrode device with the small working and the large counter electrode can stabilize the electrical potential of the bulk electrolyte solution. Not only cyclic-voltammetry (Cyc-V) used in the conventional electrochemical measurement, but also the quasi-static

capacitance voltage measurement (QSCV) used for characterizing the surface physics of the solid-state devices, are introduced to investigating the capacitive characteristics of the T-chip platform. From the capacitance-voltage (C-V) measurement, the equivalent circuit of the T-chip device is proposed. The effect of each component of the equivalent circuit has been analyzed by the modified nodal analysis (MNA) technique.

By adopting the peptide SAM as a probe molecule, the capacitance characteristic of the T-chip becomes quite symmetrized with the polarity of the applied bias and its nonlinearity is moderated. Additionally, by considering the peptide SAM as an insulator layer, the geometric structure of the metal-SAM (insulator)-electrolyte (MIE) device is similar to that of the metal-oxide-semiconductor (MOS) device. In the perspective of the electrostatics, both MIE and MOS structures share the similar capacitance components. Considering redox states, here methylene blue (MB), in MIE device as interface traps (or oxide traps) in MOS device, the electron tunneling phenomenon can be described by introducing the electrochemical (trap) capacitance and the tunneling resistance.

The voltage pulse method has been suggested to extract the transient tunneling characteristics in the early phase of the voltage pulse. In transient time, after applying the pulse, the capacitive current and the tunneling current rapidly decreases. By utilizing the symmetrized C-V characteristics of the T-chip device with SAM

with different polarity of the bias voltage, the transient tunneling characteristics can be extracted by subtracting the current components from the positive and the negative pulses.

The detection of Trypsin as the target molecule has been performed to demonstrate the performance of the T-chip device as the protease biosensor. The Cyc-V measurement and the voltage pulse method are applied alternately to compare the performance of both techniques. To imitate the human serum condition, 500 μM of BSA is chosen as the nonspecific protein and the target Trypsin was dissolved in the BSA abundant solution. The pulse method enhanced the sensitivity of the sensor device and shows higher specific-to-nonspecific ratio than the Cyc-V measurement.

In addition, the effect of the back-filling materials has been studied and the optimized structure of the T-chip device is established (see Appendix 1). The biomolecular transport in the bulk electrolyte solution and the biochemical reaction is simulated by solving the reaction-diffusion equation in reaction time. The equivalent circuit of the T-chip device is also proposed and analyzed by using the MNA technique (see Appendix 2). To overcome the limitation and increase the sensitivity of the voltage pulse method, the generalized voltage pulse method (see Appendix 3) based on integration of the tunneling current (so called the total charge) is suggested. Finally, pH sensor application (see Appendix 4) is demonstrated by the

T-chip device utilizing the MCH-SAM.

In conclusion, the T-chip platform is of great potential in the POCT application but also for understanding the surface electrochemistry and physics of the metal electrode decorated with various SAM conditions and electrolyte solution interface. The voltage pulse method is suggested to enhance the performance of the T-chip device by extracting the tunneling current from the capacitive dominant total transient current characteristics.

Appendix 1.

Appendix 1. Effect of back-filling material

A1.1. MB-modified peptide and back-filling materials of MCXs

The sequence of the peptide (Gly-Pro-Leu-Gly-Met-Trp-Ser-Arg-Cys; GPLGMWSRC) was selected as the SAM and its end terminal was modified with MB as a redox molecule. The immobilization process was same with the following references. [22], [26] The MCXs with three different lengths were used: 1) 3-Mercapto-1-propanol (MCP), 6-Mercapto-1-hexanol (MCH), and 9-Mercapto-1-nonanol (MCN).

A1.2. Trypsin as a target molecule

Trypsin, a serine protease, secreted by the pancreases was chosen as a target biomarker. Since its stable enzymatic property, trypsin has been used to evaluate the performance of protease biosensors.

A1.3. Measurement configuration

The cyclic-voltammetry (Cyc-V) measurement were performed by using HP-4165C equipment to investigate the electrochemical characteristics of the device and to measure the current response which indicated biomarker detection. The stair-case voltage sweep was applied from -0.4 V to +0.2 V with 0.02 V of the voltage steps and 200 ms of the stair-width. The hold time and the integration time was 4 s and 1 ms respectively.

A1.4. Experiment for optimization of device condition

The three different lengths of back-filling materials were immobilized on the gold electrode surface as shown in Fig. A1-1. The peptide device without the back-filling material was also prepared. The I-V characteristics from Cyc-V measurement were automatically obtained (programmed by LabVIEW). The positive peak current values indicating the electron tunneling between the gold electrode and the MB state were monitored for the four cases of the electrode modification in real-time. After 250 s of the stabilization time, 10 μ L droplets of Trypsin sample solution of 1 μ M Trypsin were injected into the devices. The cleaving event between Trypsin and the probe peptide causes the signal suppression of the peak current values.

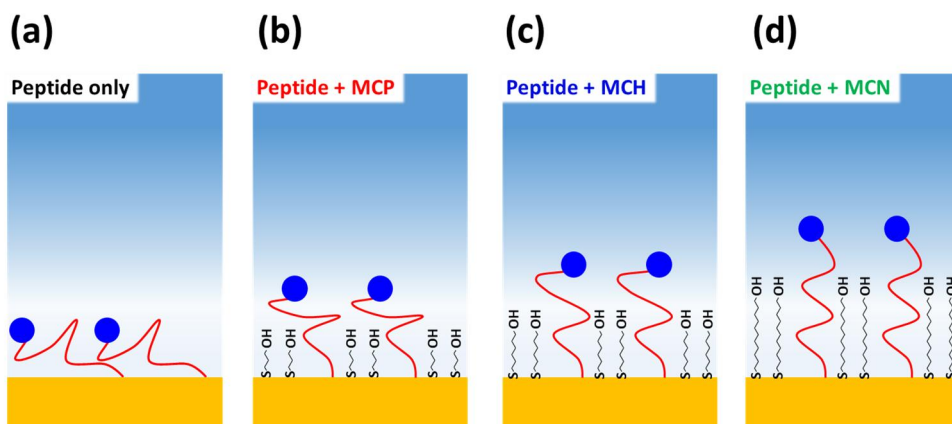
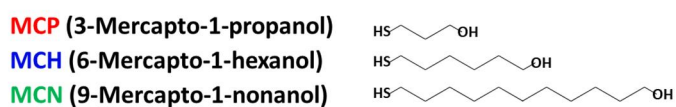


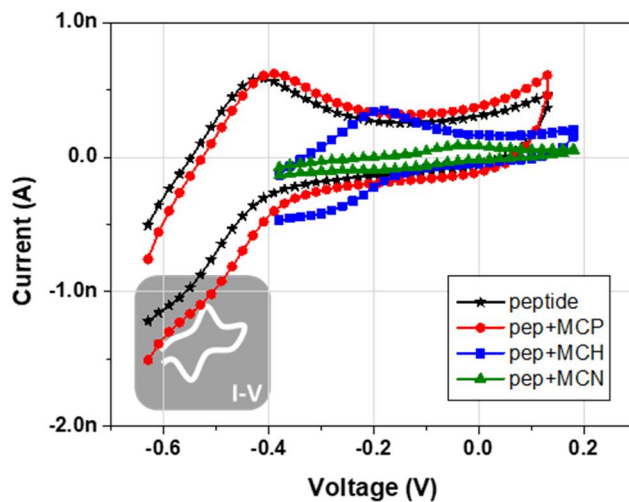
Figure A1-1. (a) Schematics of the peptide-MB only device, peptide-MB with MCP, peptide-MB with MCH, and peptide-MB with MCN.

A1.5. Effect of the back-filling materials of MCXs

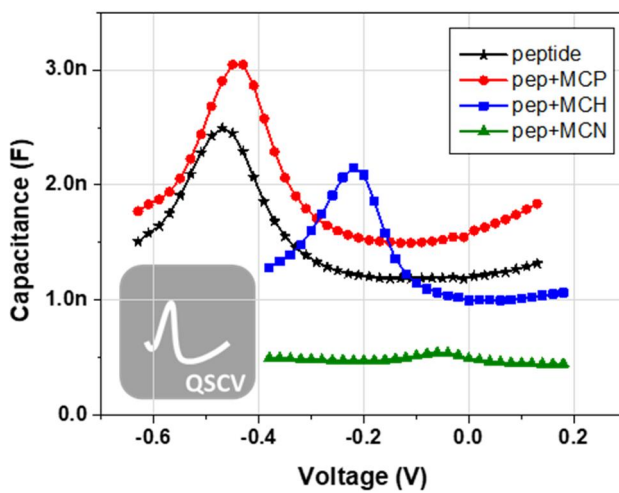
The I-V and C-V characteristics of the peptide only, peptide with MCP, peptide with MCH, and peptide with MCN devices obtained from the Cyc-V and the QSCV measurements are shown in Fig. A1-2. The monitored peak current values of the I-V characteristics of each device is plotted in Fig. A1-3. The suppressed signal values were normalized by the current values right before the injection of the Trypsin sample solution at 250 s. The maximum current change was shown in the case of the peptide device with the back-filling material of MCH (the blue line). The other three cases showed similar but less changes than MCH; MB-peptide only (the black line), back-filing material of MCP (the red line), and MCN (the green line). Because the cleaving site of the peptide sequence (carboxyl side of the amino acid arginine) is located close to the electrode surface, the longest back-filling material of MCN hindered the approach of the target biomolecule. In the other cases with shortest back-filling material of MCP and without back-filling material, the probe sequence cannot form proper structure in the electrolyte solution. Although the Trypsin can approach the cleaving site of the probe peptide, the reaction activity between the probe peptide and Trypsin decreased.

We investigated the length effect of the back-filling materials immobilized on

the gold electrode surface of the T-chip devices. The back-filling material of MCH showed the best detection performance due to its proper length. MCH assisted the probe peptide to form its optimized structure in electrolyte solution and do not hinder the approach of the Trypsin molecule.



(a)



(b)

Figure A1-2. (a) I-V characteristics and (b) C-V characteristics of the T-chip device with different back-filing material conditions.

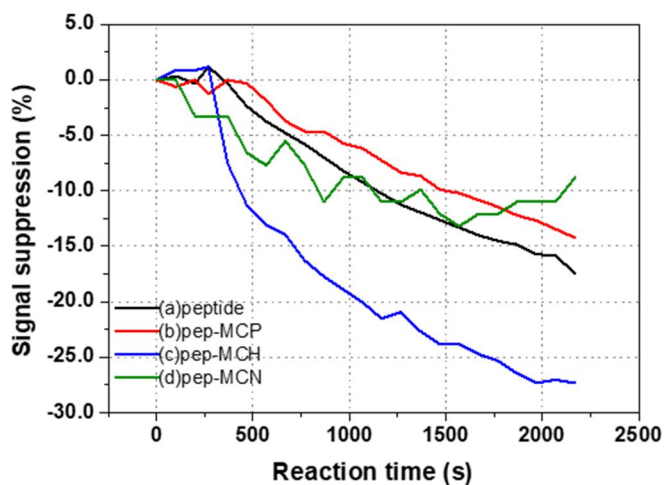


Figure A1-3. Monitored peak current values of the I-V characteristics of each device. The suppressed signal values were normalized by the current values right before the injection of the Trypsin sample solution at 250 s. The maximum current change was shown in the case of the peptide device with the back-filing material of MCH (the blue line). The other three cases showed similar but less changes than MCH; MB-peptide only (the black line), back-filing material of MCP (the red line), and MCN (the green line).

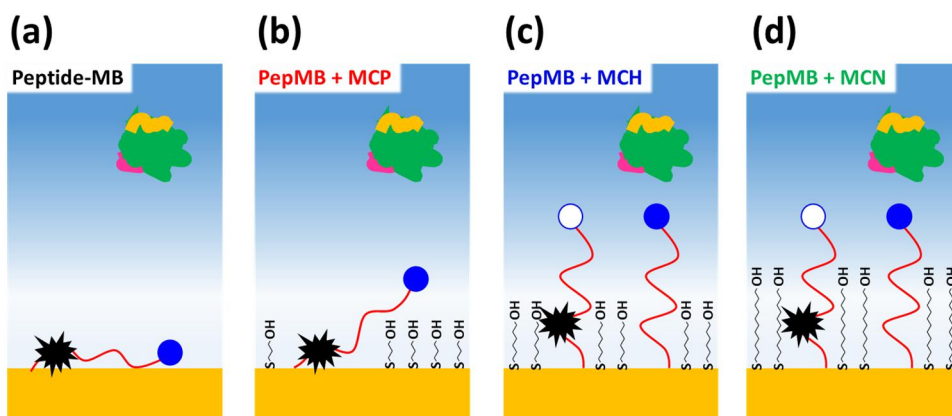


Figure A1-4. Schematic view of the peptide cleaving event. Because the cleaving site of the peptide sequence (carboxyl side of the amino acid arginine) is located close to the electrode surface, the longest back-filling material of MCN hindered the approach of the target biomolecule. In the other cases with shortest back-filling material of MCP and without back-filling material, the probe sequence cannot form proper structure in the electrolyte solution. Although the Trypsin can approach the cleaving site of the probe peptide, the reaction activity between the probe peptide and Trypsin decreased.

Appendix 2.

Appendix 2. Numerical simulation

A2.1. Diffusion and reaction of biomolecules in electrolyte

The biomolecular transport and the probe-target molecular interaction is the one of the interest. Since it is impossible to optically observe what happens in the electrolyte solution and the electrode surface in electrolyte solution, the numerical simulation can be a tool to predict the situation on the electrode surface. It is important to describe the molecular transport and biochemical reaction in the solution because there can be found the crucial insight when understanding the fundamental physics of the device, analyzing the performance of the biosensor, and developing the improved structural or methodological design of the platform.

Here, we used the diffusion equation and Menten-Michaelis kinetics for the reaction-diffusion system as a mathematical model. The methodological intuition of the simulation has been brought from that of the negative-bias temperature

instability (NBTI) which deals with reliability issue on MOSFETs in the semiconductor field. A precursor molecule diffused from the silicon oxide to the interface. The dissociation of Si-H bonds creates Si* trap states which cannot be recovered over a reasonable time considered as permanent traps and is the same as the one created by channel hot carrier and produces hydrogen molecules. The hydrogen molecule diffuses away from the interface increasing the number of the Si* states. In this situation, the Si-H bond and precursor molecule corresponds to the probe peptide and the target protease protein respectively. The Si* state and the hydrogen molecule corresponds to the cleaved peptide immobilized on the electrode surface and the other side of the cleaved one which diffuses away from the electrode surface to the bulk electrolyte solution. In addition, the mechanism of the dissociation of Si-H bond can correspond to the enzymatic cleaving event between the probe peptide and the target protein. This one-to-one correspondence allows us to simulate the situation at electrode surface with the transportation and the biochemical reaction of the biomolecules in the same manner of the NBTI.

The 1-D diffusion equation and Menten-Michaelis kinetics are solved by decoupled method. The 1-D diffusion equation is solved by finite difference and backward Euler method. The diffusion equation and its discretized form is as follows.

$$D_N \frac{d^2N}{dx^2} = \frac{dN}{dt} \tag{A2.1.1}$$

protein, and surface concentration of the substrate, the probe peptide). The surface concentration of the intermediate state of the enzyme and the substrate is expressed as ES_s and it is cleaved by the kinetic rate of k_{cat} . k_f and k_r are the association and dissociation rate constants for the enzyme and the substrate.

The reflecting boundary condition are used for every molecule: the target molecule and the cleaved and probe peptide which diffuses away from electrode surface to the bulk electrolyte solution since, there is no flux flows inward and outward the boundary of the electrolyte solution. whereas for the immobilized peptide-SAM and the leaved peptide fragment, P_s , on the electrode surface, the Neumann boundary condition is used, which is corresponds to the Fick's 1st law and the reaction kinetics equation as following.

$$\frac{d[E]}{dx} = 0 \quad \text{Reflecting B.C.} \quad (\text{A2.1.8})$$

$$\frac{d[P_s]}{dt} = +k_{cat}[ES_s] \quad \text{Reaction kinetics} \quad (\text{A2.1.9})$$

$$\frac{d[P_s]}{dt} = -D_p \frac{d[P]}{dx} \quad \text{Fick's 1st Law} \quad (\text{A2.1.10})$$

$$\frac{d[P]}{dx} = -\frac{1}{D_p} \frac{d[P_s]}{dt} \quad \text{Neumann B.C.} \quad (\text{A2.1.11})$$

The solution of the reaction-diffusion model is shown in Fig. A2-5. The left side graph of the figure shows the bulk concentration of the target protein and the fragment of the probe peptide generated by the probe-target cleaving event. The

right side one shows the normalized sum of the surface concentration of the probe peptide and the peptide-enzyme intermediate states.

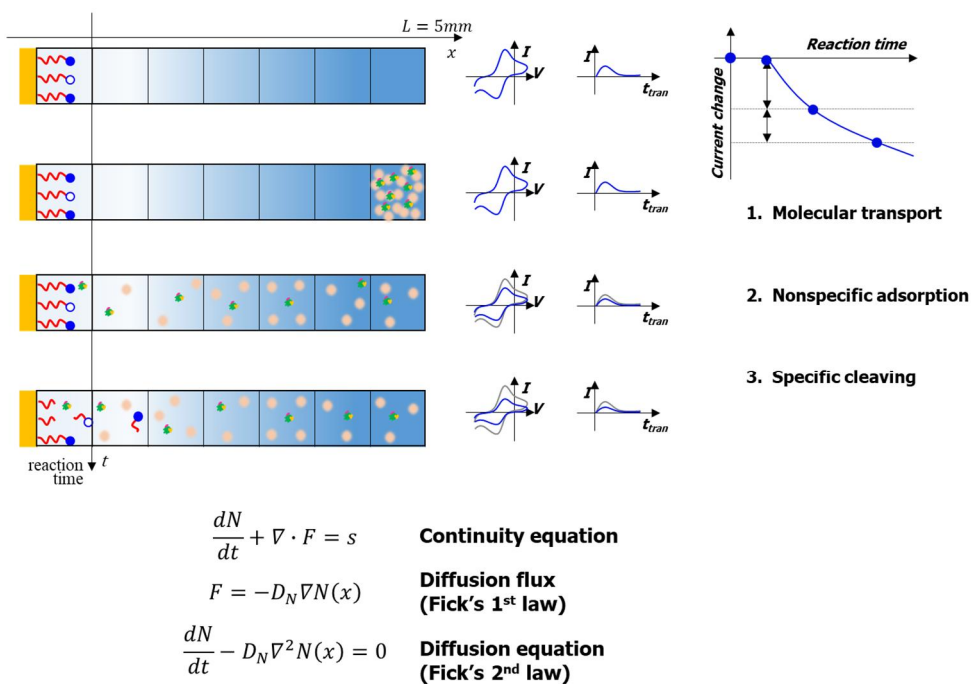
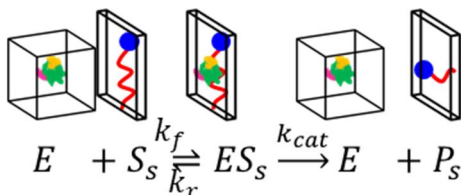


Figure A2-1. Schematic illustration of the 1-D diffusion equation.

Menten-Michaelis kinetics

Reaction on the electrode surface



$$[E] \quad /cm^3 \quad k_f \quad cm^2/s$$

$$[S_s] \quad /cm^2 \quad k_r \quad 1/s$$

$$[ES_s] \quad /cm^2 \quad k_{cat} \quad 1/s$$

$$[P_s] \quad /cm^2$$

$$\frac{d[E]}{dt} = -k_f[E][S_s] + k_r[ES_s] + k_{cat}[ES_s]$$

$$\frac{d[S_s]}{dt} = -k_f[E][S_s] + k_r[ES_s]$$

$$\frac{d[ES_s]}{dt} = +k_f[E][S_s] - k_r[ES_s] - k_{cat}[ES_s]$$

$$\frac{d[P_s]}{dt} = +k_{cat}[ES_s]$$

Figure A2-2. Menten-Michaelis kinetics

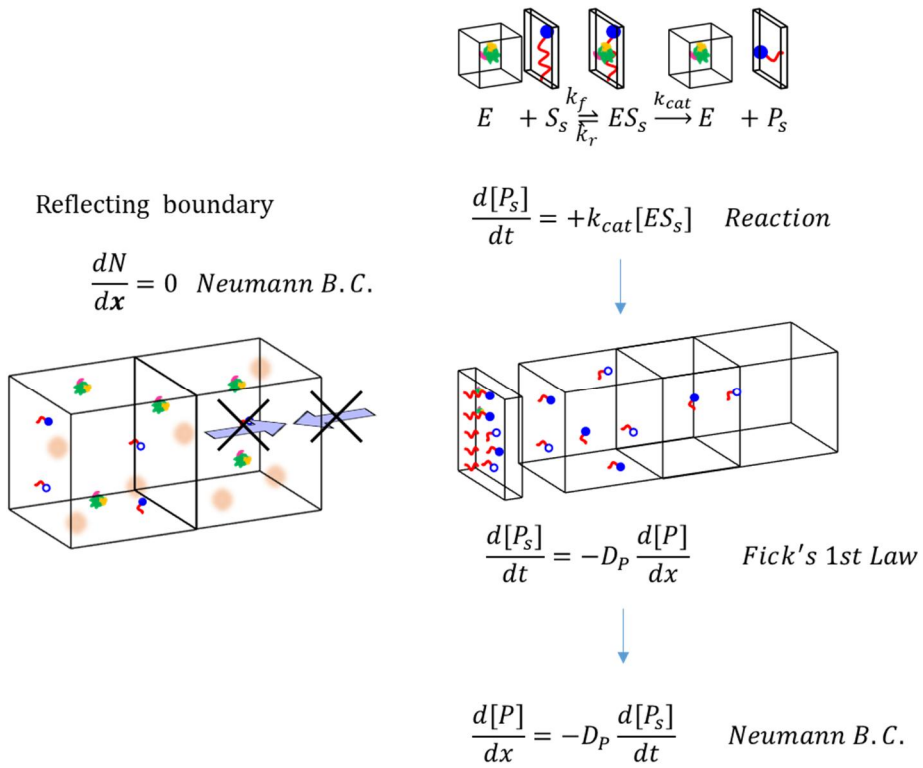


Figure A2-3. Reflecting boundary condition and Neumann boundary condition.

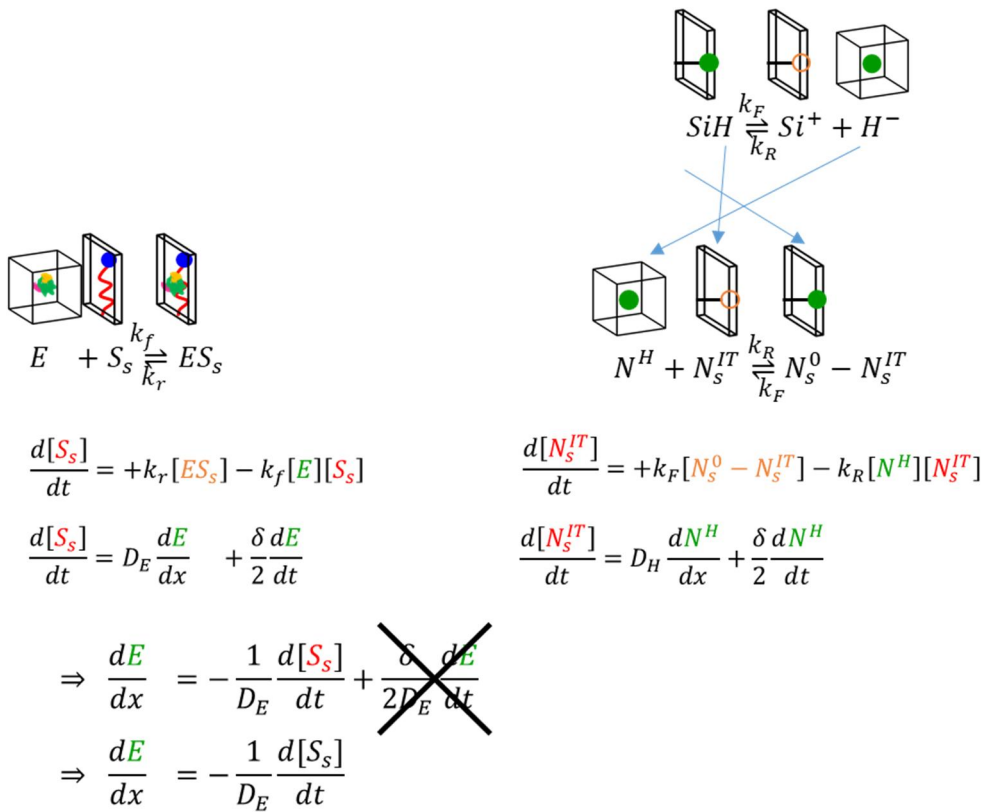


Figure A2-4. Correspondence between Menten-Michaelis kinetics and the NBTI model.

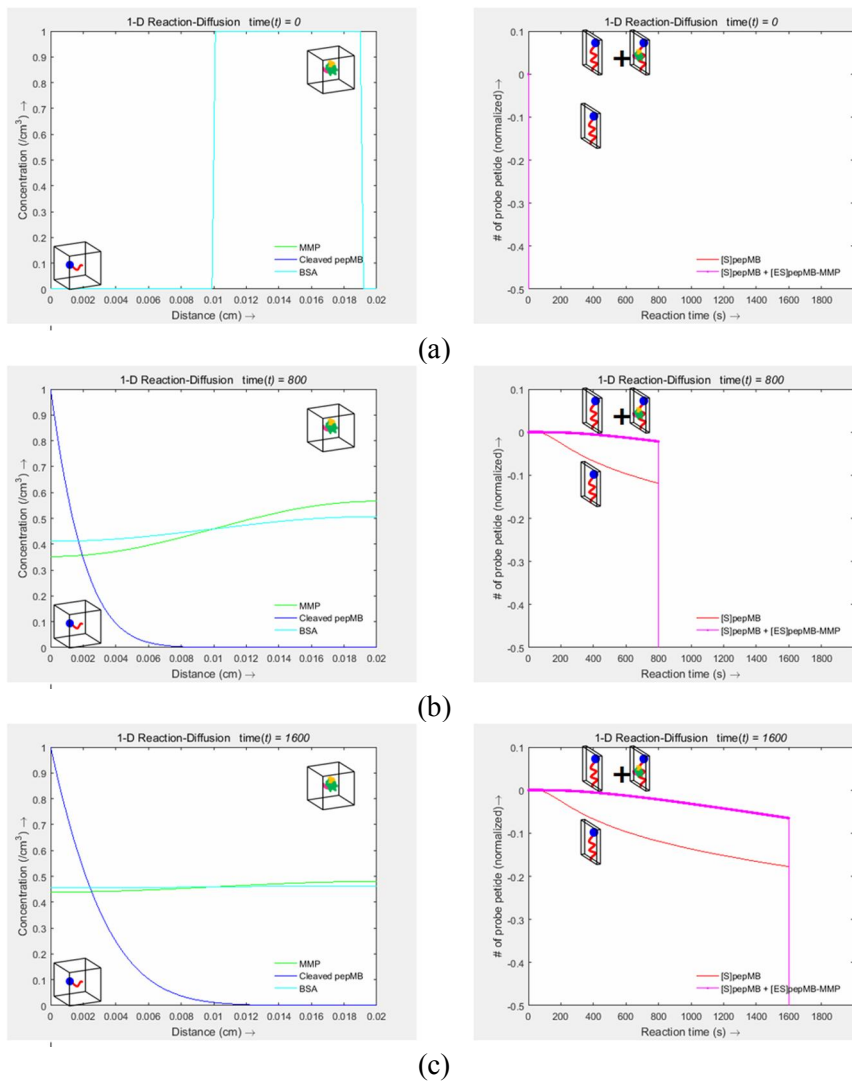


Figure A2-5. Solution of the reaction-diffusion equation at the reaction time (a) 0, (b) 800, and (c) 1600 s. (left) Bulk concentration of the target protein (green) and the fragment of the probe peptide (blue) generated by the probe-target cleaving event. (right) Normalized surface concentration of the probe peptide (purple) and sum of that and the peptide-enzyme intermediate states (red).

A2.2. Modified Nodal Analysis

In the previous chapter the equivalent circuit and its components were suggested to describe the electrochemical characteristics of the T-chip device using the nonlinear capacitance components. This equivalent circuit with nonlinear component can be analyzed by using Modified Nodal Analysis (MNA). In this research, for the faster simulation and for the better convergence of the solution, the circuit is calculated by solving the linear algebraic equation (LAE) with companion models [44] for the nonlinear components rather than solving the differential algebraic equation (DAE) directly. The exemplary matrix equation for the R-C circuit is shown as

$$\begin{pmatrix} +C/h & -C/h & -1 \\ -C/h & +C/h + g & 0 \\ 1 & 0 & 0 \end{pmatrix} \begin{pmatrix} v_1^{n+1} \\ v_2^{n+1} \\ i_1^{n+1} \end{pmatrix} = \begin{pmatrix} C/h (v_1^n - v_2^n) \\ -C/h (v_1^n - v_2^n) \\ V_{in} \end{pmatrix} \quad (\text{A2.2.1})$$

where g and C are the conductance and the capacitance value. And v_1^{n+1} and i_1^{n+1} are the node voltage and the current to be calculated under the voltage source, V_{in} with time step h .

To solve the matrix by using Newton-Raphson method, Jacobian matrix is required. However, in the circuit simulation the circuit components should be added and removed freely for flexible description of the T-chip device. The size and the

elements of the matrix equation and its Jacobian matrix must be changed automatically for the efficient simulation. In addition, this MNA includes the nonlinear circuit component. Since it is impossible to compose the elements of Jacobian matrix by deriving their derivatives analytically, we introduce the numerical Jacobin matrix which can change its size and the elements automatically according to the given matrix equation.

$$F(x) = A(x)x - b$$

$$= \begin{pmatrix} +C_k(v_c^{n+1})/h & -C_k(v_c^{n+1})/h & -1 \\ -C_k(v_c^{n+1})/h & +C_k(v_c^{n+1})/h + g_k(v_2^{n+1}) & 0 \\ 1 & 0 & 0 \end{pmatrix} \begin{pmatrix} v_1^{n+1} \\ v_2^{n+1} \\ i_1^{n+1} \end{pmatrix} - \begin{pmatrix} C_k/h (v_1^n - v_2^n) \\ -C_k/h (v_1^n - v_2^n) \\ V_{in} \end{pmatrix} \quad (A2.2.2)$$

where $F(x)$ is the matrix equation with the matrix $A(x)$ with nonlinear elements, the vector x desired to solve, and the vector b , which can be composed by the aforementioned manner.

In brief explanation, by using the numerical Jacobian matrix J_{num} and iterating the equations (A2.2.2) to (A2.2.5) the solution vector x can be obtained when the vector difference y of the vector x_{new} and x_{old} become considerably small.

$$J_{num} = \frac{F(x + \delta x) - F(x)}{\delta x}$$

$$= \begin{pmatrix} \frac{F_1(x + \delta x_1) - F_1(x)}{\delta x_1} & \dots & \frac{F_1(x + \delta x_3) - F_1(x)}{\delta x_3} \\ \vdots & \frac{F_2(x + \delta x_2) - F_2(x)}{\delta x_2} & \vdots \\ \frac{F_3(x + \delta x_3) - F_3(x)}{\delta x_1} & \dots & \frac{F_3(x + \delta x_3) - F_3(x)}{\delta x_3} \end{pmatrix} \quad (\text{A2.2.3})$$

$$y = J^{-1}F \quad (\text{A2.2.4})$$

$$x_{new} = x_{old} - y \quad (\text{A2.2.5})$$

In Fig. A2-9, the equivalent circuit of the T-chip device for MNA simulation and its simulated the I-V characteristics is plotted in the case of the initial condition (blue) and the case of the device with BSA capacitance, which describe the nonspecific effect to the circuit component equivalently. Each circuit component was dealt with in the previous chapter.

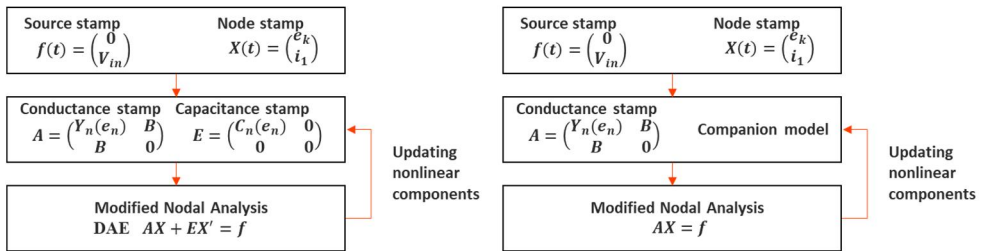
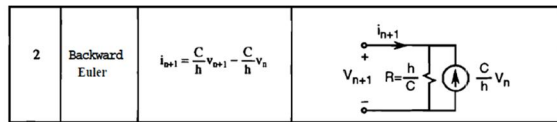
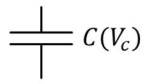
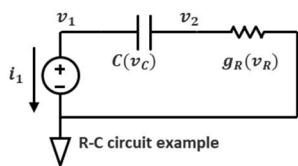


Figure A2-6. (left) MNA by solving the differential algebraic equation and (right) the linear algebraic equation with the companion model.



Differential Algebraic Equation
 $Ax + Ex' = b$

$$\begin{pmatrix} 0 & 0 & -1 \\ 0 & +g_k & 0 \\ 1 & 0 & 0 \end{pmatrix} \begin{pmatrix} v_1 \\ v_2 \\ i_1 \end{pmatrix} + \begin{pmatrix} +C_k & -C_k & -1 \\ -C_k & +C_k & 0 \\ 1 & 0 & 0 \end{pmatrix} \frac{d}{dt} \begin{pmatrix} v_1 \\ v_2 \\ i_1 \end{pmatrix} = \begin{pmatrix} 0 \\ 0 \\ V_{in} \end{pmatrix}$$

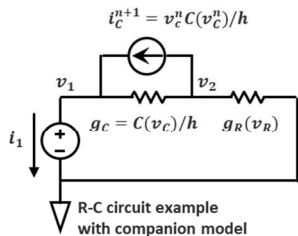


$$\begin{pmatrix} 0 & 0 & -1 \\ 0 & +g_k & 0 \\ 1 & 0 & 0 \end{pmatrix} \begin{pmatrix} v_1^{n+1} \\ v_2^{n+1} \\ i_1^{n+1} \end{pmatrix} + \begin{pmatrix} +C_k & -C_k & -1 \\ -C_k & +C_k & 0 \\ 1 & 0 & 0 \end{pmatrix} \frac{1}{h} \begin{pmatrix} v_1^{n+1} \\ v_2^{n+1} \\ i_1^{n+1} \end{pmatrix} = \begin{pmatrix} v_1^n \\ v_2^n \\ V_{in} \end{pmatrix}$$



Linear Algebraic Equation
 $Ax = b$

$$\begin{pmatrix} +C_k/h & -C_k/h & -1 \\ -C_k/h & +C_k/h + g_k & 0 \\ 1 & 0 & 0 \end{pmatrix} \begin{pmatrix} v_1^{n+1} \\ v_2^{n+1} \\ i_1^{n+1} \end{pmatrix} = \begin{pmatrix} C_k/h (v_1^n - v_2^n) \\ -C_k/h (v_1^n - v_2^n) \\ V_{in} \end{pmatrix}$$



Source stamp

$$b(t) = \begin{pmatrix} 0 \\ V_{in} \end{pmatrix}$$

Conductance stamp

$$A(x) = \begin{pmatrix} +g_k(v_k) & -g_k(v_k) \\ -g_k(v_k) & +g_k(v_k) \end{pmatrix}$$

Node stamp

$$x(t) = \begin{pmatrix} v_k \\ i_i \end{pmatrix}$$

Capacitance stamp

$$E(x) = \begin{pmatrix} +C_k(v_k) & -C_k(v_k) \\ -C_k(v_k) & +C_k(v_k) \end{pmatrix}$$

Figure A2-7. Example of MNA for the R-C circuit and its matrix formulations of DAE and LAE with the companion model.

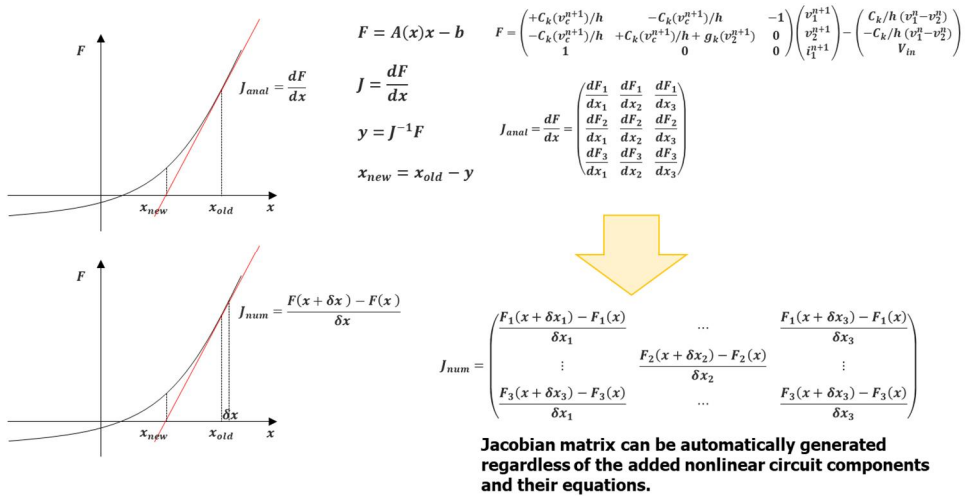


Figure A2-8. (up) Jacobian matrix and its elements calculated analytically. (down) Numerical Jacobian matrix and its elements, which can change its size and the elements automatically according to the given matrix equation.

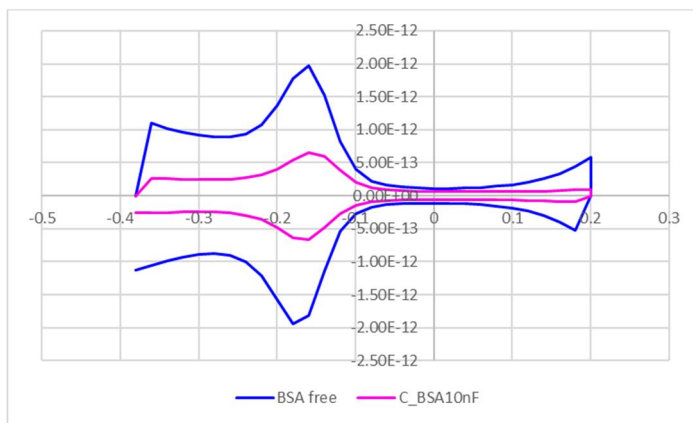
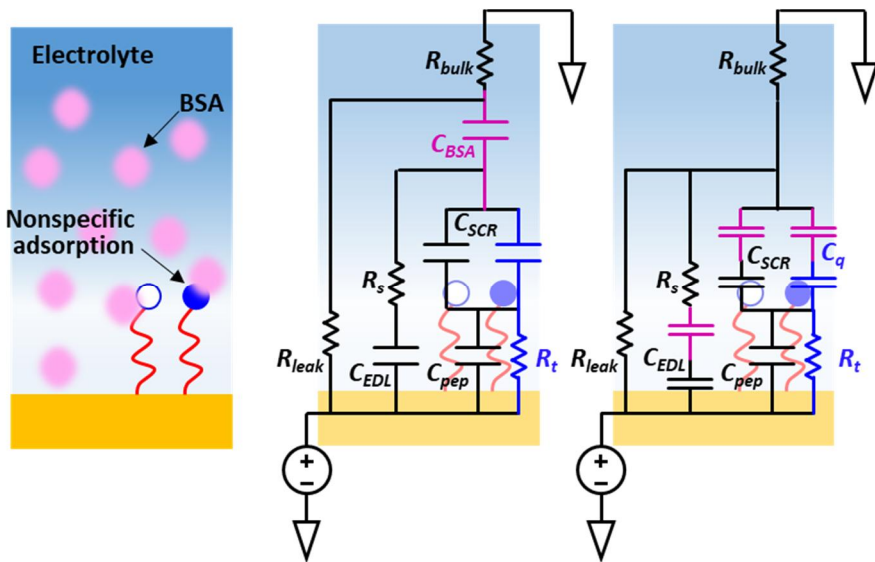


Figure A2-9. (a) equivalent circuit of the T-chip device and (b) simulated I-V characteristics by using MNA in the case of the initial condition (blue) and the case of the device with BSA capacitance, which describe the nonspecific effect to the circuit component equivalently. Each circuit components were dealt with in the previous chapter.

Appendix 3.

Appendix 3. Generalized voltage pulse method.

A3.1. Integration of tunneling current

The key of the suggested voltage pulse method in this research is the elimination of the capacitive current component of the device. Since this is only possible in the case that the C-V characteristic except for the tunneling current component of the device is symmetric. Although many electric and electrochemical biosensor platforms select the electrode structure with SAM, the voltage method cannot be applied to the devices in general cases without SAM.

To overcome this restriction on the voltage pulse method, the generalized voltage pulse method based on tunneling charge rather than tunneling current itself is suggested in this chapter. The tunneling charge can be obtained by integrating the tunneling charge with a simple integrator R-C circuit without changing any components used in the original voltage pulse method. The generalized voltage

pulse method utilizes the difference of the electron transfer rate between the forward and reverse reaction of the redox molecule.

The detail explanation of the generalized voltage pulse method is as follows. Here, we assume the case that no tunneling current flows under zero bias condition of the device and the tunneling current flows inward to the redox state from the electrode under the negative bias condition and flows outward to the electrode under the positive bias condition (same as the MB state). First the rising step of the negative voltage pulse is applied to the electrode of the device. After applying the negative step voltage, the sum of the capacitive, $I_c^+(t)$, and tunneling, $I_t^-(t)$, current flows. The capacitive current decreases rapidly and its value and the total integrated charge, $Q^-(t)$, under the negative bias condition becomes

$$\begin{aligned}
 Q^-(t) &= Q_c^-(t) + Q_t^-(t) \\
 &= Q_c^-(t) - q \int (k_f[MB^+] - k_r[LMB^0])dt \\
 &= Q_c^-(t) - q \int (k_f[MB^+])dt \quad (A3.1.1)
 \end{aligned}$$

where $[LMB^0]$ is close to zero because most of the MB states are unoccupied under zero bias condition to the early phase of the negative voltage pulse step.

Second, the falling step of the negative voltage pulse is applied to the electrode of the device after $Q_c^-(t)$ is saturated, also the total charge $Q^+(t)$ is expressed as

$$Q^+(t) = Q_c^+(t) + Q_t^+(t)$$

$$\begin{aligned}
&= Q_c^+(t) - q \int (k_f[MB^+] - k_r[LMB^0])dt \\
&= Q_c^+(t) + q \int (k_r[LMB^0])dt. \tag{A3.1.2}
\end{aligned}$$

By using the integrator circuit, the total transient charge, $Q(t)$, is

$$Q(t) = Q_c^- + Q_c^+ + Q_t^- + Q_t^+(t). \tag{A3.1.3}$$

Since the RC time constant of the EDL capacitive current is much shorter than decay rate of the tunneling current, the $Q_c^- + Q_c^+$ can be zero at specific time by choosing an appropriate pulse width. It is hard to predict that the charge terms due to the electron tunneling $Q_t^- + Q_t^+(t)$ becomes zero, but leaves with some small amount value of charge, δQ_t , mismatched by the forward and reverse tunneling current where values of k_f and k_r are similar and this method is adopted under the condition of $[MB^+] \neq [LMB^0]$ so δQ_t can be treated as a constant. Therefore after N th negative voltage pulse is applied, the total charge value, Q^N , becomes

$$Q^N = N\delta Q_t. \tag{A3.1.4}$$

The advantage of this method is that the mismatched charge can be continuously added by applying an additional pulse and proportionally amplified with the number of the pulse train as shown in Fig. A3-2.

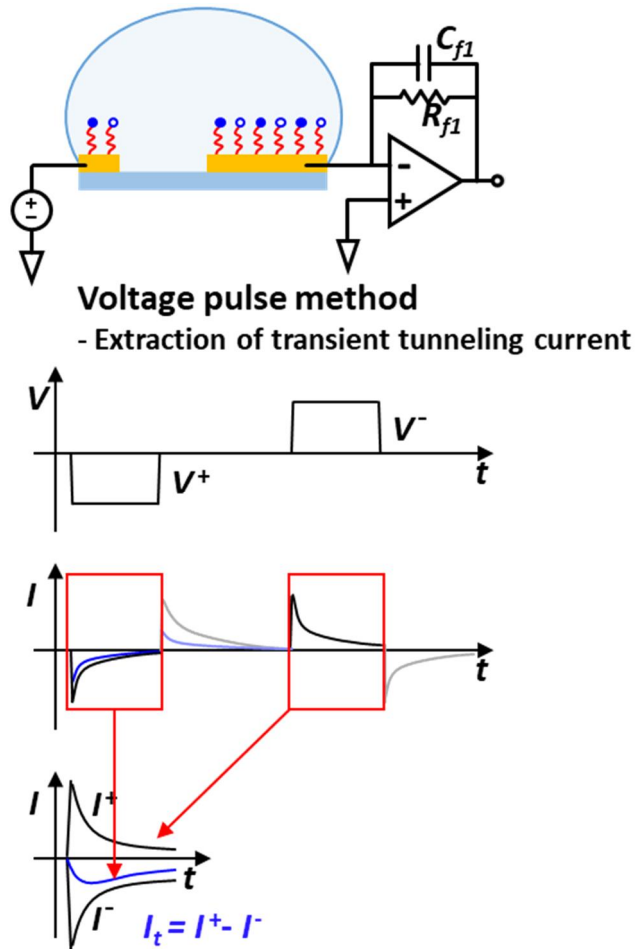
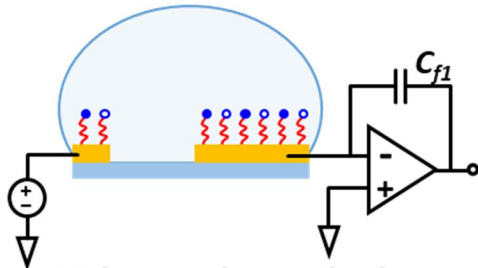


Figure A3-1. Schematic of the voltage pulse method to extract the transient tunneling current.



Voltage pulse method

- Integration of tunneling charge difference

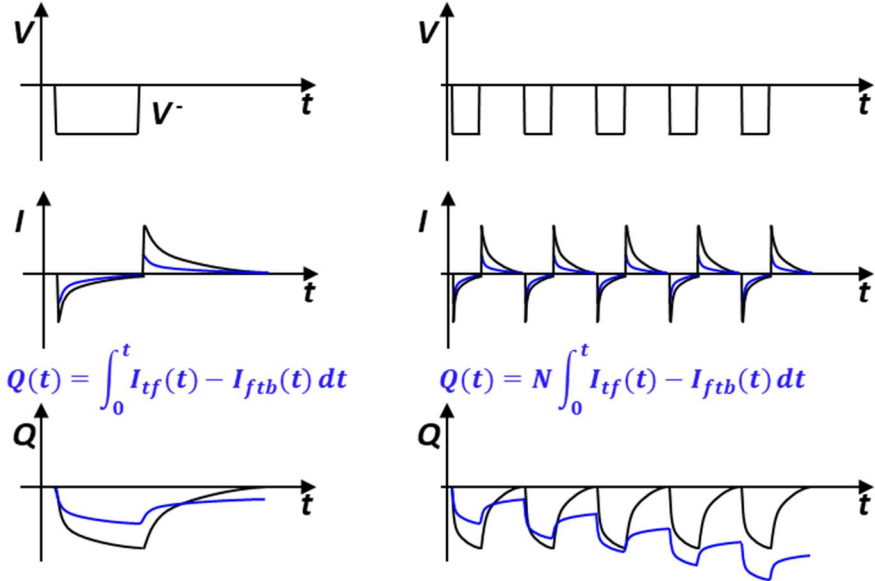


Figure A3-2. Schematic of the generalized voltage pulse method based on integration of the tunneling charge.

Appendix 4.

Appendix 4. pH sensor application

A4.1. MIE capacitor for pH sensor application

In this chapter, another possible application of the T-chip device is suggested. From the previous chapter, the concept of the flat-band voltage can be applied to understand the electrical characteristics of the T-chip device since it is equivalent to the MIE capacitor. Especially, the T-chip device when composed by only the MCH-SAM without the peptide-MB has the negative fixed surface charges at the interface between the insulator and the electrolyte solution. Since the surface concentration of the fixed charge is determined by the concentration of the hydrogen ions (pH value) in the electrolyte solution, this MIE capacitor can be operated as a pH sensor.

Traditionally well-developed electrical pH device is the ion-sensitive field effect transistor (ISFET) device with the electrolyte-insulator-semiconductor (EIS) structure. The ISFET device with an appropriate membrane that allows the hydrogen

ion (proton) to penetrate is used for measuring the hydrogen ion concentration in the electrolyte solution. The surface charge at the oxide-semiconductor interface can be calculated by the site binding model which describe the surface concentration of the Si-OH site in equilibrium. the surface concentration of the hydrogen ion, H_s , following the Boltzmann distribution is given as

$$H_s = H_b \exp\left(-\frac{\phi_0}{k_b T}\right) \quad (\text{A4.1.1})$$

where H_b and ϕ_0 are the bulk concentration of the hydrogen ion and the surface potential. The two possible chemical reaction can be established as



with the amphoteric dissociation constants, $K_+ = [\text{SiOH}][\text{H}_s^+]/[\text{SiOH}_2^+]$ and $K_- = [\text{SiO}^-][\text{H}_s^+]/[\text{SiOH}]$. The total concentration of the surface charge, N_s , and its charge density, Q_s , is simply written as

$$N_s = [\text{SiO}^-] + [\text{SiOH}] + [\text{SiOH}_2^+] \quad (\text{A4.1.3})$$

$$\begin{aligned} Q_s &= q([\text{SiOH}_2^+] - [\text{SiO}^-]) \\ &= q[\text{SiOH}] \left\{ \frac{[H_b^+]}{K_+} - \frac{K_-}{[H_b^+]} \right\} \end{aligned} \quad (\text{A4.1.4})$$

As shown in Fig. A4-1, the MIE and EIS structures show similar structure where the metal, insulator, and electrolyte components correspond to the electrolyte, insulator, and semiconductor components. The difference between the MIE and EIS structure as a pH sensor application is that the MIE structure utilizes the flat-band

voltage shift due to the changes of the electrical potential and of the concentration of the surface charge density at the insulator-electrolyte interface while the EIS structure utilizes the threshold voltage shift due to the those at the insulator-semiconductor interface. the C-V characteristics and the flat-band shift of the MIE capacitor device in the solutions with various pH value are plotted in Fig. A4-2. Although its sensing performance is lower than that of the ideal ISFET, there is significance in suggesting a new concept of the pH sensing device without the membrane structure.

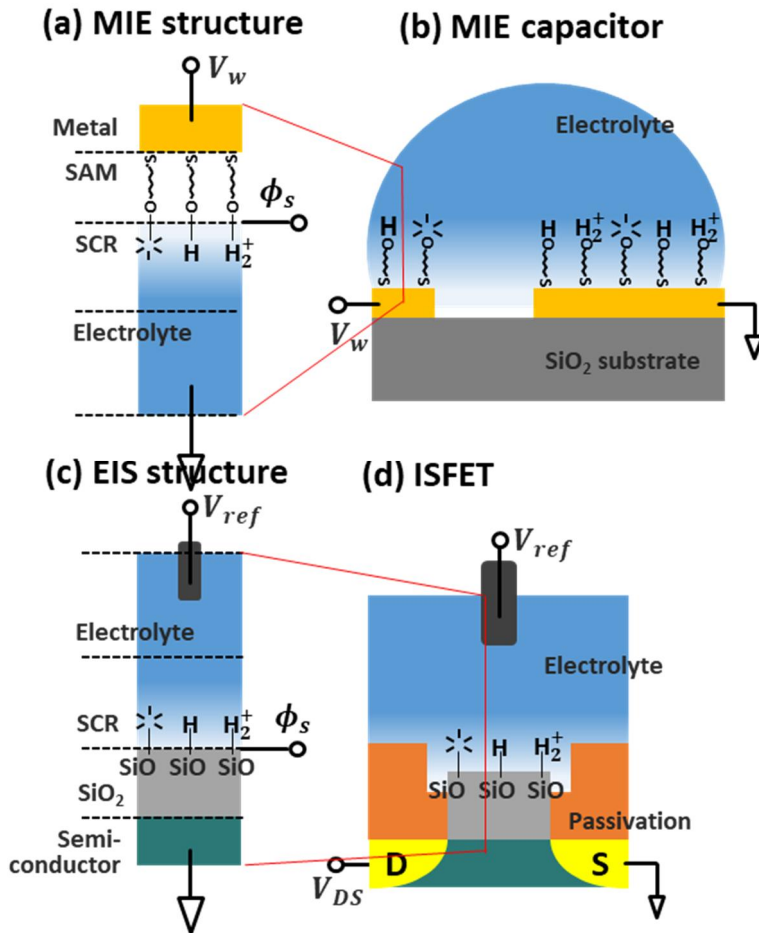


Figure A4-1. (a) MIE structure, (b) MIE capacitor, (c) EIS structure, and (d) ISFET

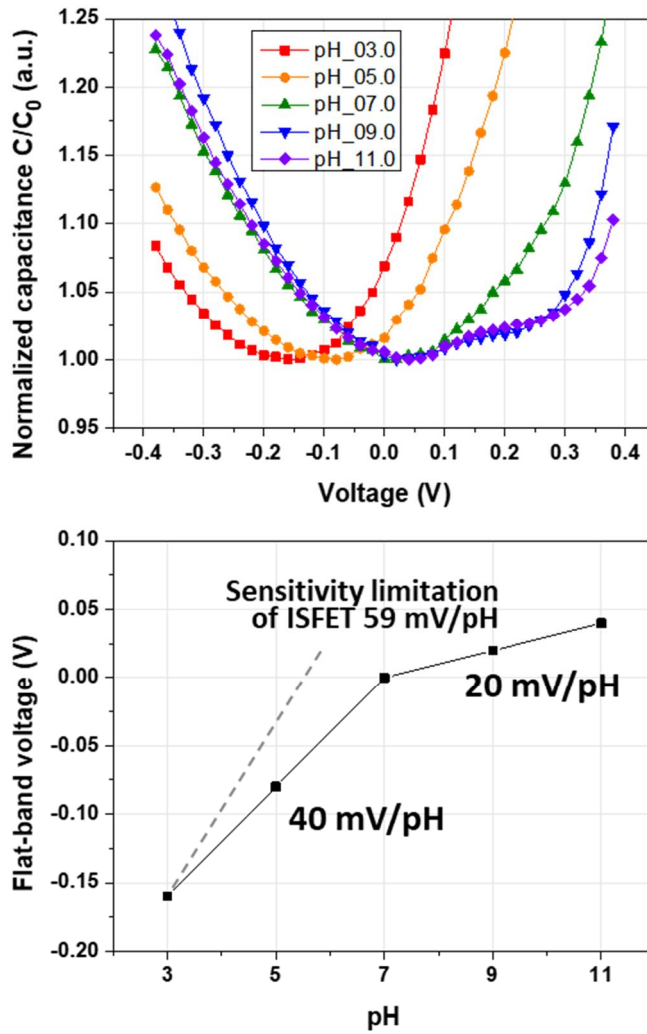


Figure A4-2. (up) C-V characteristics of the MIE capacitor with the various pH conditions. (down) Line plot of the flat-band voltage according to the pH value.

Bibliography

- [1] “Point-of-Care/Rapid Diagnostics Market by Testing (Glucose, Lipids, HbA1c, HCV, HIV, Influenza, Urinalysis, Hematology, Cancer, Pregnancy, PT/INR), Platform (Lateral Flow, Immunoassay), Mode (Prescription, OTC), End-User - Global Forecast to 2022,” 2018. [Online]. Available: <https://www.researchandmarkets.com/research/nhqshh/pointofcarerapi?w=4>. [Accessed: 01-Jul-2018].
- [2] “Insurance Analytics Market: Global Forecast until 2023,” 2018. [Online]. Available: <https://www.reportlinker.com/p05398027/Insurance-Analytics-Market-by-Component-Business-Application-Deployment-Model-Organization-Size-End-User-And-Region-Global-Forecast-to.html>. [Accessed: 01-Jul-2018].
- [3] S. K. Vashist, P. B. Luppá, L. Y. Yeo, A. Ozcan, and J. H. T. Luong, “Emerging Technologies for Next-Generation Point-of-Care Testing,” *Trends Biotechnol.*, vol. 33, no. 11, pp. 692–705, Nov. 2015.
- [4] S. Vashist, E. Schneider, and J. Luong, “Commercial Smartphone-Based Devices and Smart Applications for Personalized Healthcare Monitoring and Management,” *Diagnostics*, vol. 4, no. 3, pp. 104–128, Aug. 2014.
- [5] Q. Zhang, Y. Lu, S. Li, J. Wu, and Q. Liu, “Peptide-based biosensors,” in

- Peptide Applications in Biomedicine, Biotechnology and Bioengineering*, vol. 136, Elsevier, 2018, pp. 565–601.
- [6] B. Turk, “Targeting proteases: successes, failures and future prospects,” *Nat. Rev. Drug Discov.*, vol. 5, no. 9, pp. 785–799, Sep. 2006.
- [7] A. C. Mitchell *et al.*, “Development of a Protease Biosensor Based on a Dimerization-Dependent Red Fluorescent Protein,” *ACS Chem. Biol.*, vol. 13, no. 1, pp. 66–72, 2018.
- [8] T. Kitamura *et al.*, “SMAD4-deficient intestinal tumors recruit CCR1+ myeloid cells that promote invasion,” *Nat. Genet.*, vol. 39, no. 4, pp. 467–475, Apr. 2007.
- [9] Q. Elisa and H. V. Immunoassay, “Quantikine® ELISA,” vol. 9.
- [10] O. A. Zlobovskaya *et al.*, “Genetically encoded far-red fluorescent sensors for caspase-3 activity,” *Biotechniques*, vol. 60, no. 2, pp. 62–68, Feb. 2016.
- [11] S. GRANT, C. WEILBAECHER, and D. LICHLYTER, “Development of a protease biosensor utilizing silica nanobeads,” *Sensors Actuators B Chem.*, vol. 121, no. 2, pp. 482–489, Feb. 2007.
- [12] K. Hu *et al.*, “A human immunodeficiency virus type 1 protease biosensor assay using bioluminescence resonance energy transfer,” *J. Virol. Methods*, vol. 128, no. 1–2, pp. 93–103, Sep. 2005.
- [13] J. Zhou *et al.*, “Assessing activity of Hepatitis A virus 3C protease using a cyclized luciferase-based biosensor,” *Biochem. Biophys. Res. Commun.*, vol. 488, no. 4, pp. 621–627, Jul. 2017.

- [14] P.-T. Chen, T.-Y. Liao, C.-J. Hu, S.-T. Wu, S. S.-S. Wang, and R. P.-Y. Chen, "A highly sensitive peptide substrate for detecting two A β -degrading enzymes: Neprilysin and insulin-degrading enzyme," *J. Neurosci. Methods*, vol. 190, no. 1, pp. 57–62, Jun. 2010.
- [15] S.-Y. Kwak *et al.*, "Luminescent Graphene Oxide with a Peptide-Quencher Complex for Optical Detection of Cell-Secreted Proteases by a Turn-On Response," *Adv. Funct. Mater.*, vol. 24, no. 32, pp. 5119–5128, Aug. 2014.
- [16] H.-S. Lee, J.-S. Oh, Y.-W. Chang, Y.-J. Park, J.-S. Shin, and K.-H. Yoo, "Carbon nanotube-based biosensor for detection of matrix metalloproteinase-9 and S-100B," *Curr. Appl. Phys.*, vol. 9, no. 4, pp. e270–e272, Jul. 2009.
- [17] A. Biela *et al.*, "Disposable MMP-9 sensor based on the degradation of peptide cross-linked hydrogel films using electrochemical impedance spectroscopy," *Biosens. Bioelectron.*, vol. 68, pp. 660–667, Jun. 2015.
- [18] A. Shoji, M. Kabeya, and M. Sugawara, "Real-time monitoring of matrix metalloproteinase-9 collagenolytic activity with a surface plasmon resonance biosensor," *Anal. Biochem.*, vol. 419, no. 1, pp. 53–60, Dec. 2011.
- [19] D.-S. Shin, Y. Liu, Y. Gao, T. Kwa, Z. Matharu, and A. Revzin, "Micropatterned Surfaces Functionalized with Electroactive Peptides for Detecting Protease Release from Cells," *Anal. Chem.*, vol. 85, no. 1, pp. 220–227, Jan. 2013.
- [20] G. S. Choe, D. W. Kim, J. Cheon, S. M. Sea, and Y. J. Park, "Simulation of Self Gating Effect of a Liquid Gate Carbon Nanotube Field Effect Transistor,"

- in *Simulation of Semiconductor Processes and Devices, 2008. SISPAD 2008.*, 2008, pp. 161–164.
- [21] D. W. Kim *et al.*, “Self-gating effects in carbon nanotube network based liquid gate field effect transistors,” *Appl. Phys. Lett.*, vol. 93, no. 243115, pp. 91–94, 2008.
- [22] J. Lee *et al.*, “A reference electrode-free electrochemical biosensor for detecting MMP-9 using a concentric electrode device,” *Sensors Actuators B Chem.*, vol. 240, pp. 735–741, Mar. 2017.
- [23] J. Lee, “Electrical Tunneling Biosensor for Detecting MMP-9 Using Concentric Electrode Device,” Seoul National University, 2016.
- [24] Y. Lee, “Detection of MMP-2 in human serum as the biomarker of colorectal cancer using the T-chip platform,” Seoul National University, 2017.
- [25] J. Lim, “A Biosensor platform based on the Carbon Nanotube Network for detecting antibody antigen reaction,” SEOUL NATIONAL UNIVERSITY, 2018.
- [26] J. Y. Yun, W. C. Lee, S. W. Choi, and Y. J. Park, “Featuring of transient tunneling current by voltage pulse and application to an electrochemical biosensor,” *J. Appl. Phys.*, vol. 123, no. 12, p. 124902, Mar. 2018.
- [27] H.-K. S. Leiros, “Trypsin specificity as elucidated by LIE calculations, X-ray structures, and association constant measurements,” *Protein Sci.*, vol. 13, no. 4, pp. 1056–1070, Apr. 2004.
- [28] N. D. Rawlings and A. J. Barrett, “[2] Families of serine peptidases,” in

- Methods in Enzymology*, vol. 244, no. 26, 1994, pp. 19–61.
- [29] E. González-Fernández, N. Avlonitis, A. F. Murray, A. R. Mount, and M. Bradley, “Methylene blue not ferrocene: Optimal reporters for electrochemical detection of protease activity,” *Biosens. Bioelectron.*, vol. 84, pp. 82–88, Oct. 2016.
- [30] M. S. Hossain and K. H. Bevan, “Exploring Bridges between Quantum Transport and Electrochemistry. II. A Theoretical Study of Redox-Active Monolayers,” *J. Phys. Chem. C*, vol. 120, no. 1, pp. 188–194, Jan. 2016.
- [31] A. Velikonja, V. Kralj-Iglič, and A. Iglič, “On asymmetric shape of electric double layer capacitance curve,” *Int. J. Electrochem. Sci.*, vol. 10, no. 1, pp. 1–7, 2015.
- [32] J. Bisquert, “Chemical capacitance of nanostructured semiconductors: its origin and significance for nanocomposite solar cells,” *Phys. Chem. Chem. Phys.*, vol. 5, no. 24, p. 5360, 2003.
- [33] J. Bisquert, F. Fabregat-Santiago, I. Mora-Seró, G. Garcia-Belmonte, E. M. Barea, and E. Palomares, “A review of recent results on electrochemical determination of the density of electronic states of nanostructured metal-oxide semiconductors and organic hole conductors,” *Inorganica Chim. Acta*, vol. 361, no. 3, pp. 684–698, Feb. 2008.
- [34] A. Ulman, “Formation and Structure of Self-Assembled Monolayers,” *Chem. Rev.*, vol. 96, no. 4, pp. 1533–1554, 1996.
- [35] A. L. Eckermann, D. J. Feld, J. A. Shaw, and T. J. Meade, “Electrochemistry

- of redox-active self-assembled monolayers,” *Coord. Chem. Rev.*, vol. 254, no. 15–16, pp. 1769–1802, 2010.
- [36] C. Nicosia and J. Huskens, “Reactive self-assembled monolayers: from surface functionalization to gradient formation,” *Mater. Horizons*, vol. 1, no. 1, pp. 32–45, 2014.
- [37] Y. Xiao, R. Y. Lai, and K. W. Plaxco, “Preparation of electrode-immobilized, redox-modified oligonucleotides for electrochemical DNA and aptamer-based sensing,” *Nat. Protoc.*, vol. 2, no. 11, pp. 2875–2880, 2007.
- [38] K. Kerman, M. Kobayashi, and E. Tamiya, “Recent trends in electrochemical DNA biosensor technology,” *Meas. Sci. Technol.*, vol. 15, no. 2, pp. R1–R11, Feb. 2004.
- [39] J. J. Gooding and D. B. Hibbert, “The application of alkanethiol self-assembled monolayers to enzyme electrodes,” vol. 18, no. 8, pp. 525–533, 1999.
- [40] A. Radi *et al.*, “Reagentless , Reusable , Ultrasensitive Electrochemical Molecular Beacon Aptasensor,” *J. Am. Chem. Soc.*, vol. 128, no. 1, pp. 117–124, 2006.
- [41] A. J. Bard, L. R. Faulkner, E. Swain, and C. Robey, *Electrochemical Methods: Fundamentals and Applications*, 2nd ed. John Wiley & Sons, 2000, 2001.
- [42] F. Scholz, “Books on Fundamental Electrochemistry and Electroanalytical Techniques,” in *Electroanalytical Methods*, Berlin, Heidelberg: Springer

Berlin Heidelberg, 2010, pp. 343–345.

- [43] G. L. Long and J. D. Winefordner, “Limit of Detection A Closer Look at the IUPAC Definition,” *Anal. Chem.*, vol. 55, no. 07, p. 712A–724A, Jun. 1983.
- [44] W. N. Laurance, “SPICE2: A Computer Program To Simulate Semiconductor Circuits,” University of California, Berkeley, California, 1975.

초 록

전자 터널링 기반의 전기화학 바이오센서 플랫폼

윤(尹) 준 연(俊淵)

전기·컴퓨터공학부

공과대학 대학원

서울대학교

이 논문에서는 T-chip 으로 명명된 전자 터널링 기반의 전기화학적 프로테아제 바이오센서 플랫폼과 과도상태 터널링 전류 특성을 추출할 수 있는 전압 펄스 기법을 제안한다. 또한 T-chip 소자의 전류-전압 (I-V) 그리고 캐패시턴스-전압 (C-V) 특성을 분석함으로써 금속-절연체-전해액 (MIE) 캐패시터 소자라는 새로운 관점을 제시한다.

소 혈청 알부민(BSA)을 500 μM 고농도로 용해하여 인간 혈청을 모사한 용액 환경에서 트립신을 타겟물질로 하고 이를 검출하는 바이오센서 응용을 보였다. 제안된 전압 펄스 기법을 이용하면 기존의 전기화학적 전압순환 측정법을 이용한 경우보다 센서의 민감도와 비특이-특이 비율에 있어서 높은 성능 향상이 이뤄질 수 있음을 실험으로 보였다.

추가로, 기존의 타 연구에서는 중점적으로 다루어지지 않은 배경 채움 물질들의 소자에 대한 영향이 연구되었고, 최적화된 T-chip 구조가 완성되었다. 반응-확산 방정식과 멘틴-미하엘리스 화학 반응속도 역학을 계산함으로써 벌크 전해 용액 내의 생체분자의 거동과 생화학적 반응을 시뮬레이션하였다. 수정된 노달분석기법으로 T-chip 의 등가회로를 시뮬레이션하였다. 전압 펄스 기법의 한계를 극복하기 위해 터널링 전류 적분을 기반으로 일반화된 전압 펄스기법을 제안하였다. 마지막으로, 6-Mercapto-1-hexanol (MCH)을 자기 조립 단분자막 (SAM)으로 이용한 T-chip 소자로 pH 센서 응용을 시연하였다.

이 연구에서, 특히 T-chip 소자의 등가회로를 제안한 접근법에 다소 거친 가정을 이용하더라도 소자의 회로적 해석에 새로운 시각을 착안하는데 초점을 맞추었다. 우리의 접근법이 완전히 견고하지는 않거나 분석된 실험 데이터가 완벽히 정밀하지는 않는다 하더라도 우리는 미래에 활용될 실제 바이오 응용 가능성을 발견하고 기반 이론을 제안하는 것에 큰 가치가 있다고 믿는다. 이 가치에 기반한 우리의 접근법은 바이오센서 분야에만 국한되지 않고 고체소자를 연구하는 어떤 분야에서도 새로운 기여를 할 수 있으리라 기대한다.

주요어 : 전기화학 바이오센서, 프로테아제 바이오센서, 전자 터널링, 자기조립 단분자막, 산화환원상태, 메틸렌블루, 펩타이드, 트립신, 금속-절연체-전해질 구조, 전압순환법, 준-정적 캐패시턴스-전압 측정법, 전압 펄스 방법, 반응-확산 시스템, 멘틴-미하엘리스 반응속도론, 수정된 노달 분석, pH 센서

학번 : 2013-20837

The end of the dissertation.

